Correspondence to:

M. Drilleau,
melanie.drilleau@isae-supaero.fr

Marsquake Locations and 1-D Seismic Models for Mars From InSight Data

Mélanie Drilleau[1] , Henri Samuel[2] , Raphaël F. Garcia[1] , Attilio Rivoldini[3] , Clément Perrin[4] , Chloé Michaut[5] , Mark Wieczorek[6] , Benoît Tauzin[5,7] , James A. D. Connolly[8] , Pauline Meyer[1,9], Philippe Lognonné[2] , and William B. Banerdt[10]

[1]Institut Supérieur de l'Aéronautique et de l'Espace ISAE-SUPAERO, Toulouse, France, [2]Institut de Physique du Globe de Paris, CNRS, Université de Paris, Paris, France, [3]Royal Observatory of Belgium, Brussels, Belgium, [4]Nantes Université, Université d'Angers, Le Mans Université, CNRS UMR 6112, Laboratoire de Planétologie et Géosciences, UAR 3281, Observatoire des Sciences de l'Univers de Nantes Atlantique, Nantes, France, [5]Université de Lyon, Ecole Normale Supérieure de Lyon, Université Claude Bernard Lyon 1, CNRS, Laboratoire de Géologie de Lyon : Terre, Planètes, Environnement, Villeurbanne, France, [6]Université Côte d'Azur, Observatoire de la Côte d'Azur, CNRS, Laboratoire Lagrange, Nice, France, [7]Research School of Earth Sciences, The Australian National University, Canberra, ACT, Australia, [8]Institute of Geophysics, ETH Zürich, Zürich, Switzerland, [9]Ecole et Observatoire des Sciences de la Terre, Université de Strasbourg, Strasbourg, France, [10]Jet Propulsion Laboratory, California Institute of Technology, Pasadena, CA, USA

Abstract We present inversions for the structure of Mars using the first Martian seismic record collected by the InSight lander. We identified and used arrival times of direct, multiples, and depth phases of body waves, for 17 marsquakes to constrain the quake locations and the one-dimensional average interior structure of Mars. We found the marsquake hypocenters to be shallower than 40 km depth, most of them being located in the Cerberus Fossae graben system, which could be a source of marsquakes. Our results show a significant velocity jump between the upper and the lower part of the crust, interpreted as the transition between intrusive and extrusive rocks. The lower crust makes up a significant fraction of the crust, with seismic velocities compatible with those of mafic to ultramafic rocks. Additional constraints on the crustal thickness from previous seismic analyses, combined with modeling relying on gravity and topography measurements, yield constraints on the present-day thermochemical state of Mars and on its long-term history. Our most constrained inversion results indicate a present-day surface heat flux of 22 ± 1 mW/m^2, a relatively hot mantle (potential temperature: 1740 ± 90 K) and a thick lithosphere (540 ± 120 km), associated with a lithospheric thermal gradient of 1.9 ± 0.3 K/km. These results are compatible with recent seismic studies using a reduced data set and different inversion approaches, confirming that Mars' potential mantle temperature was initially relatively cold (1780 ± 50 K) compared to that of its present-day state, and that its crust contains 10–12 times more heat-producing elements than the primitive mantle.

Plain Language Summary The seismic recordings from the InSight mission have proven that Mars is an active planet. Among the several 100s of detected marsquakes, 17 have a sufficient quality to constrain the internal structure of Mars. We found that most of these marsquakes occurred at depths shallower than 40 km, and are located in the Cerberus Fossae region. There are faults in this area, which could be a source of quakes. An important finding is that as on Earth, the crust is made of two types of rocks formed when hot molten material is cooling, quickly near the surface, and slowly in depth because temperature under the planet's surface is higher. Combining our seismic data with other independent geophysical measurements, we are able to reconstruct the thermal history of Mars. Our results indicate that Mars has a relatively hot mantle, and that the uppermost mantle temperature was initially colder than at the present.

1. Introduction

With 100s of seismic events detected since the deployment of the first seismometer at the surface of Mars (Clinton et al., 2021; Giardini et al., 2020), the Seismic Experiment for Interior Structure (SEIS) of Mars (Lognonné et al., 2019) from the InSight (Interior Exploration using Seismic Investigations, Geodesy and Heat Transport) mission has shown that the red planet is seismically active. The estimated global seismic event rate indicates a moderately active planet, with a value far above that of the Moon (excluding deep moonquakes associated with tidal stresses) and slightly below that of the Earth, based on intraplate earthquakes (Banerdt et al., 2020). Most of

the reported events are proposed to be related to thermal cracking, similar to observations on the Moon (Dahmen et al., 2021). However, no seismic event (marsquake) with magnitude larger than four has been detected so far (Clinton et al., 2021), and no impact origin has yet been identified in the seismic data (Daubar et al., 2020). Up to now, only a handful of recorded marsquakes exhibit a sufficient quality to allow for the clear identification of body wave phases. Among those, none showed clearly detectable surface waves (Giardini et al., 2020) that could be powerful to sample the planet's crust and shallow mantle thanks to the recording of multiple surface wave trains (Khan et al., 2016; Panning et al., 2015, 2017).

Despite the small number of exploitable body wave phases detected, this precious data set has led to the first estimations of the interior structure of Mars from the crust to the core (Khan et al., 2021; Knapmeyer-Endrun et al., 2021; Lognonné et al., 2020; Stähler et al., 2021). From receiver function analysis, Lognonné et al. (2020) inferred that the uppermost 8–11 km part of the crust at the InSight landing site is highly altered and/or fractured. By analyzing the seismic phases that are reflected and converted at subsurface interfaces, Knapmeyer-Endrun et al (2021) determined the structure of the crust underneath the InSight landing site, down to the Martian equivalent of the Moho discontinuity. They found the observations to be consistent with models that include at least two and possibly three interfaces, with the local Moho located at 20 ± 5 km depth and 39 ± 8 km depth in the case of a two-layer and a three-layer model, respectively. A more recent analysis of other crustal phases is more in favor of three-layer model (Kim et al., 2021). Using time- and spectral-domain techniques, the first-ever identifications of direct and surface-reflected body wave phases on Mars (P, PP, PPP, S, SS, and SSS) have recently been made (Khan et al., 2021), allowing to jointly invert for both epicentral distance and interior structure. A total of eight marsquakes occurring in the epicentral distance range 25°–75° with moment magnitudes between 3.0 and 4.0 (Clinton et al., 2021) were considered in Khan et al. (2021). Two of these marsquakes were located near Cerberus Fossae (Giardini et al., 2020), a major volcanic and tectonic structure (Perrin et al., 2022), providing direct evidence for ongoing activity associated with these volcano-tectonic features. Brinkman et al. (2021) showed that the source mechanism is coherent with the fault systems, and estimated the hypocenters to be located between 33 and 40 km depth. Combining seismic constraints with geodynamic considerations, Khan et al. (2021) estimated that the crust contains 13–20 more heat-producing elements (HPEs) than the primitive mantle. This crustal enrichment was found to be larger than the one suggested by gamma-ray spectrometer (GRS) mapping (Boynton et al., 2007). It is associated with a moderate-to-elevated present-day surface heat flow compared to pre-mission estimates (Khan et al., 2018; Plesa et al., 2018; Samuel et al., 2019) (in conjunction with a bulk mantle HPE content relatively enriched compared to cosmochemical and geochemical estimates (Wanke & Dreibus, 1994)). The detection of seismic waves reflected at the core-mantle boundary of Mars allowed Stähler et al. (2021) to estimate the radius of the liquid core, with a mean value of 1,830 ± 40 km, consistent with geodetic constraints. The relatively large core size inferred implies a Martian mantle mineralogically similar to that of the terrestrial upper mantle and transition zone, but differing from Earth by lacking a bridgmanite-dominated lower mantle.

Since the studies by Khan et al. (2021) and Stähler et al. (2021), SEIS has recorded additional seismic events, thereby augmenting the initial data set, giving us the opportunity to refine our knowledge on the interior of Mars. In addition, on account of the identification of seismic depth phases (which result from a reflection at the surface of Mars close the epicenter of the event) the estimation of the quake depths, combined with the determination of back azimuths and epicentral distances, can help to better understand the location and the origin of the seismicity on Mars. Indeed, hypocentral depths are crucial to assess the current deformation of the planet, and to infer whether Mars remains internally active or if it is instead passively deformed by global contraction (Knapmeyer et al., 2006; Plesa et al., 2018).

In line with the aforementioned pioneering works, we present a new independent inversion study that further improves our knowledge on both marsquake locations and on the structure of crust, the mantle, and the core of Mars. To this end, we measured the arrival times of body waves (direct, multiples, depth phases, and core-reflected S-waves) for 17 marsquakes, and their back azimuths from the InSight seismic record. Relying on the corresponding set of differential arrival times, our inversions use the largest seismic arrival time data set published so far and considered for Mars, with 108 phase picks. To date, the largest database is made of 76 picks, considering 14 marsquakes (Durán et al., 2022). The previous comprehensive works inverting for Mars' seismic structure considered fixed source depths (Khan et al., 2021; Stähler et al., 2021). As carried out in Durán et al. (2022), our current approach also represents one of the first attempt to invert simultaneously for the complete location of

marsquakes (epicentral distance and depth), and the structure of Mars from the surface down to the core. To assess model resolution and non-uniqueness, we rely on a probabilistic approach (e.g., Mosegaard & Tarantola, 1995; Tarantola, 2005). In addition, to better constrain the seismic structure of Mars, and its present-day thermal state, we used a novel approach (Drilleau et al., 2020, 2021), which enables key quantities for planetary evolution to be inferred (i.e., the mantle rheology, initial thermal state and composition). This geodynamically constrained inversion approach that was recently applied to real data in Stähler et al. (2021) to constrain the core size of Mars allows the planet's thermochemical history to be reconstructed.

To constrain the thermal and chemical history of Mars, Khan et al. (2021) and Knapmeyer-Endrun et al. (2021) estimated in a first step a distribution of seismic velocity models by inverting the seismic data, and then explored in a second step the relevant geodynamic model parameters compatible with the seismic profiles. However, here we take a different methodological path because our inversion fully integrates the thermal history of Mars directly into the forward problem. One main advantage of our approach is to directly connect the posterior uncertainties on the geodynamic parameters to the uncertainties of the seismic observations, in addition to constraining the seismic velocity structure. Moreover, to refine the output distributions of the velocity models and to better constrain the present-day thermal state of Mars and its evolution, we used recent estimates of the crustal thickness below the InSight landing site (Knapmeyer-Endrun et al., 2021).

This paper is organized as follows: Section 2 describes the seismic data used in this study, Section 3 presents the body wave analysis performed to extract arrival times and marsquake back azimuths from the seismic waveforms, Section 4 summarizes the inversion methodologies (forward and inverse problems), Section 5 presents the inversion results, Section 6 discusses the inversion results, and Section 7 summarizes the main findings of this study.

2. Data

The ground velocity measurements (VEL) used in this study were acquired by the very broadband sensor (VBB) of the InSight mission (SEIS) (Lognonné et al., 2019). The raw components from the VBB channels of different orientations are labeled U, V, and W. The raw data in counts of U, V, and W components are corrected for "tick noise" (a constant electromagnetic cross-talk from temperature measurement repeating every second) and "glitch perturbations" (transient one-sided pulses) following the methods described in Compaire et al. (2021) and Scholz et al. (2020). Then, the SEIS-VBB-VEL recordings are converted to ground velocity by removing the instrument response of each component, and by rotating the timeseries into vertical, North and East (ZNE) geographical reference frame. During the detection and the picking of body wave arrival times, the data from the Temperature and Winds for InSight (TWINS) and Pressure instruments from the Auxiliary Payload and Sensor Suite (APSS) were used to monitor the wind speed and direction, as well as the air pressure variations in order to identify potential noise sources induced by atmospheric processes (Banfield et al., 2019; Garcia et al., 2020; Lognonné et al., 2020). The observed marsquakes are assigned to four different classes ranging from A to D based on signal-to-noise ratio and event characteristics (Clinton et al., 2021). Class A corresponds to the highest-quality observations, clear and identifiable phases and clear polarization. Class B is assigned to events with clear phases without polarization. Signals that belong to class C show a good signal-to-noise ratio, but the phase picking is challenging. Class D consists of weakly observed signals. Only the Broad Band (BB) and Low Frequency (LF) events of quality A, B, and C listed in the Mars Quake Catalog V7 (InSight Marsquake Service, 2021) were analyzed in this study. The events presenting signals dominated by a single frequency were excluded from the analysis because they were interpreted as ground velocity variations induced by either atmospheric acoustic waves (Martire et al., 2020) or volcanic tremors (Kedar et al., 2021).

3. Body Wave Arrival Times and Back Azimuth Computations

This section describes the body wave analysis performed to extract arrival times and event back azimuths from the ground velocity waveforms.

3.1. P and S Phase Arrival Time Estimates

The arrival times of direct P and S waves were measured by analyzing the dominant polarization using both coherence and covariance methods (Vidale, 1986), the instantaneous phase coherence between the different

components (Schimmel et al., 2011), and the energy on the ground velocity records. P and S body wave signals are expected to present a high linearity, a significant instantaneous phase coherence between vertical and horizontal components, and a signal energy larger than the one observed prior to the start of the event. The phase picking method presented here differs from the one used in Khan et al. (2021), by attempting to validate the arrival with both polarization and phase coherence analysis. The analysis was performed in two different frequency bands (0.2–0.4 and 0.4–1 Hz). Frequencies below 0.2 Hz were not considered due to a significant increase of noise level at lower frequencies, and to an increase of the noise induced by glitch signals. Despite the glitch removal process (Scholz et al., 2020), residual glitch noise can remain present in the data. This noise source was monitored by plotting the raw SEIS-VBB-VEL waveforms after the glitch removal process is performed to visually detect potential residual glitches. Another important noise source was the vibrations triggered by the wind flowing around the InSight lander. Previous studies demonstrated that this noise can generate ground velocity signals with amplitude that are about twice larger on the vertical component than on the horizontal components (Lognonné et al., 2020; Murdoch et al., 2017), which is polarized almost linearly along the wind azimuth direction (Charalambous et al., 2021; Stutzmann et al., 2021). This noise source was monitored by comparing the polarization azimuth to the wind direction azimuth (modulo 180°).

To visualize all these parameters as a function of time, we created a control panel that is displayed in Figure 1 for the records of the P-wave of event S0173a (note that events are labeled by mission sol of occurrence and
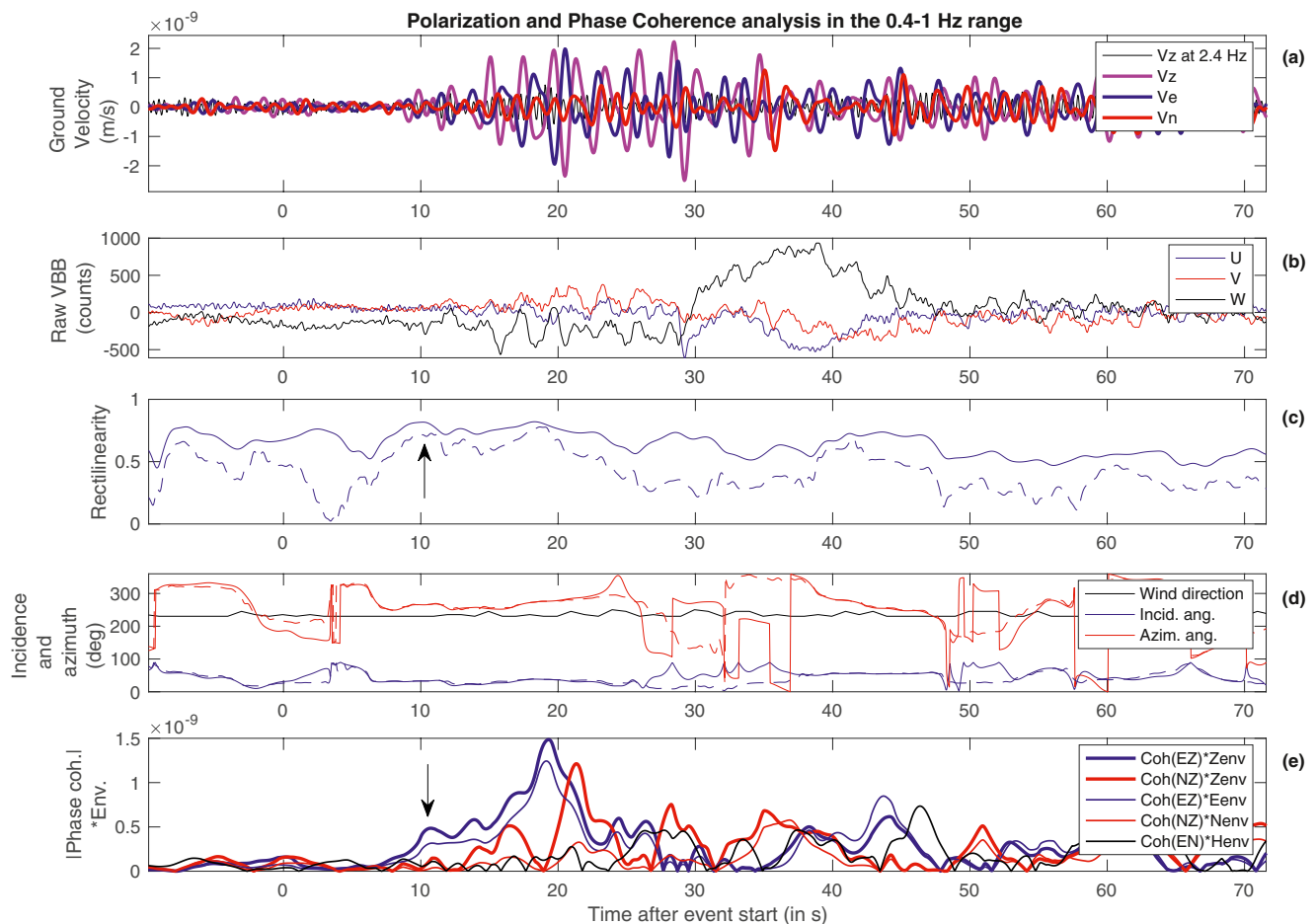
Figure 1. Example of body wave analysis on the direct P wave arrival window for event S0173a. From top to bottom: (a) Ground velocity of the vertical component in a narrow band around 2.4 Hz (black line) and of the three components in the 0.4–1 Hz frequency range (colors). (b) Raw very broadband sensor U, V, and W components (in counts) low pass filtered below 3 Hz. Rectilinearity is shown in panel (c), and incidence angle (blue) and azimuth (red) in panel (d) for polarization analysis with coherence (plain lines) and covariance (dashed lines) methods. Wind azimuth is indicated by a black line in panel (d). Panel (e) presents the products of instantaneous phase coherence between the vertical and the East and North in blue and red respectively, with the envelope of the vertical component (thick lines), or the corresponding horizontal component (thin lines). Coherence between East and North is shown in black. Black arrows indicate the P arrival time estimate.

Table 1

Summary of Back-Azimuth Estimates and Associated Error bar (in °), P and S Direct Phases Arrival Times (YYYY-MM-DD hh:mm:ss:mmm in UTC Time), and Differential Times Between Body Waves and Direct Phases (in s)

Event	Qual.	BAZ-P	BAZ-S	BAZ-best	BAZ-err	P arrival	S-P	pP-P	sP-P	PP-P	PPP-P	sS-S	SS-S	SSS-S	ScS-S
S0154a	C	87	74.5	87	55.6	2019-05-04 07:08:42.101	174.4	–	–	–	–	–	25.3	35	–
S0173a	A	91	86	88.2	15.9875	2019-05-23 02:22:58.547	178.8	–	9.43	19.9	34.4	13.2	24.4	40.5	345.2
S0185a	B	319	324	319.7	14.325	2019-06-05 02:14:11.883	327.28	4	–	22.47	49.3	10	30.9	55.4	152.3
S0235b	A	69	69	69	18.13	2019-07-26 12:19:19.491	171.4	–	–	18.6	32	9.2	23.2	33.3	343.9
S0325a	B	125.5	138	125.5	17	2019-10-26 06:59:00.111	229.3	9.8	–	21.1	34.4	13.8	26.1	50.3	220.4
S0407a	B	79	108.5	79	24.5	2020-01-19 09:57:48.268	170.7	6.77	–	23.38	–	13.3	21.1	33.1	370
S0409d	B	82	335	82	58.9	2020-01-21 11:31:25.480	163.2	8.3	–	27.6	36.94	8.4	20.9	39.8	320.1
S0474a	C	21	40	21	48.75	2020-03-28 00:35:57.678	121.6	–	–	13.4	24.8	–	15.8	32.4	–
S0484b	B	73	123.5	73	33.7	2020-04-07 08:52:36.662	173.1	5.5	–	19.73	–	13	17.4	–	322.3
S0784a	B	100.5	110.5	100.5	17.025	2021-02-09 12:16:17.730	179.3	6.5	–	13.7	22.4	7.2	19.6	28	–
S0802a	B	85	110	85	19.5	2021-02-28 06:11:07.418	180.3	4	–	25.6	33.9	9.3	22.4	36.5	387.6
S0809a	A	86.25	122	86.25	15.2	2021-03-07 11:13:16.881	191.95	4.5	–	16.25	29.65	8.1	23.8	39.3	373.5
S0820a	A	84	74	84	17.85	2021-03-18 14:55:26.005	174.1	–	–	21.9	32.1	8.5	–	–	–
S0861a	C	313	290.5	313	14.95	2021-04-29 18:31:22.012	319.3	–	–	19.6	47.6	–	41.1	–	–
S0864a	A	83.5	90.5	88	27	2021-05-02 01:01:13.600	171.4	–	–	18	27.9	17.3	26.4	–	–
S0916d	B	71	90.5	71	25.25	2021-06-25 05:17:32.834	170.8	3.9	–	19.3	36.1	–	19	42.9	342.8
S0918a	B	161.5	137.5	161.5	90.85	2021-06-27 05:35:19.740	102.4	–	–	12.8	22.5	–	21.2	35	–

Note. When the differential time cannot be estimated, "–" marker is indicated. Error bars for direct P- and S-phases arrival times are 5s. Error bars for PP and SS are 8 and 5s, respectively. Error bars for PPP and SSS are 12 and 8s, respectively. Concerning the depth phases, the error bars are equal to 3s for pP arrival times, and 5s for sP and sS arrival times. Error bars for ScS phases are 12s.

sublabeled alphabetically for sols with more than one event). The P-wave arrival time was measured at the peak value of the product of the vertical component envelope and the absolute value of instantaneous phase coherence between vertical and horizontal component. This peak value was validated by ensuring that it also corresponds to a high value of the signal linearity and a low value of incidence angle, as expected for far field P-waves. We also checked that the dominant polarization azimuth is significantly different from the azimuth of the wind direction. In addition, for this particular event, a glitch signal was observed on raw waveforms (Figure 1b) starting 30 s after the start of the event. The S-wave arrival time was measured in a similar manner. Its validation could not be performed based on the direction of the dominant polarization because the interference between SV and SH waves does not create linearly polarized signals. However, the signal energy being usually stronger for the S-waves than for the P-waves, the arrival time determination was easier on S-waves than on P-waves. Even though wind noise can mimic P-waves, residual glitch signals being most of the time along the horizontal plane, they can also easily mimic SH waves. As a consequence, a careful visual inspection of raw waveforms was performed to ensure that S-wave arrival time was not contaminated by this noise source. Most of the arrival times were determined in the 0.4–1 Hz frequency range. However, due to a larger attenuation, S-waves were also analyzed in the 0.2–0.4 Hz range.

As observed in Figure 1, other arrivals appear after the direct phase and could be measured in a similar manner. However, we preferred to use the method described in Section 3.3 to measure differential times, because it takes into account waveform similarities, and it allows for a more precise measurement of the differential times. Back azimuth measurements are summarized in Table 1. The figures allowing to estimate the back azimuths for the quakes listed in Table 1 are provided in Appendix A.

3.2. Back Azimuth Estimates and Validation of P and S Arrivals

To estimate the event back azimuth and to validate both our direct body wave arrivals and the seismic character of the event, we designed a method to infer the event back azimuth from both P and S waveforms. The consistency between these two estimates validated both the arrival times measurements and the seismic character of the event.

Three different parameters were considered as a function of azimuth during the direct wave arrivals: the energy along the horizontal component, the correlation coefficient between the vertical and the horizontal components, and the instantaneous phase coherence between the vertical and the horizontal components. The parameters were computed for different window sizes, covering the direct phase and its coda, and for all back azimuths with a one degree step. During P-wave arrival, we expect the energy to be maximum, and the correlation coefficient and instantaneous phase coherence to be both negative and minimum in the back azimuth direction. The energy could not be used to determine the S-wave arrival because, due to the interference between SV and SH, the direction of maximum energy along the horizontal strongly depend on the quake mechanism, which was not inferred here. However, due to SV projection along the vertical component, we expected maximum values of both correlation coefficient and instantaneous phase coherence along the back azimuth direction. 0.4–1 Hz frequency range is used for P-waves, but extended to 0.3–1 Hz range for S-waves due to their lower frequency content.

Figure 2 provides an example of the variation of these parameters as a function of back azimuth for event S0173a. The variation of the different markers was provided for various temporal window sizes. As expected, during the P-wave arrival the energy of the horizontal component was maximum, and horizontal to vertical correlation and instantaneous phase coherence were negative when pointing in the back azimuth direction. During the S-wave arrival window, horizontal to vertical correlation and instantaneous phase coherence are maximum when pointing in the back azimuth direction. For this high quality event, the back azimuths determined from P- and S-waves were consistent, validating both these arrival times and the seismic character of the event. However, the processing of lower quality events demonstrated that the methods based on the phase of the signal (correlation coefficients and instantaneous phase) were much less stable relative to noise than the method based on P-wave energy. In addition, validation tests performed on synthetic waveforms (not shown) demonstrated that the methods based on signal phase are also less sensitive to the exacted back azimuth direction. As a consequence, the even back azimuth was determined only from the maximum of P-wave energy along the horizontal, except if the value obtained from S-wave correlation coefficient was within 10°of the back azimuth determined from P-wave energy. In this second case, an average between the two values was used. We considered the event and the direct wave arrival times as validated if the azimuths determined for P- and S-waves were within the same quadrant.

The error on this back azimuth determination was estimated from the standard deviation of the back azimuths determined by using different window sizes (bold dashed lines in Figure 2), and from the back azimuth range covered by the energy value exceeding 80% of the peak energy (thin dashed lines in Figure 2). While the first method surely under-estimates the error bar, the second probably over-estimates it. As a consequence, we simply averaged these two error estimates as a final error bar for the back azimuth determination. However, due to the non-linear character of methods based on signal phase, and due to potential contributions of seismic scattering during the S-wave arrival for some distances or some back azimuth directions, these error estimates cannot take into account all potential contributors to the error budget.

3.3. Differential Times Between Direct Phases and Multiples and/or Depth Phases

Once the seismic event was validated, the arrival times of direct P and S phases were measured, and the back azimuth is estimated, the following method was used to infer the differential times between the direct wave, its multiples, and depth phases. The waveform of the direct P, respectively S, was extracted on the vertical, respectively transverse, component by using temporal windows of different lengths starting 2 s prior to the direct phase arrival. The correlation function between this waveform and the record of the same component was computed to detect multiples of the direct phase by using long temporal windows including depth phases. When short time windows (not including depth phase), were used, the correlation function can enhance the arrival of depth phases since they shared the same source time function with direct phases. This correlation function was also computed for the Hilbert transform of the direct waveform to account for the 90°phase shift of the first multiple (PP or SS). Core reflected S waves were also detected on these correlation functions between direct S and the rest of the waveform on the transverse component, as described in Stähler et al. (2021). An arrival was selected if the
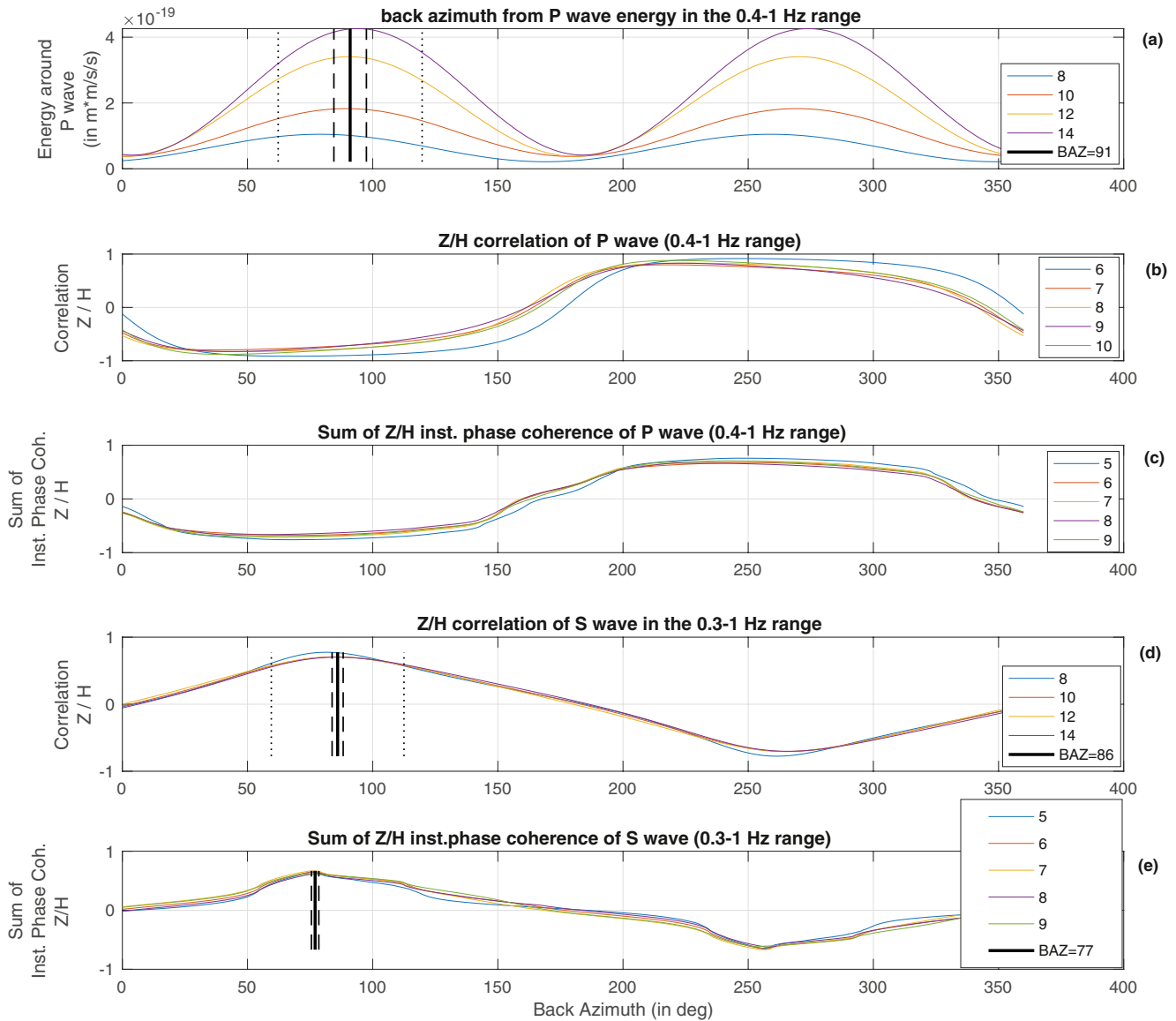
Figure 2. Example of back azimuth determination for event S0173a. From top to bottom: (a) energy along the horizontal component around the P wave arrival, (b) correlation coefficient between vertical and horizontal components around the P wave, (c) average of instantaneous phase coherence between vertical and horizontal components around the P wave, (d) correlation coefficient between vertical and horizontal components around the S wave, and (e) average of instantaneous phase coherence between vertical and horizontal components around the S wave. For each panel, all possible back azimuths are examined and various window lengths (in s) are tested (different colors). Best estimates of back azimuth are identified by vertical black lines. The error on the back azimuth estimate is computed by averaging this standard deviation and the average width of the correlation function at 80% of its peak value.

following conditions were met: the correlation coefficient exceeding a given value (≈0.6), a peak of energy was present at that time in the record, and the differential time roughly consistent with the value predicted by internal structure models (within 10 seconds). This matched filtering method allows one to infer the differential between the given phase and the direct phase much more precisely than methods based only on energy and polarization, and can resolve the interference between the different phases. A practical example is shown for event S0173a in Figure 3. The variation of the different markers is provided for various window sizes. Additional examples are provided in Appendix B.

The body wave arrival times, the differential times, and back azimuth measurements are summarized in Table 1. Our back azimuth measurements are globally in good agreement with Zenhäusern et al. (2022). Note that S0189a and S0167b events used in Khan et al. (2021) are excluded for the following reasons. S0189a is a signal
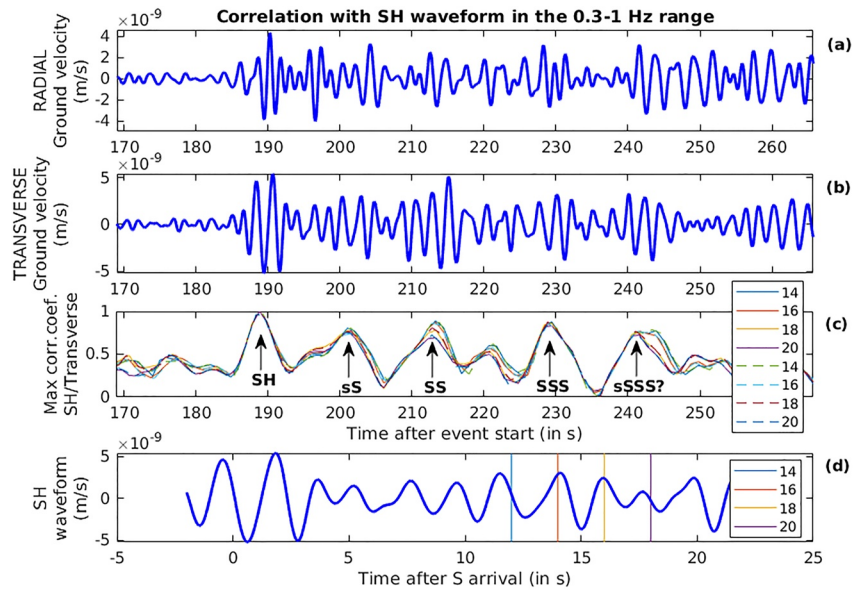
Figure 3. Example of differential times measurements of multiples and depth phases of SH waves for event S0173a. From top to bottom, (a) horizontal ground velocity in the radial direction. (b) Horizontal ground velocity in the transverse direction. (c) Maximum correlation coefficients between SH waveform and horizontal transverse component for different sizes of windows of SH waveform (plain lines) and Hilbert transform of SH waveform (dashed lines). (d) S wave arrival in the horizontal transverse direction (SH waveform), vertical lines in panel (d) indicate the end of the SH wave window. Arrows indicate peaks of correlation coefficient identified as depth phase (sS) or multiples (SS and SSS).

dominated by a single frequency, which is difficult to explain in terms of seismic source. In addition, S0189a has been previously interpreted as either atmospheric acoustic waves (Martire et al., 2020) or volcano tremors (Kedar et al., 2021). The P-wave of S0167b presents a polarization exactly aligned along the wind direction and a P-wave coda of much shorter duration than other seismic events. In addition, we were not able to find a back azimuth consistent between P and S waveforms. These observations suggest that the signal identified as a P-wave may be due to contamination by a wind burst.

4. Inversion Methodology

The inversion methodology is based on the approach proposed in Drilleau et al. (2021). In the following, we summarize the model parameterizations used for the inversions, the forward and inverse problems, and the prior information.

4.1. Forward Problem and Parameterization

The forward problem consists in computing synthetic body wave arrival times from a model of the interior structure of Mars subdivided into a crust, a mantle, and a core.

4.1.1. Classical Approach

We considered a conventional approach in the sense that the models are parameterized in terms of seismic velocity as a function of depth. The models include three layers in the crust. The 1-D V_S models and the V_P/V_S ratio as a function of depth in the mantle, and V_P as a function of depth in the core, are constructed using C^1 polynomial Bézier curves (Drilleau et al., 2013). The advantages of this parameterization is that it does not impose a regularly spaced discretization of the models in depth, or prior constraints on layer thicknesses and location of seismic discontinuities in the mantle. The models can vary smoothly over the entire depth space or instead include sharp discontinuities. This classical approach considering velocity models does not enforce the matching of the planet's mass, moment of inertia and degree-two Love number.

4.1.2. Geodynamically Constrained Approach

The Geodynamically constrained approach relies on the modeling of the thermo-chemical history of a Mars-like planet (Samuel et al., 2019) that predicts present-day density and seismic velocity profiles. The methodology is described in detail elsewhere (Drilleau et al., 2020, 2021) and will therefore only be briefly summarized below. The marsquake epicentral distances and depths are also inverted for at the same time. This approach has been previously used to constrain the core radius of Mars (Stähler et al., 2021).

Contrary to more classical parameterizations, here we do not directly invert for seismic velocities and density values along a radial domain. Instead, we first compute the thermal and chemical transfers in a spherically symmetric planet of radius $R = 3,389.5$ km and surface temperature $T_s = 220$ K divided into several concentric envelopes: a liquid adiabatic iron-alloy core, a convecting silicate mantle of thermal conductivity $k_m = 4$ W/m/K, overlaid by an evolving lithospheric lid (also of conductivity k_m) that includes an evolving crust enriched in HPEs with respect to the mantle. The crust's thermal conductivity is fixed to $k_{cr} = 2.5$ W/m/K. This leads to a set of coupled differential equations that are numerically solved using finite differences schemes, as described in Samuel et al. (2019) and references therein. Therefore, rather than varying independently the value of seismic velocities and density along each radial point of the domain, we sample a parameter space of smaller dimension. The latter is composed of the values of several governing parameters varied within plausible bounds: the mantle rheology (its activation energy (E^*), its activation volume (V^*), and its viscosity (η_0) at reference pressure and temperature of 3 GPa and 1600 K, respectively), the initial uppermost mantle temperature (T_{m_0}), the initial core-mantle boundary temperature (T_{c_0}), the crustal enrichment factor Λ, defined as the ratio of heat production in the crust to the total heat production in the bulk silicate envelope crust plus mantle, and core radius (R_c) is allowed to randomly vary between 1,500 and 2000 km. For each sample we compute a thermo-chemical evolution.

The ranges or the values of the governing parameters are listed in Table 2. Several bulk compositions in major and HPE elements have been proposed for the bulk silicate Mars (e.g., Plesa et al., 2015 and references therein). We considered the composition of the silicate envelope to be the EH45-chondrite model of Sanloup et al. (1999). The latter consists of a mixture of 55% H chondrite with 45% enstatite chondrite, and we accounted for potassium depletion using a K/Th ratio of 5,300 from GRS estimates (Boynton et al., 2007). These choices fix the bulk silicate compositions in terms of major elements and HPE contents, leading to $U = 14$ ppb, Th = 54 ppb, $K = 284$ ppm that are similar to those proposed in Wanke and Dreibus (1994) and in G. J. Taylor (2013) (i.e., $U = 16$ ppb, Th = 56 ppb, $K = 305$ ppm). This composition was chosen because is was shown to be compatible with with receiver functions, gravity data, the degree two Love number, and the Moment of Inertia (MoI) factor of Mars, while the major element abundances proposed in the standard composition discussed in G. J. Taylor (2013) yield a structure that is more difficult to reconcile with these constraints (Knapmeyer-Endrun et al., 2021). This was confirmed by separate sets of inversions presented in Appendix C where we considered the composition described in G. J. Taylor (2013) for the mantle for both major and HPEs. While the inversion results are similar to those obtained with a EH45 composition when no crustal constraints are considered, we were not able to find solutions that satisfied both the MoI and crustal constraints (see Appendix C for further details) in this case. For this reason, we opted for the EH45 composition for the geodynamically constrained inversions.

With the knowledge of composition and thermal state, bulk mantle properties (density, thermal expansion, specific heat) are deduced. Each thermo-chemical history (corresponding to a given set of the aforementioned model parameters) is evolved for 4.5 Gyr. The resulting thermo-chemical structure is then used to compute the seismic velocity structure at the present-day. In the mantle, our mineralogical model relies on the `Perple_X` Gibbs free energy minimization software (Connolly, 2005) with the thermodynamic database of Stixrude and Lithgow-Bertelloni (2011). For the core, we considered a simple generic equation of state for a compressible medium following Nimmo and Faul (2013) that does not make assumptions about the composition of the core, in which the density is adjusted to match the mass constraint of Mars, $M = 6.417 \times 10^{23} \pm 2.981 \times 10^{19}$ kg (Konopliv et al., 2016). In the crust, the seismic velocity and density are based on the results of receiver functions, while the crustal density is iteratively adjusted within bounds compatible with receiver functions and gravity data inversion (Knapmeyer-Endrun et al., 2021). The crust builds up from the occurrence of melt at shallow depth, where its positive buoyancy at low pressure (<7.4 GPa; Ohtani et al., 1998) allows for its upward extraction (Breuer & Spohn, 2006; Hauck & Phillips, 2002; Samuel et al., 2019), accounting for the effect of heat consumption/release through fusion/crystallization with a latent heat of melting-crystallization of $L_m = 6 \times 10^5$ J/kg. In addition, as in

Table 2
List of Inverted Parameters and the Corresponding Prior Bounds Considered for Classical and Geodynamically Constrained Models

Description	Quantity	Value/range	Distribution
Classical models			
Depth of the upper crust	1	4 km—depth of the lower crust	Gaussian
Depth of the mid-crust	1	4 km—depth of the lower crust	Gaussian
Depth of the lower crust	1	4–130 km	Gaussian
R_c (core radius)	1	1,500–2000 km	Gaussian
V_S in the upper crust	1	1.0–3.0 km/s	Gaussian
V_S in the mid-crust	1	1.0–4.4 km/s	Gaussian
V_S in the lower crust	1	1.0–4.4 km/s	Gaussian
V_S in the mantle	12	Provided in Figure 4	Gaussian
V_P/V_S in the entire crust	1	1.7–1.9	Gaussian
V_P/V_S in the mantle	6	1.6–2.1	Gaussian
V_P in the core	8	4.8–5.7	Gaussian
Source epicentral distance	17	0–180°	Gaussian
Source depth	17	5–200 km	Gaussian
Geodynamically constrained models			
T_{m_0} (initial uppermost mantle temperature)	1	1700–2000 K	Gaussian
T_{c_0} (initial core-mantle boundary temperature)	1	$T_{c_0} - T_{m_0} = 300 - 600$ K	Gaussian with a dependence on T_{m_0}
E^* (mantle activation energy)	1	60–500 kJ/mol	Gaussian
η_0 (mantle viscosity)	1	10^{20}–$10^{22.5}$ Pa s	Gaussian
V^* (mantle activation volume)	1	0–10 cm³/mol	Gaussian
Λ (crustal enrichment factor)	1	5–20	Gaussian
Depth of the upper crust	1	4 km—depth of the lower crust	Gaussian
Depth of the mid-crust	1	4 km—depth of the lower crust	Gaussian
R_c (core radius)	1	1,500–2,000 km	Gaussian
V_S in the upper crust	1	1.0–3.0 km/s	Gaussian
V_S in the mid-crust	1	1.0–4.4 km/s	Gaussian
V_S in the lower crust	1	1.0–4.4 km/s	Gaussian
V_P/V_S in the entire crust	1	1.7–1.9	Gaussian
Mantle V_S factor	1	0.95–1.05	Gaussian
Mantle V_P factor	1	0.95–1.05	Gaussian
Source epicentral distance	17	0–180°	Gaussian
Source depth	17	5–200 km	Gaussian

the classical approach, we considered a crustal stratification with three layers, as suggested by receiver functions analysis (Knapmeyer-Endrun et al., 2021). Even though the total crustal thickness is an output parameter of the thermo-chemical modeling, we inverted for the individual thicknesses of each crustal sub-layer along with their associated seismic velocities within plausible bounds suggested by our current knowledge on Mars (Table 2).

For each set of inverted model parameters (E^*, V^*, η_0, T_{m_0}, T_{c_0}, Λ, and R_c) we require that the computed thermo-chemical histories satisfy the following constraints: (a) estimates of Mars' normalized MoI factor $I/(MR^2) = 0.3634 \pm 0.0006$ (Konopliv et al., 2020), (b) estimates of the degree-two Love number $k_2 = 0.174 \pm 0.008$ that includes atmospheric correction (Konopliv et al., 2020), and (c) supercritical values of mantle Rayleigh numbers (i.e., non-convecting mantles) to be compatible with the recent traces of volcanism observed at the surface (Hartmann et al., 1999; Neukum et al., 2004). Models that fail to satisfy the constraints above are rejected.

In some cases (i.e., Section 5.4), we also consider a fourth requirement that the present-day average crustal thickness (Dcr) must lie within the bounds inferred from receiver functions and gravity data (Knapmeyer-Endrun et al., 2021).

As shown in Drilleau et al. (2021), these constraints associated with the geodynamic considerations yield a considerably more informative prior, provide constraints on parameters that are difficult to measure (i.e., the mantle rheology), and allows for the reconstruction of the thermo-chemical history of the planet.

The thermo-chemical evolution modeling summarized above is similar to the one used as a post-processing stage in Khan et al. (2021) and involves a number of additional parameters that we did not invert for. However, here these parameters values are either directly obtained from the thermodynamic model mentioned above (e.g., the mantle density or specific heat at constant pressure), or are computed self-consistently (e.g., surface or CMB gravity and pressure), or are adjusted iteratively within plausible bounds to match geodetic, seismic, gravity and topography data (crustal and core densities), as explained above.

4.1.3. Arrival Times Computation

For each sampled model, the body wave arrival times are calculated using the `TauP` software (Crotwell et al., 1999). Note that only the first arrival of each seismic phase is considered. This implies that we always picked the first arrival in the seismograms.

4.2. Inverse Problem

Due to the ill-posed nature of the problem (i.e., several different combinations of the parameters can yield the same arrival times), we use a Bayesian approach based on a Markov chain Monte Carlo (McMC) method (e.g., Mosegaard & Tarantola, 1995; Tarantola, 2005) to solve the inverse problem. To do so, we adapted the procedure described in Drilleau et al. (2021) for P- and S-phase arrivals, to our data set composed of multiple phases.

To estimate the posterior distribution of the parameters, we use the Metropolis algorithm (Hastings, 1970; Metropolis et al., 1953). In the McMC algorithm, new models are proposed by randomly perturbing the previously accepted model using a Gaussian probability density distribution. The model space is sampled in a random fashion with a sampling density proportional to the posterior probability density function (pdf), and thus ensures that low-probability areas are sampled less excessively. This algorithm relies on a randomized decision rule, which accepts or rejects the proposed model according to its fit to the data and the prior information. It ensures that models that fit data well and are simultaneously consistent with prior information are sampled more frequently.

The inversion output consists of an ensemble of internal structure models that fit the data set. Since the origin time of the seismic events remains unknown (because the InSight seismic network consists of a single seismic station), we use differential times relative to the P- and S-waves phase arrivals (Drilleau et al., 2021; Durán et al., 2022; Khan et al., 2021; Stähler et al., 2021):

$$
\begin{aligned}
\mathcal{M} = \sum_{i=1}^{N} \Bigg[& \frac{|(t_S^{obs} - t_P^{obs}) - (t_S^{calc} - t_P^{calc})|}{\sigma_S + \sigma_P} + \frac{|(t_{pP}^{obs} - t_P^{obs}) - (t_{pP}^{calc} - t_P^{calc})|}{\sigma_{pP} + \sigma_P} + \frac{|(t_{sP}^{obs} - t_P^{obs}) - (t_{sP}^{calc} - t_P^{calc})|}{\sigma_{sP} + \sigma_P} \\
& + \frac{|(t_{PP}^{obs} - t_P^{obs}) - (t_{PP}^{calc} - t_P^{calc})|}{\sigma_{PP} + \sigma_P} + \frac{|(t_{PPP}^{obs} - t_P^{obs}) - (t_{PPP}^{calc} - t_P^{calc})|}{\sigma_{PPP} + \sigma_P} + \frac{|(t_{sS}^{obs} - t_S^{obs}) - (t_{sS}^{calc} - t_S^{calc})|}{\sigma_{sS} + \sigma_S} \\
& + \frac{|(t_{SS}^{obs} - t_S^{obs}) - (t_{SS}^{calc} - t_S^{calc})|}{\sigma_{SS} + \sigma_S} + \frac{|(t_{SSS}^{obs} - t_S^{obs}) - (t_{SSS}^{calc} - t_S^{calc})|}{\sigma_{SSS} + \sigma_S} \Bigg] + \frac{|(t_{ScS}^{obs} - t_S^{obs}) - (t_{ScS}^{calc} - t_S^{calc})|}{\sigma_{ScS} + \sigma_S} \Bigg],
\end{aligned}
\tag{1}
$$

where the cost function $\mathcal{M}$ is defined as the sum of the differences between observed (t^{obs}) and computed (t^{calc}) arrival times taking into account the error bars σ, for the N different quakes.

4.3. Prior Information

The prior model parameter information, which represents our current state of knowledge, is summarized in Table 2 for the two parameterizations described in Section 4.1. The *a priori* distributions of V_S and V_P, and the V_P/V_S ratio are shown in Figure 4. The parameters of the two different approaches are randomly sampled within relatively broad parameter spaces.

Both classical and geodynamic parameterizations consider three layers in the crust, as estimated by receiver functions studies (Kim et al., 2021; Knapmeyer-Endrun et al., 2021). Due to the assumed heterogeneous mineralogical

Classical inversion   Geodynamically-constrained inversion
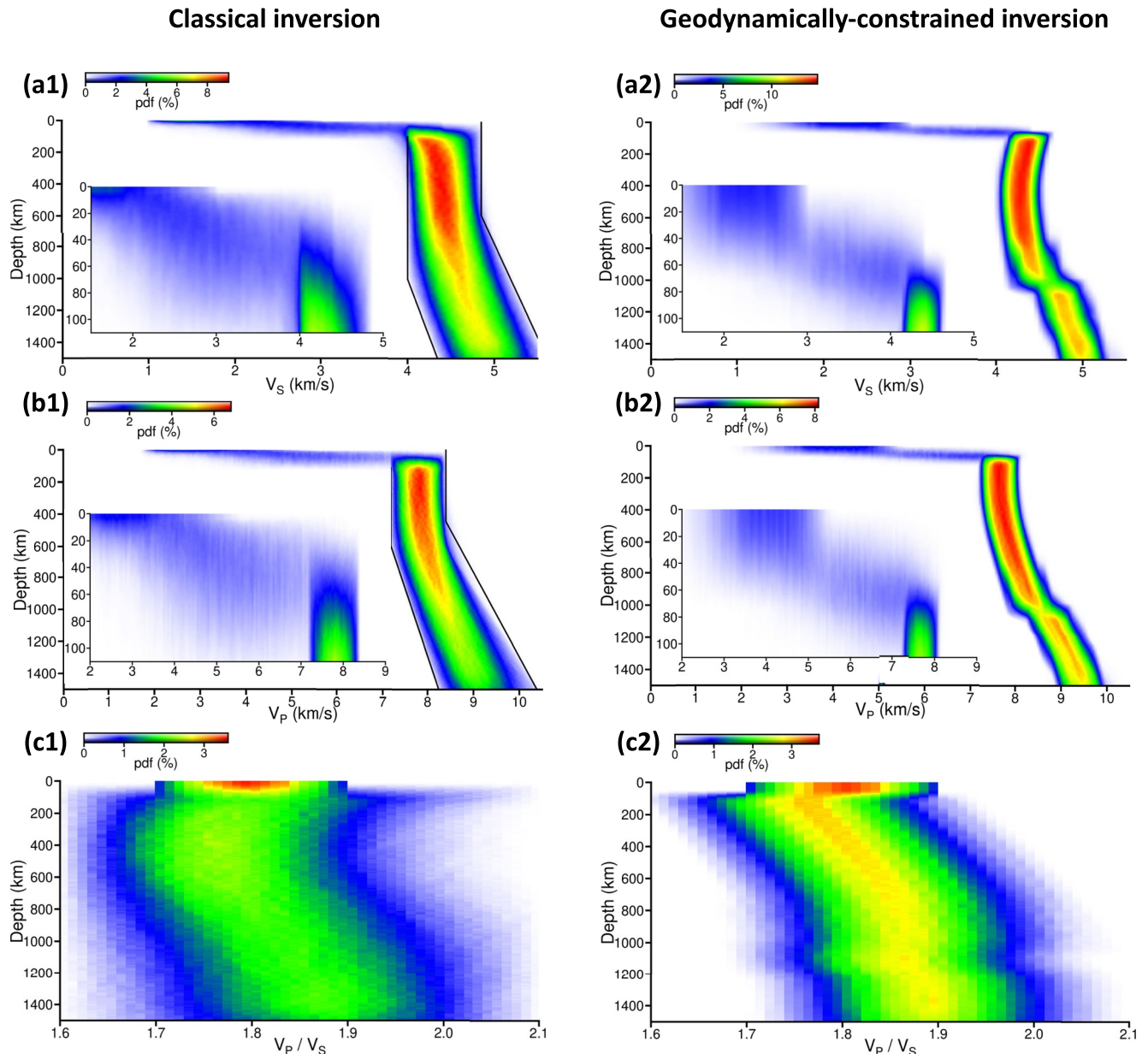
Figure 4. *A priori* probability density functions (pdfs) of the 1-D V_S profiles (a1 and a2), V_P profiles (b1 and b2) and the V_P/V_S ratio (c1 and c2), for the classical and geodynamic approaches, considering that all the sampled models which are in good agreement with *a priori* information detailed in Table 2 are accepted. These are the priors of the inversions detailed in Section 5. Blue and red colors show small and large probabilities, respectively. The pdf is computed by counting the number of sampled profiles in each of the cases. The discretization is 1 km for depth, 0.05 km/s for V_S and V_P, and 0.01 for the V_P/V_S ratio. For a given depth, the sum of the pdf over all the parameter intervals is equal to 100%. The black lines in panels (a1 and b1) shows the prior bounds of classical models in the mantle. A zoom on the crust between the surface and 110 km depth is shown in panels (a1, a2, b1, b2).

content in the crust and the inadequacy of thermodynamic formalism used in `Perple_X` applied at crustal P–T conditions, the same ranges for V_P and V_S values are applied for the two methods. The range of V_P/V_S values allowed in the crust is deduced from an analysis of reflected and converted seismic phases from subsurface interfaces at the InSight landing site (Knapmeyer-Endrun et al., 2021). The total crustal thickness is allowed to vary between 4 and 130 km for the classical models, whereas for the geodynamically constrained models this value directly results from the thermo-chemical evolution modeling. The thicknesses of the mid and lower crusts are then randomly sampled between 4 km and the total crustal thickness value. We impose that the seismic velocities within the crust increase with depth, and that S-wave velocity jumps across crustal discontinuities do not exceed 1.5 km/s, which is large compared to what is found on Earth (Barton, 2006).

In the mantle, the prior bounds cover the representative range of seismic Martian interior models described in Smrekar et al. (2019) and in Yoshizaki and McDonough (2021), constrained by geodetic data, geochemical and thermal considerations. The seismic velocities from the geodynamically constrained approach are directly obtained from the thermal profiles and the assumed mantle composition, as detailed in Section 4.1.2. The seismic velocity profiles are allowed to be shifted by ±5% to account for uncertainties in the thermochemical and mineralogical models. The representative range of seismic Martian interior models described in Smrekar et al. (2019), constrained by geodetic data, geochemical and thermal considerations, is thus included within the prior bounds. We verified that reducing the uncertainties in the thermochemical and mineralogical models reduces the spread of the parameters' distributions, but it does not change the main conclusions of our study. The V_S and V_P prior bounds of the classical models in the mantle are displayed with black lines in Figure 4. To ensure the presence of a velocity jump between the crust and mantle for the classical models, we require that V_S and V_P in the first Bézier point in the mantle to be larger than the values of V_S and V_P in the lowest crustal layer. In the mantle, the *a priori* distributions values of the geodynamically constrained models (Figures 4a2–4c2) are smaller compared to the classical models (Figures 4a1–4c1), due to the physical assumptions used in the forward problem (Section 4.1.2). The V_P/V_S ratio increases as a function of depth for the geodynamic models (Figure 4c2), because the increasing temperature with depth in the mantle produces a larger decrease in V_S than in V_P as a function of depth. On the other hand, the V_P/V_S ratio of the classical models can increase or decrease with depth. Note that the discontinuity near 1,100 km depth for the geodynamic models is related to the olivine-to-wadsleyite phase transition.

The core radius (R_c) for both parameterizations can randomly vary between 1,500 and 2,000 km. For the classical parameterization, we require that V_P increases with depth in the core. However, V_P is not constrained below 700 km depth (Appendix D), because no observations of P-waves that traverse the lower mantle were observed so far.

The epicentral distance and the depth of the 17 sources are randomly sampled between 0 and 180° and 5–200 km, respectively.

4.4. Computational Aspects

To reduce the trade-offs between the parameters and for computational efficiency purposes, we performed a two-stage inversion. The purpose of the first stage is to provide a first estimation of the quake locations (epicentral distance and depth), while the second stage is dedicated to constrain the seismic interior structure, and to refine the quake locations.

In the first stage, only the P- and S-waves arrivals, as well as the depth phases (pP, sP, and sS) are considered in the cost function (Equation 1). Each seismic event is inverted individually. As shown in Drilleau et al. (2020), the output epicentral distance distributions from the inversion of the differential arrival times $t_S - t_P$, reflect the range of epicentral distances compatible with the *a priori* distribution of seismic velocity profiles. The depth phases, reflected from the surface of the planet at locations relatively close to the hypocenter, allow the quake depths to be constrained. Indeed, the depth phase arrival time follows the P- or S-waves by a time interval that changes slowly with distance but rapidly with depth. Then, using the differential times $t_{pP} - t_P$, $t_{sP} - t_P$, and $t_{sS} - t_S$, and by randomly sampling the epicentral distance, the quake depths can be determined. The output distributions of the epicentral distances and depths are subsequently used as a prior for the second stage, thereby reducing the parameter space.

In the second stage, all the seismic phases are used, and the 17 quakes are considered in the same inversion scheme. For computational efficiency, we followed the approach originally developed by Drilleau et al. (2013)

and performed the second stage of the inversion in three different steps. The two first steps seek for a family of the best-misfit configurations of the parameters, and the statistics are performed during the third step. During the first step, a broad exploration of the model space is performed by randomly perturbing the parameters using wide Gaussian proposal distributions. To allow the algorithm to sample a sufficient number of extrema in the model space, we run 192 independent Markov chains in parallel over 900 iterations. The starting model for each chain is randomly chosen within the prior, and thus each chain follows a different path in the model space. The best-fitting model is then determined for each chain and sorted in ascending order. To discard the chains that might not have converged, based on experience we empirically selected the best ∼35% of parameters that are associated with the smallest misfits among the 192 best-fitting models generated to be the starting models for the second step.

The selected 72 independent chains are then run in parallel for 8,000 iterations during the second step, sampling the parameter space with narrower Gaussian proposal distributions. Reducing the Gaussian proposal distributions ensures this time to preserve most of the characteristics of the starting model, which may have resulted in a good data fit. Again, we kept only the 48 best-fitting models out of the 72 at the end of the step 2, and the step 3 restarted from these 48 models for another 10,000 iterations. The models sampled during the step 3, which we consider to be the "stationary period", are then used to compute the pdfs. Since the McMC method provides a series of dependent samples, we reduce the correlation between the output models by further retaining one model every 25 models out of the resulting output. The posterior probabilities shown in Section 5 therefore correspond to 19,200 models.

5. Inversion Results

In this section, we present inversion results of the differential arrival times recorded by SEIS from 17 marsquakes. We first show the marsquake locations (epicentral distance and depth). The data fit is then discussed. We present the retrieved 1-D seismic models and show how independent constraints on the crustal thickness can reduce the trade-off between the parameters. Then, we discuss the constraints obtained on the geodynamic parameters and on the present day thermal state.

5.1. Marsquake Locations

The *a posteriori* distributions of the epicentral distances and the quake depths for both inversion methods are displayed in Figure 5. The black lines delineate the prior bounds deducted from the first step of the inversion process, as explained in Section 4.4.

A good agreement between the retrieved epicentral distances is found for both parameterizations. The mean epicentral distance values and the 1-σ standard deviations are summarized in Table 3. It is worth noting that the *a posteriori* distributions from the classical parameterization (Figure 5a1) are slightly more spread out, due to larger flexibility allowed in the model sampling compared to the geodynamically constrained inversion (Figure 5a2). Both methods show that 12 out of the 17 marsquakes occurred near 30° of epicentral distance. Events S0185a, S0325a, and S0861a are located at larger distances, between 40° and 55°. Events S0474a and S0918a are located closer to the InSight lander, between 17° and 21°. The epicentral distances of events S0173a, S0185a, S0235b, S0325a, and S0407a, are coherent with those estimated in Clinton et al. (2021). Our current study shares six out of the eight marsquakes selected in Khan et al. (2021), and 11 out the 14 marquakes used in Durán et al. (2022). Our output epicentral distances are in good agreement with those inferred in Khan et al. (2021) and Durán et al. (2022) (error bars are overlapping).

The *a posteriori* distributions of the quake depths indicate that the hypocenters are relatively shallow, lying between 40 km depth and the surface (Figures 5b1 and 5b2). We checked whether considering the quake depths as fixed could introduce some biases and shift the seismic velocity distributions toward larger or smaller values. Our results are consistent with the shallow depths estimated in Brinkman et al. (2021) for events S0173a and S0235b, and Durán et al. (2022) for 14 events. As argued in Brinkman et al. (2021), because none of the events manifest surface waves of amplitude greater than the instrument noise (Giardini et al., 2020), event depths shallower than 10 km are less likely. Indeed, if the event depth is larger than the penetration depth for the high-frequency

Classical inversion

Geodynamically-constrained inversion
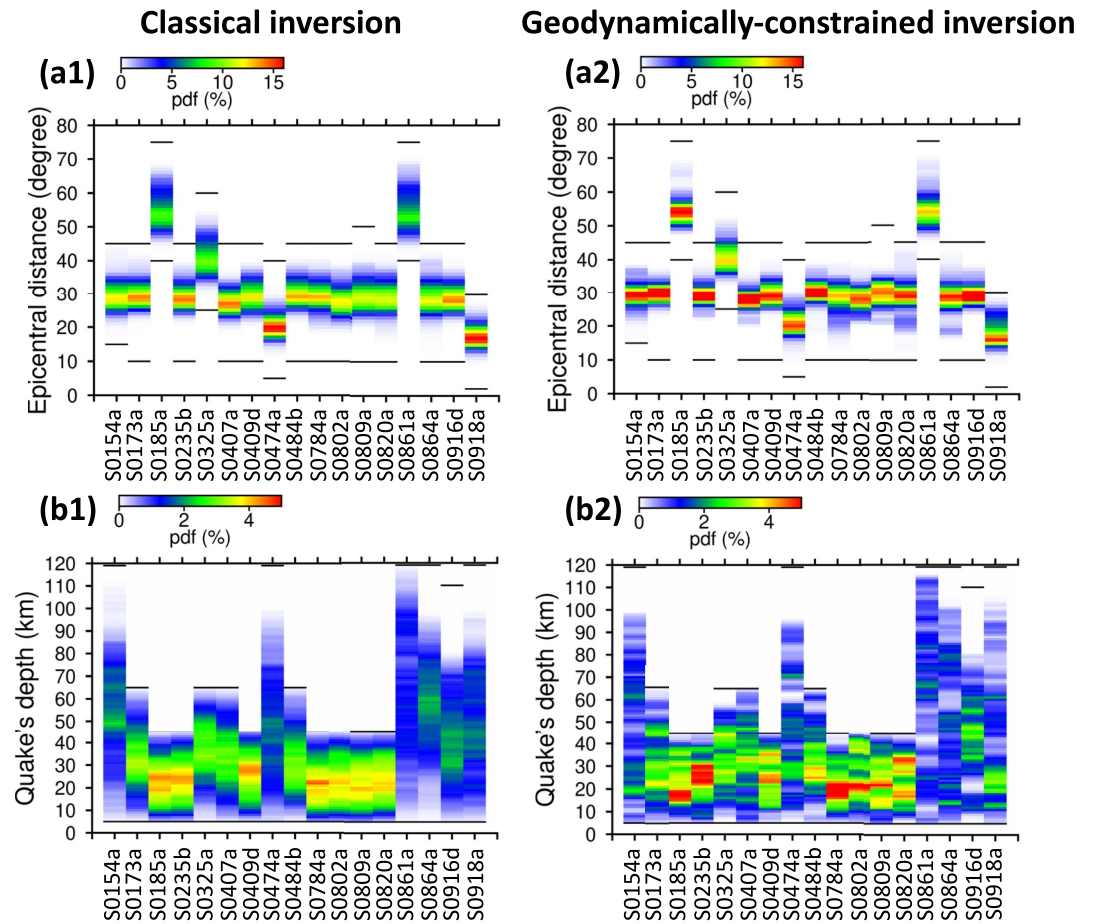
Figure 5. *A posteriori* probability density functions (pdfs) of the epicentral distances (a1 and a2) and quake depths (b1 and b2) of the 17 marsquakes, for the classical and geodynamic approaches. Blue and red colors show small and large probabilities, respectively. The pdf is computed by counting the number of sampled models in each of the case. The discretizations are 1° and 1 km for the epicentral distances and the quake depths, respectively. The black lines show the prior bounds, estimated at the end of the first stage of the inversion process (see Section 4.4). For a given marsquake, the sum of the pdf over all the parameter intervals is equal to 100%.

fundamental mode surface wave, the signal would not be observable because its amplitude would be within the instrument noise (below 0.1 Hz).

Because the event depth distributions are rather asymmetric compared to those of the epicentral distances, we prefer to use the mode instead of the mean as a measure to characterize the quake depth distributions in Table 3. The shapes of the model distributions obtained with the geodynamic method (Figure 5b2) are more multimodal compared to those of the classical parameterization (Figure 5b1), because of the stronger non-linearity between the geodynamic parameters and the arrival times, compared to the relationships between the seismic parameters and the data.

Figure 6 shows the marsquake locations determined in our study with the geodynamically constrained inversion, projected on a global topographic map inferred from the Mars Orbiter Laser Altimeter (Smith et al., 2001). The latitude and longitudes of the marsquakes are summarized in Table 3. Most of the marsquakes are located East of the InSight lander, and 12 of them are concentrated near the major fracture zones of Cerberus Fossae and Grjótá Valles. In Section 6.1, we discuss how such shallow marsquakes could be related to tectonic features observed at the surface of the planet by orbiters.

Table 3
Summary of the Mean Epicentral Distances and Marsquake Depths

Event	Mean epicentral distance (°)		Marsquake depth (km)		Latitude and longitude (°)	
	Classical inversion	Geodynamically constrained inversion	Classical inversion	Geodynamically constrained inversion	Classical inversion	Geodynamically constrained inversion
S0154a	29.3 ± 3.4	29.4 ± 2.8	48.8 ± 20.0	19.0 ± 37.7	5.40, 165.02	5.40, 165.11
S0173a	29.7 ± 3.0	29.8 ± 2.0	29.2 ± 12.9	23.7 ± 16.9	4.80, 165.42	4.80, 165.52
S0185a	55.1 ± 4.6	54.2 ± 2.9	24.1 ± 8.6	17.3 ± 10.7	42.23, 90.04	41.76, 91.09
S0235b	29.1 ± 2.9	29.3 ± 2.2	23.1 ± 8.8	24.0 ± 8.3	14.13, 163.53	14.18, 163.72
S0325a	41.1 ± 4.2	40.8 ± 3.2	34.0 ± 12.3	27.0 ± 13.1	−19.00, 170.06	−18.84, 169.78
S0407a	27.5 ± 2.8	27.9 ± 2.1	31.1 ± 12.7	33.1 ± 13.7	9.11, 162.94	9.16, 163.34
S0409d	29.5 ± 3.3	29.6 ± 2.5	27.1 ± 9.0	22.8 ± 9.2	7.89, 165.11	7.90, 165.21
S0474a	20.5 ± 2.6	21.1 ± 2.8	48.1 ± 20.4	29.5 ± 27.5	23.75, 143.49	24.30, 143.75
S0484b	30.2 ± 3.1	30.4 ± 2.3	25.3 ± 13.6	25.5 ± 14.4	12.47, 165.13	12.51, 165.33
S0784a	29.4 ± 3.6	28.6 ± 3.4	22.3 ± 8.7	19.8 ± 7.6	−1.26, 164.49	−1.10, 163.70
S0802a	28.0 ± 3.4	28.1 ± 2.7	23.1 ± 9.1	20.9 ± 11.0	6.34, 163.69	6.34, 163.79
S0809a	29.6 ± 3.5	29.7 ± 2.7	18.6 ± 9.9	21.2 ± 9.5	5.78, 165.31	5.78, 165.41
S0820a	29.2 ± 3.5	28.7 ± 3.9	19.3 ± 10.0	34.0 ± 12.6	6.88, 164.87	6.85, 164.37
S0861a	55.1 ± 5.0	54.5 ± 3.7	55.6 ± 27.0	66.6 ± 30.3	37.31, 86.83	37.06, 87.52
S0864a	29.1 ± 3.7	28.5 ± 3.4	58.9 ± 18.3	15.2 ± 42.6	4.91, 164.82	4.91, 164.21
S0916d	29.0 ± 2.9	29.4 ± 2.0	32.9 ± 18.7	46.7 ± 16.8	13.15, 163.69	13.26, 164.09
S0918a	17.6 ± 2.6	18.3 ± 3.2	44.0 ± 20.3	22.9 ± 30.3	−12.38, 141.25	−13.05, 141.49

Note. The 1σ standard deviations are also indicated. The last two columns are the latitude and longitude coordinates, computed from the back-azimuth values in Table 1 (BAZ-Best) and the mean epicentral distance values.

5.2. Data Fit

The data fits of all the differential arrival times for the 17 marsquakes, as described in Equation 1, are displayed in Figure 7. The data and the 1-σ uncertainties are shown in black. For both methods, all the accepted models by the algorithm can fit the observational $t_S - t_P$ data within error bounds (Figures 7a1 and 7a2).

Unsurprisingly, Figures 7b1–7e1 and 7b2–7e2 show that the data fits computed for the multiples ($t_{PP} - t_P$, $t_{PPP} - t_P$, $t_{SS} - t_S$, and $t_{SSS} - t_S$) are globally better for S-phases compared to P-phases, because the P, PP, and PPP arrivals are more difficult to pick and have a smaller amplitude, as explained in Section 2. Concerning the two farthest marsquakes (S0185a and S0861a), the distributions of the data fits estimated on the multiples are more spread for the classical method (Figures 7b1–7e1) compared to the geodynamic method (Figures 7b2–7e2). The geodynamically constrained approach allows the application of relatively tight constraints to the mantle velocity structure, by generating consistent velocity models through the entire planet, which reduces the range of possible models. In contrast, the classical models provide constraints only at the depths where the data are most sensitive to the seismic structure. Since only the three farthest marsquakes (S0185a, S0325a, and S0861a) allow the structure between 400 and 700 km depth to be constrained, as seen in Appendix D, the classical models are less constrained at these depths. On the other hand, the physical assumptions made in the geodynamic approach allow to reduce the model distribution, yielding tighter data fit distributions.

The data fits estimated on P and S depth phases ($t_{pP} - t_P$, $t_{sS} - t_S$, and $t_{sP} - t_P$) are displayed in Figures 7f1–7h1 and 7f2–7h2. Again, the data fits are better for S-phases compared to those for P-phases. Among the 17 marsquakes, 10 of them show clear ScS arrivals (Figures 7i1 and 7i2), which are used to constrain the radius of the core.

Based on the data fit calculations, we can argue that the majority of models accepted by both the classical and geodynamic methods fit the data within uncertainty bounds, which means that almost all the sampled models are able to explain the data. Among the different causes that are certainly responsible for deviations of calculated
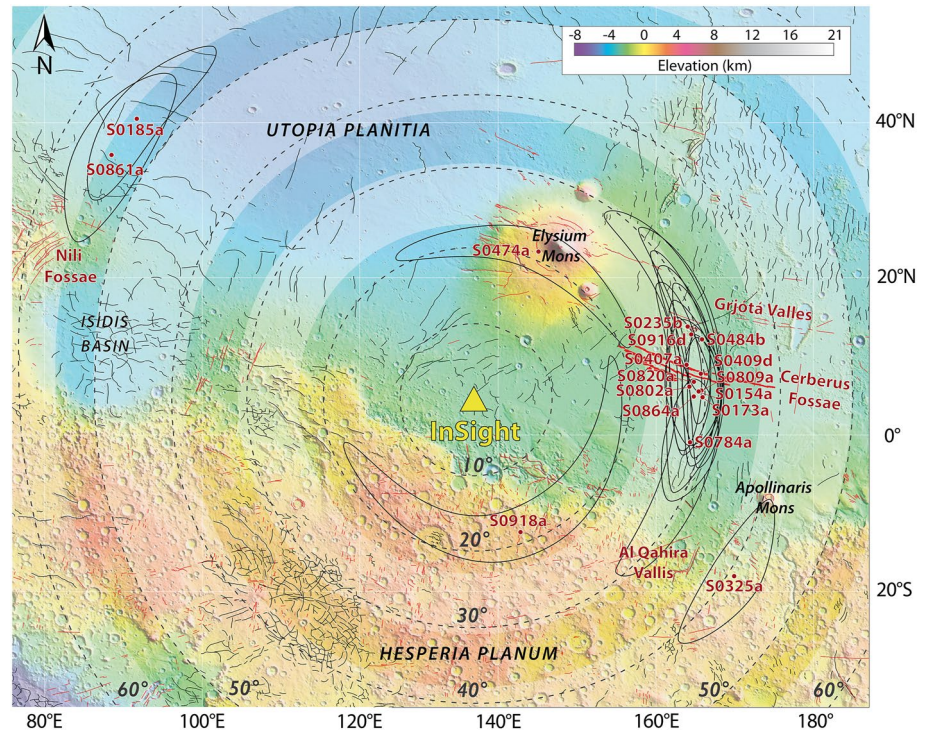
Figure 6. Topographic map of Mars (Mars Orbiter Laser Altimeter data) showing the main tectonic structures around InSight (shown as a yellow triangle) which landed on an ancient volcanic plain south of Elysium Mons and north of the Martian hemispheric dichotomy. Red and black lines are global compilation of normal and reverse faults, respectively (Knapmeyer et al., 2006). The thick red lines highlight the Cerberus Fossae graben system (Giardini et al., 2020; Perrin et al., 2022). Circular dotted lines are distances from the InSight lander in degree. Shaded white bands are areas of main seismicity locations from Giardini et al. (2020). Event locations from this study are indicated by the red dots associated with their uncertainties (black ellipses). See text for details.

versus measured arrival times; the small P-phase amplitudes (which make them difficult to pick), the presence of noise, and the fact that the modeling is based on spherically symmetric models, all likely play a major role.

5.3. 1-D Seismic Models

Following Drilleau et al. (2021), for a better analysis of the output 1-D seismic models, we use two different representations. Figure 8 represents the *a posteriori* pdf on V_S, V_P, and on the V_P/V_S ratio profiles. The pdfs provide an overview of the most frequently sampled models, and show the additional gain in information obtained through the inversion, compared to the *a priori* distributions (Figure 4). Figure 9 displays in gray 15 models randomly selected in the ensemble models. The four models associated with the smallest misfit values are displayed in red. These selected models cannot be used to infer statistical properties, but they are useful to visualize the diversity of the models sampled.

We observe that the V_S and V_P output profiles from the classical and geodynamic approaches show a different behavior in the mantle (Figures 8a1 and 8a2). The geodynamically constrained V_S distribution clearly indicates a decrease of V_S down to 500 km depth, which is absent from the V_S distribution of the classical models. Figures 9a1 and 9b1 reveal different families of models in the mantle for the classical models. Indeed, several models show a negative velocity gradient, while other models do not. These results indicate that models with distinct characteristics can fit the same data. The S- and P-wave velocity gradient is therefore not constrained by our data set, and the negative velocity gradient found for V_S using the geodynamically constrained inversion is imposed by the *a priori* assumptions. The structure between 400 and 700 km depth is constrained by only three events (S0185a, S0325a, and S0861a). We tested their influence on the retrieved model parameters by dividing the error bars of their measured body wave arrival times by two, and observed minor differences in the output seismic velocity distributions.
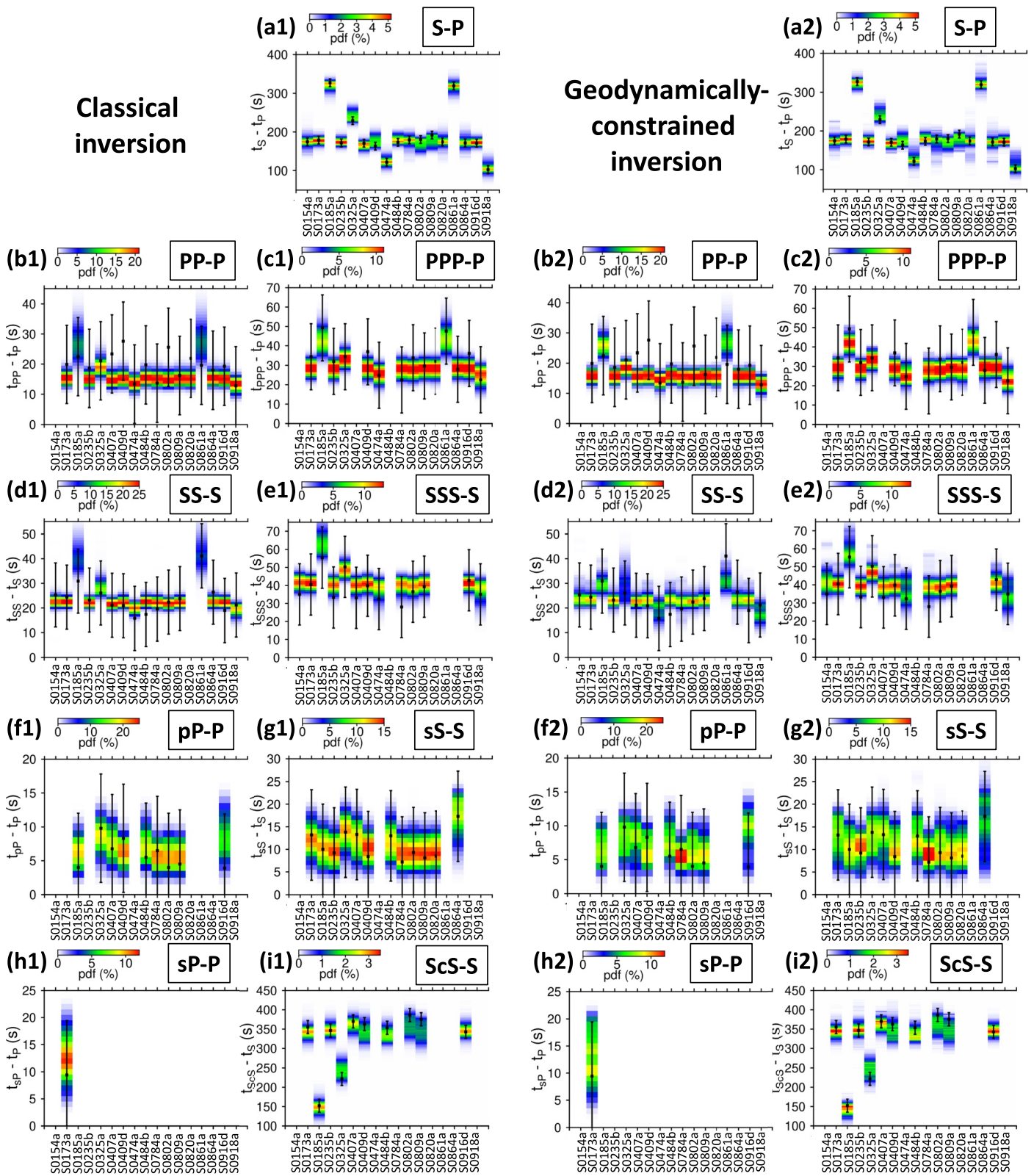
Figure 7. Data fit from the inversion of the body waves arrival times, considering 17 marsquakes, for the classical inversion (left panel) and the geodynamic inversion (right panel). The *a posteriori* probability density functions of $t_S - t_P$ differential arrival times are shown in panels (a1 and a2). The data fits calculated on P- and S-wave multiples ($t_{PP} - t_P$, $t_{PPP} - t_P$, $t_{SS} - t_S$, and $t_{SSS} - t_S$) are displayed in panels (b1–e1 and b2–e2), whereas those estimated for the depth phases ($t_{pP} - t_P$, $t_{sS} - t_S$, and $t_{sP} - t_P$) are shown in panels (f1–h1 and f2–h2). The data fits calculated on ScS ($t_{ScS} - t_S$) are shown in panels (i1 and i2). The measured data from Table 1 and the 1-σ uncertainties are represented in black.

Classical inversion

Geodynamically-constrained inversion
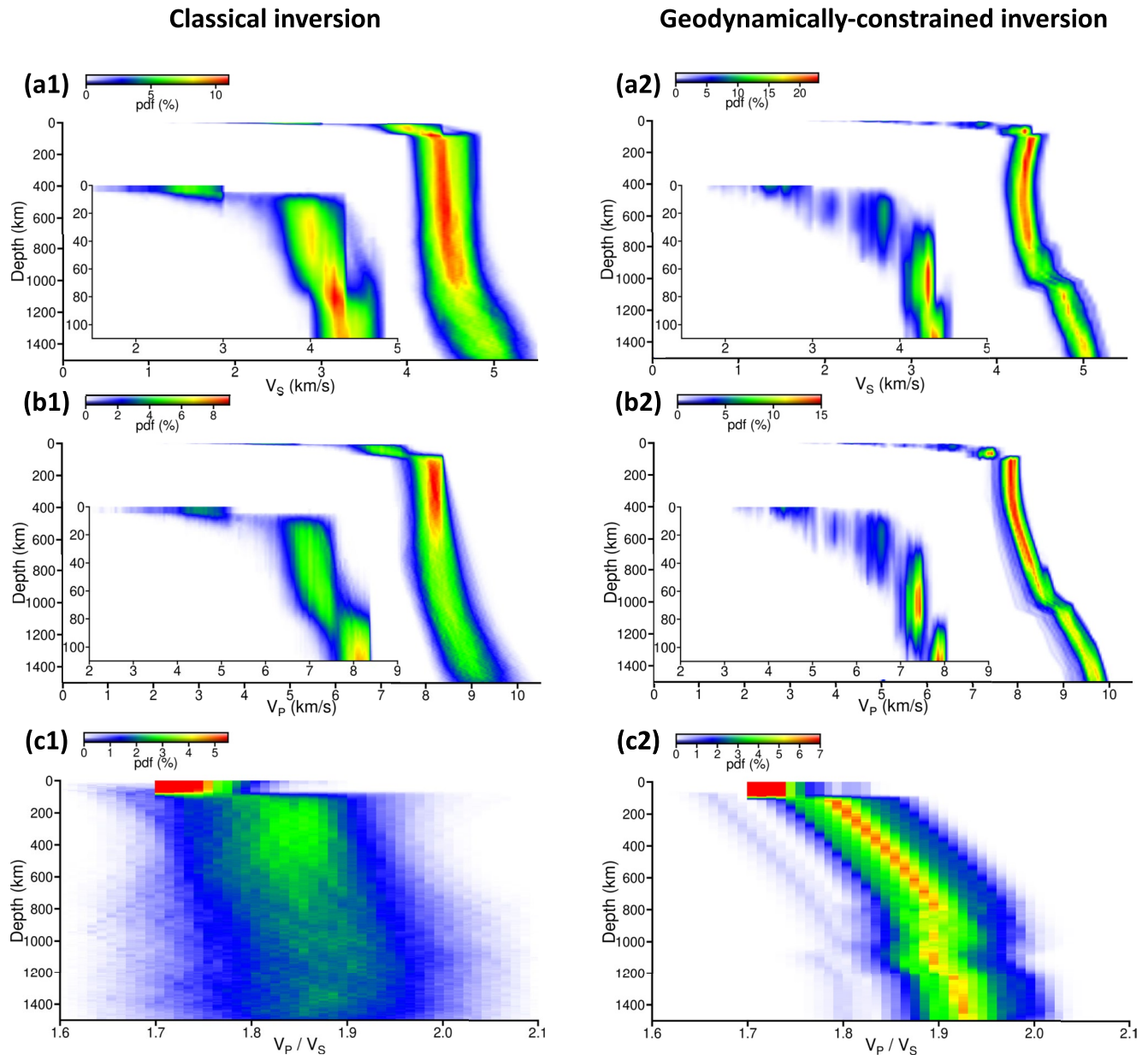
Figure 8. Inversion results using the classical approach (left) and the geodynamic approach (right). Panels (a1, a2, b1, b2) are *a posteriori* probability density functions (pdfs) of the 1-D V_S and V_P profiles, respectively. Panels (c1 and c2) are *a posteriori* pdfs of the V_P/V_S ratio. Blue and red colors show small and large probabilities, respectively. The pdf is computed by counting the number of sampled profiles in each of the cases. The discretization is 1 km for depth, 0.05 km/s for V_S and V_P, and 0.01 for the V_P/V_S ratio. For a given depth, the sum of the pdf over all the parameter intervals is equal to 100%. A zoom on the crust between the surface and 110 km depth is shown in panels (a1, a2, b1, b2).

Below ∼700 km depth, the pdfs become more spread in the parameter space (Figures 8a1–8b2) and the classical models (Figures 9a1 and 9b1) show a chaotic behavior, because our body wave data set is no longer sensitive to the structure at this depth (Appendix D). The location of the olivine-to-wadsleyite phase transition is thus not constrained with the classical parameterization. Thanks to the ScS phases, we retrieve core radii with values that are in good agreement with the previous study of Stähler et al. (2021), with $R_c = 1{,}817 \pm 87$ and $1{,}820 \pm 55$ km. The output marginal distributions of the core radius are displayed in Appendix E.

In the crust, both approaches indicate larger probabilities of the V_P/V_S ratio for values smaller than 1.8 (Figures 8c1 and 8c2), with a mean V_P/V_S ratio equal to 1.77 ± 0.04 and 1.73 ± 0.03 for the classical and the geodynamically constrained approaches, respectively. In contrast, the distribution of the V_P/V_S ratio in the mantle

Classical inversion

Geodynamically-constrained inversion
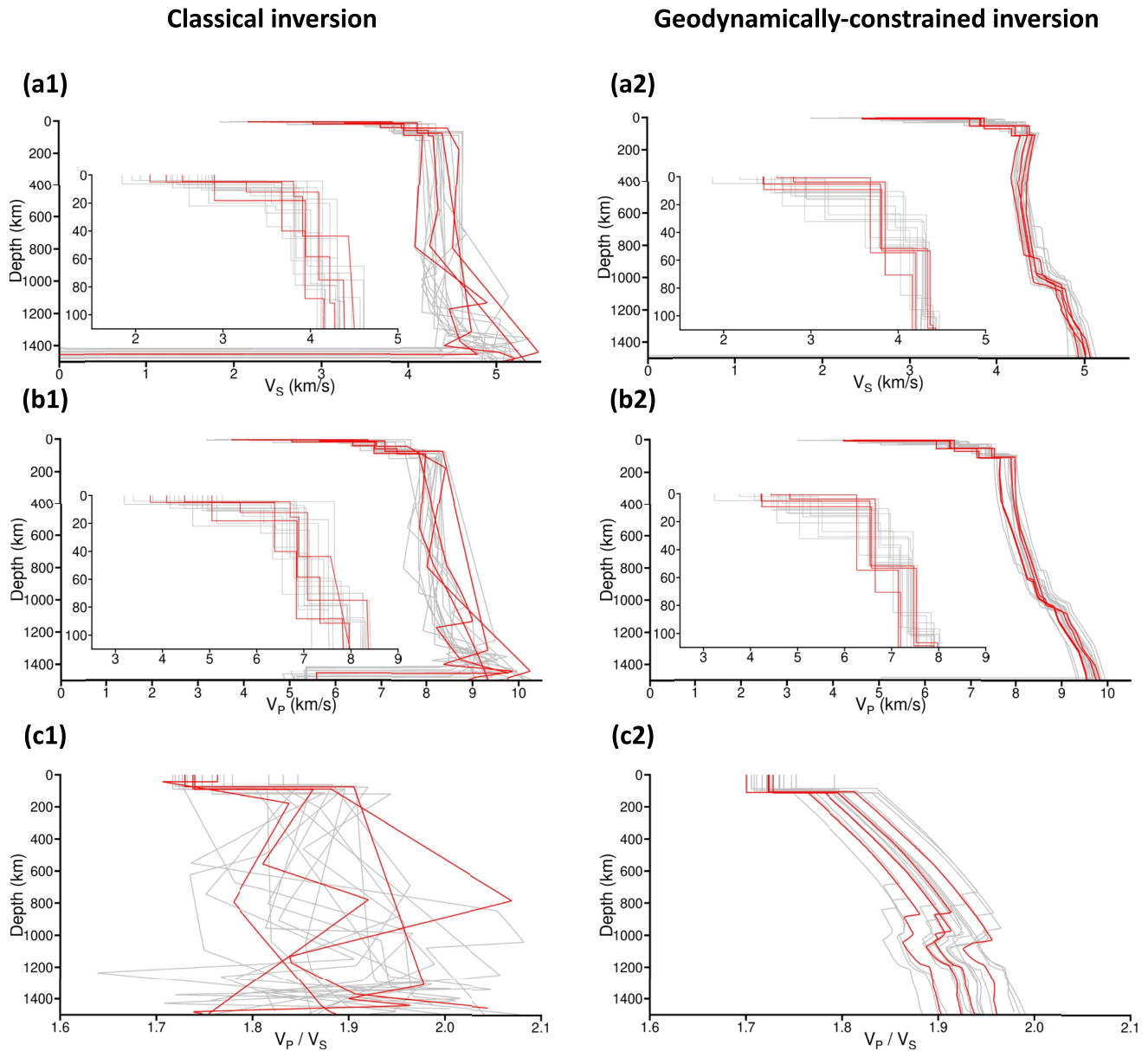
Figure 9. Inversion results using the classical approach (left) and the geodynamic approach (right). Panels (a1, a2, b1, b2, c1, c2), are the 1-D V_S, V_P, and V_P/V_S ratio profiles, respectively. The gray profiles represent a random subset of 15 models selected from the ensemble solution. Red profiles correspond to models with the four best misfits. A zoom on the crust between the surface and 110 km depth is shown in panels (a1, a2, b1, b2).

is broad (Figures 8c1 and 8c2). No evidence for a clear increase with depth is observed with the classical models (Figure 9c1), which indicates that the V_P/V_S ratio in the mantle remains poorly constrained by seismic data without a more informative prior.

Similar to the seismic velocities in the mantle (Figure 8), the V_S and V_P marginal posterior distributions in the upper, mid, and lower layers (Figures 10b and 10c), are broader for the classical model. Figures F1 and F2 in Appendix F show the correlation between the interface locations and the seismic velocities of the three crustal layers. Table 4 summarizes the mean V_S and V_P values in the three crustal layers. Within the three layers, larger seismic velocities are found for the geodynamically constrained models, compared to the classical models. In the lower crustal layer, the average value of the $V_{S_{lower}}$ distribution reaches $\sim$4.1 km/s, which is relatively close to the value of V_S at the top of the mantle.
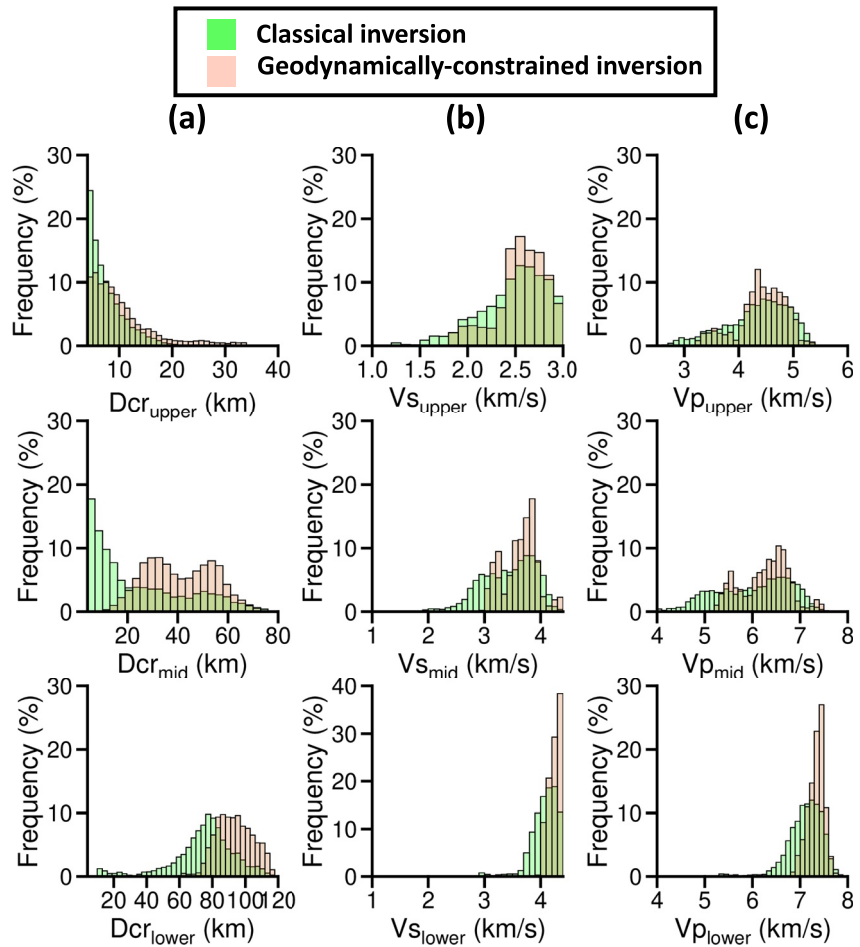
Figure 10. Output marginal distributions of the inverted parameters in the crust. The results of the classical and geodynamically constrained inversions are shown in green and pink, respectively. (a) Displays the layer's depth (Dcr). Panels (b and c) are the distributions of the P- and S-waves velocities. The subscripts $_{upper}$, $_{mid}$, and $_{lower}$ refer to parameters belonging to the upper, mid, and lower crusts, respectively.

A significant difference between the classical and geodynamically constrained approaches is observed on the distribution of the depths of the crustal layer interfaces (Figure 10a). A summary of the mean and the standard deviation can be found in Table 4. The classical models make fewer assumptions on the depth of the structural discontinuities, while in the case of the geodynamically constrained models, the Moho depth, that we consider here to be the base of the lower crustal layer (Dcr_{lower}), is directly estimated in the forward problem, as it results from the values of the geodynamic governing parameters sampled. Since these constraints are absent in the classical inversion, a large range of possible crustal thickness values is allowed for the classical models. Indeed, the marginal Dcr_{lower} distribution of the classical models is very broad, with a mean value of 75.0 ± 19.5 km. On the other hand, the strong prior induced by the geodynamically constrained approach reduces the range of possible Dcr_{lower} values with a mean value of 93.5 ± 11.0 km (Figure 10a). The distribution of the upper and mid crustal thicknesses are clearly in favor of thinner layers, compared to the lower crust, in particular for the classical models. The depths of the upper and mid crust interfaces are larger for the geodynamically constrained models, compared to those for the classical models (Figure 10a), again because of the constraints on the Moho depth (or Dcr_{lower}) mentioned above.

The good agreement between observed and computed travel times (Figure 7) confirms that the classical and geodynamic approaches are able to constrain distributions of 1-D average seismic models compatible with the data. Despite the large uncertainties on the location of the crustal layers' location (Table 4), an important result is that a lower crust with relatively high seismic velocities (with $V_S \sim 4.1$ km/s and $V_P \sim 7.2$ km/s), in a significant

Table 4
Summary of the Depths of the Crustal Layer Interfaces (Dcr_{upper}, Dcr_{mid}, Dcr_{lower}), the S- and P-Waves Velocities (V_S, V_P) in the Three Crustal Layers, and the V_P/V_S in the Whole Crust

	No crustal constraints		With crustal constraints	
	Classical inversion	Geodynamically constrained inversion	Classical inversion	Geodynamically constrained inversion
Dcr_{upper} (km)	7.7 ± 3.5	8.2 ± 6.5	20.7 ± 1.9	20.9 ± 2.3
Dcr_{mid} (km)	24.5 ± 18.9	41.0 ± 13.5	33.8 ± 3.9	30.1 ± 3.1
Dcr_{lower} (km)	75.0 ± 19.5	93.5 ± 11.0	53.7 ± 5.0	60.9 ± 1.5
$V_{S_{upper}}$ (km/s)	2.5 ± 0.3	2.6 ± 0.3	2.8 ± 0.1	2.7 ± 0.1
$V_{S_{mid}}$ (km/s)	3.4 ± 0.5	3.6 ± 0.3	3.7 ± 0.3	3.8 ± 0.3
$V_{S_{lower}}$ (km/s)	4.1 ± 0.2	4.2 ± 0.1	4.1 ± 0.2	4.3 ± 0.1
$V_{P_{upper}}$ (km/s)	4.3 ± 0.6	4.4 ± 0.4	5.0 ± 0.3	4.7 ± 0.3
$V_{P_{mid}}$ (km/s)	6.0 ± 0.8	6.3 ± 0.5	6.5 ± 0.6	6.6 ± 0.5
$V_{P_{lower}}$ (km/s)	7.1 ± 0.4	7.3 ± 0.2	7.2 ± 0.4	7.5 ± 0.1
V_P/V_S	1.77 ± 0.04	1.73 ± 0.03	1.76 ± 0.04	1.73 ± 0.02

Note. The subscripts $_{upper}$, $_{mid}$, and $_{lower}$ refer to parameters associated with the upper, mid, and lower crusts, respectively. The results with no crustal constraints are described in Section 5.3, and those with crustal constraints in Section 5.4.

part of the entire crust, is required to explain the data. However, due to the trade-offs between the parameters (in particular the seismic velocities in the crust and in the mantle), and the depth of crustal discontinuities, the solution remains strongly non-unique. Such a non-uniqueness of the solution is particularly amplified by the uncertainty on the Moho depth.

5.4. Additional Constraints on the Crustal Thickness

As shown in Drilleau et al. (2021), independent constraints on the crustal thickness can help to reduce the trade-offs between the governing parameters.

The majority of the events are located in the vicinity of Cerberus Fossae and Grjótá Valles, with a surface elevation that changes little along the path to the InSight landing site (Figure 6). However, considering back-azimuth uncertainties, five marsquakes (S0325a, S0474a, S0784a, S0861a, and S0918a) potentially show significant lateral variations of the surface elevation along the ray paths. These lateral variations are mainly related to crustal thickness variations between the southern highlands and northern lowlands (Neumann et al., 2004; Wieczorek & Zuber, 2004).

To take into account these variations in our 1-D models, we made the assumption that the average crustal thickness as seen by the seismic body waves is not too different from the mean crustal thickness within a circle of 60° radius around the InSight lander. This region includes all the events we considered in our data set since our farthest marsquake is located near 55° of epicentral distance.

We therefore estimated the mean crustal thickness within a circle of 60° radius around the InSight lander from gravity and topography measurements using the approach of Wieczorek et al. (2019) and considering the crustal thickness at the InSight landing site as determined in Knapmeyer-Endrun et al. (2021) as an anchoring point. Following Knapmeyer-Endrun et al. (2021), we considered different interior pre-landing models (Smrekar et al., 2019) that specify the density profiles of the mantle and the core. For each interior model, global crustal thickness models were constructed for a range of crustal densities between an assumed lower limit of 2,550 kg/m³ and the maximum value allowed by each model.

We considered here that the Martian crust is composed of three units. In this case, the receiver function analysis carried out in Knapmeyer-Endrun et al. (2021) has constrained the thickness ranges for each of the three crustal layers in terms of Gaussian distributions: 8 ± 2, 20 ± 5, and 39 ± 8 km beneath the seismic station. Because the seismic wave arrival times considered here are computed in spherically symmetric models, we make the assump-

Classical inversion

Geodynamically-constrained inversion
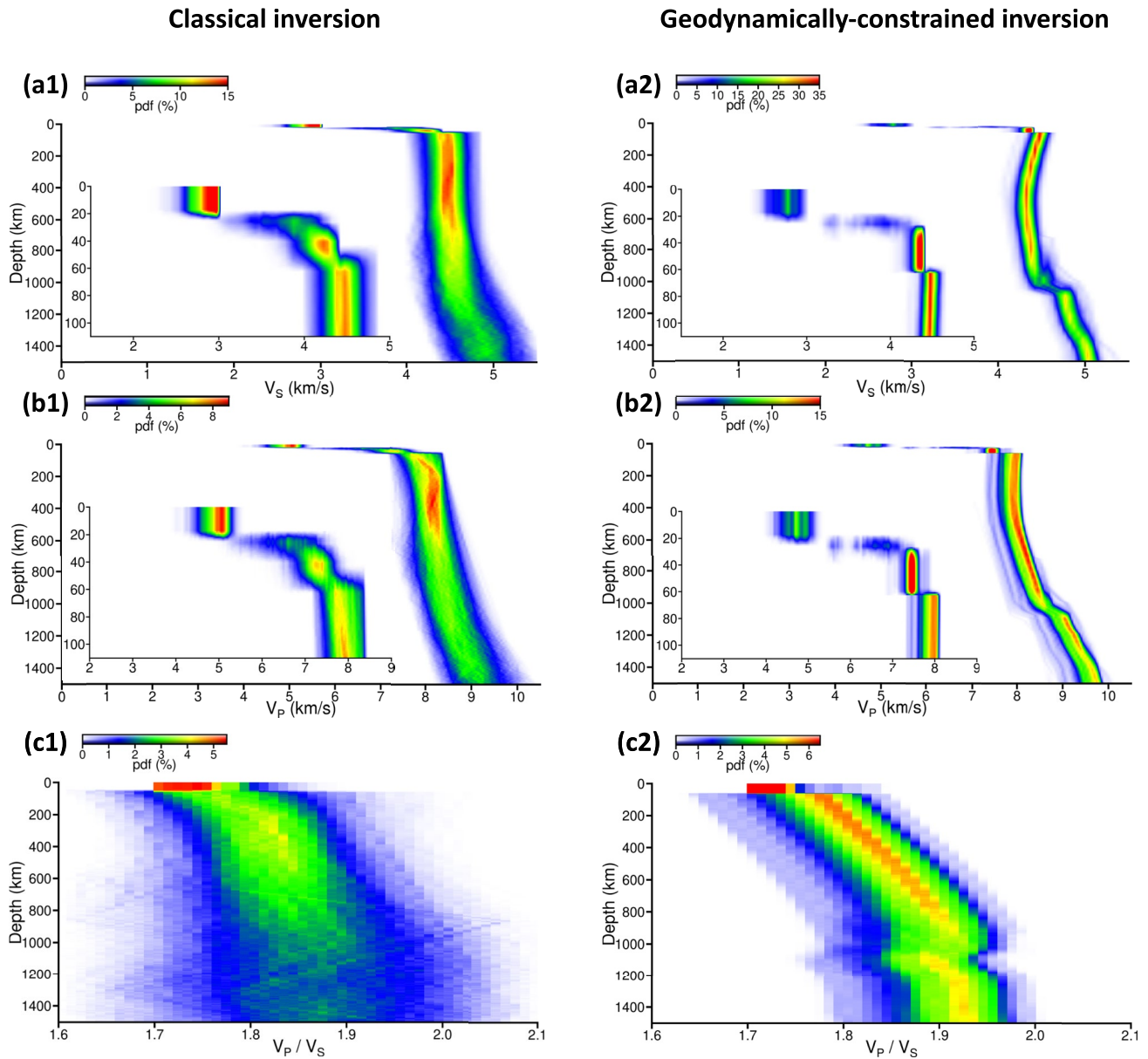
Figure 11. Inversion results using the classical approach (left-hand panel) and the geodynamic approach (right-hand panel), considering a restricted prior range on the location of the upper, mid, and lower crustal layer. Panels (a1, a2, b1, b2) are *a posteriori* probability density functions (pdfs) of the 1-D V_S and V_P profiles, respectively. Panels (c1 and c2) are *a posteriori* pdfs of the V_P/V_S ratio. Blue and red colors show small and large probabilities, respectively. The pdf is computed by counting the number of sampled profiles in each of the cases. The discretization is 1 km for depth, 0.05 km/s for V_S and V_P, and 0.01 for the V_P/V_S ratio. For a given depth, the sum of the pdf over all the parameter intervals is equal to 100%. A zoom on the crust between the surface and 110 km depth is shown in panels (a1, a2, b1, b2).

tion that the three crustal interfaces (whose thicknesses will be determined by our inversion scheme) exist at the global scale.

Here, we randomly varied the thickness of the deepest interface underneath the InSight lander between the range inferred in Knapmeyer-Endrun et al. (2021) (i.e., 31 and 47 km) and obtained the pdf for the crustal thickness average in a circle of 60° around the lander following the approach in Wieczorek et al. (2019). The retrieved mean crustal thickness of Mars from the ensemble of crustal thickness models averaged in the 60° circle around the lander is found to be 52.5 ± 10 km. This range is narrower compared to the global average range 39–72 km inferred in Knapmeyer-Endrun et al. (2021) meaning that our constraint on crustal thickness is more restrictive. Then, we apply the same mapping to obtain the pdf for the intra-crustal layer thicknesses. This corresponds to

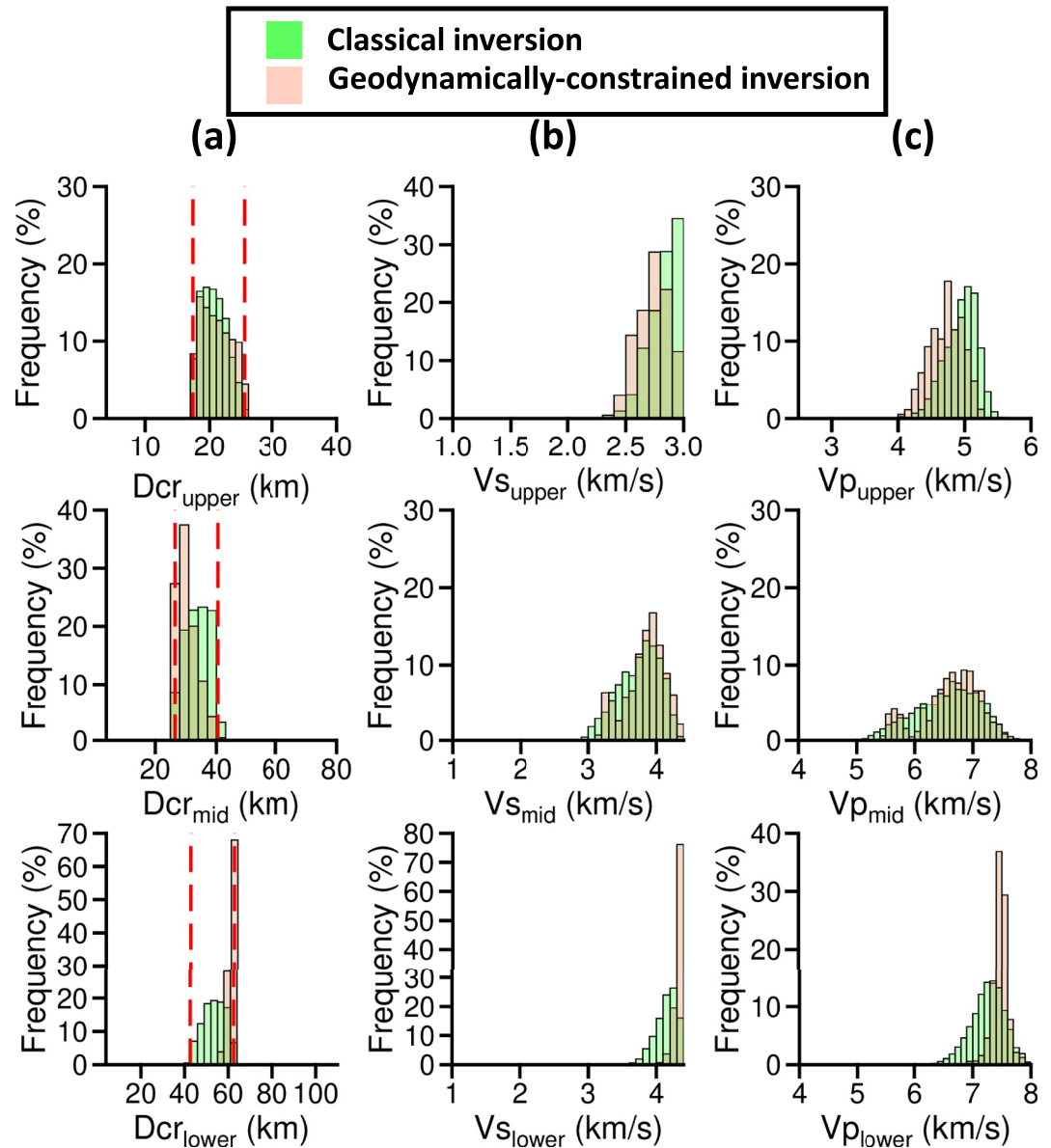## Classical inversion　　　　Geodynamically-constrained inversion
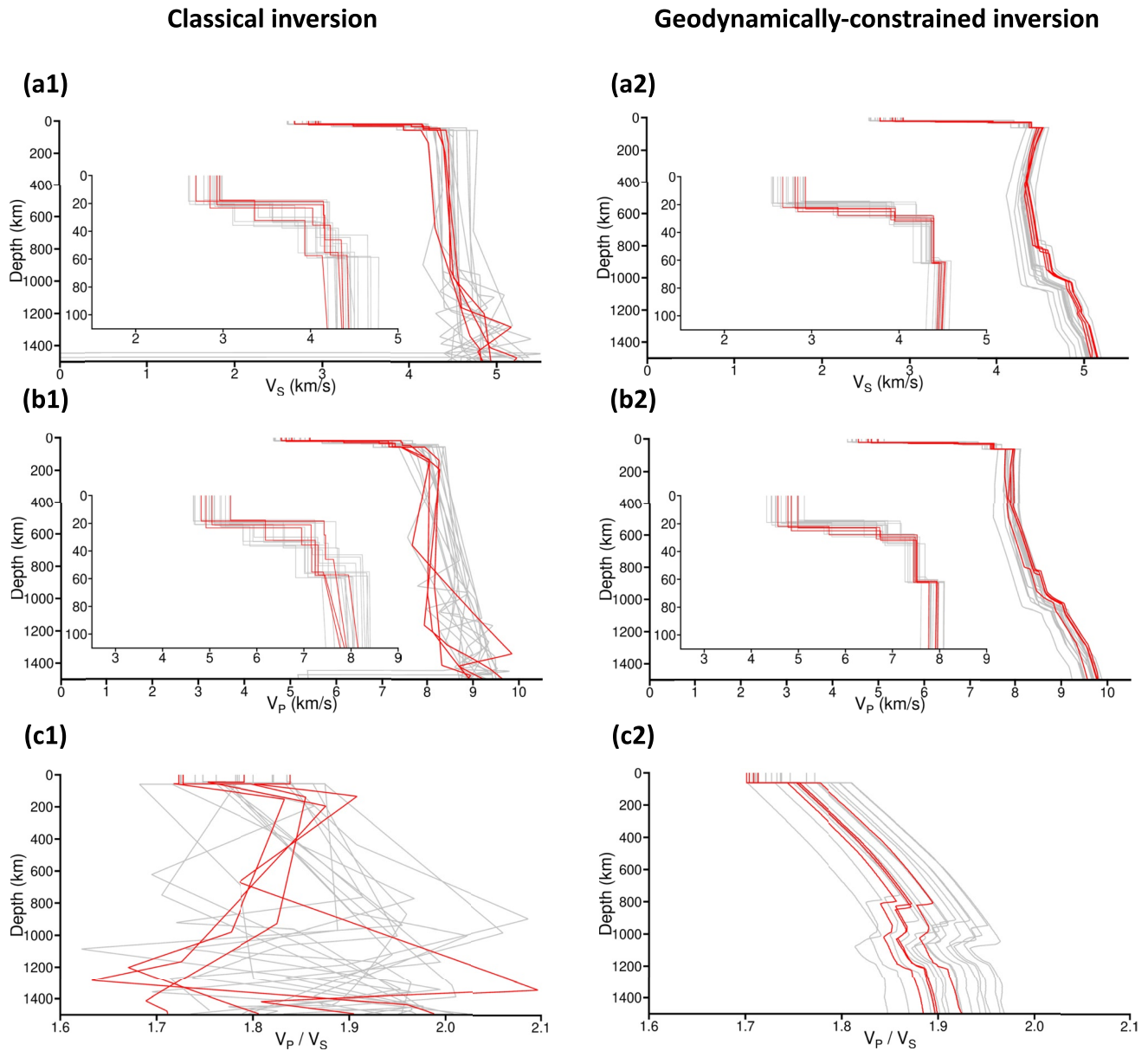
Figure 12. Inversion results using the classical approach (left panels) and the geodynamic approach (right panels), considering a restricted prior range on the location of the upper, mid, and lower crustal layer. Panels (a1, a2, b1, b2, c1, c2), are the 1-D V_S, V_P, and V_P/V_S ratio profiles, respectively. In gray are shown a random subset of 15 models selected from the ensemble solution. Red lines are the profiles corresponding to the four best misfits. A zoom on the crust between the surface and 110 km depth is shown in panels (a1, a2, b1, b2).

an upper and mid crustal interfaces located on average at 21.5 ± 4 and 33.5 ± 7 km. To investigate the extent to which the retrieval of the parameters could be improved if the locations of the crustal interfaces and the Moho depth were considered to be known, we restricted the depth range of the upper, mid, and lower crustal layers in our inversions using the above values (note that the *a priori* on the geodynamic parameters are not modified).

When the above constraints on the crustal thickness are applied, the trade-off between the parameters decreases, in particular for the geodynamically constrained models (Figures 11 and 12). Indeed, the possible range of Moho depths (Dcr$_{lower}$) is very limited for these models (Figure 13a), with a mean Dcr$_{lower}$ value equal to 60.9 ± 1.5 km (Table 4). In the mantle down to 700 km depth, the geodynamically constrained models (such as those displayed in Figures 12a2 and 12b2) show that the range of V_S and V_P gradient values are more limited compared to the results obtained with no constraints on the depth range of the crustal layers (Figures 9a2 and 9b2). However,
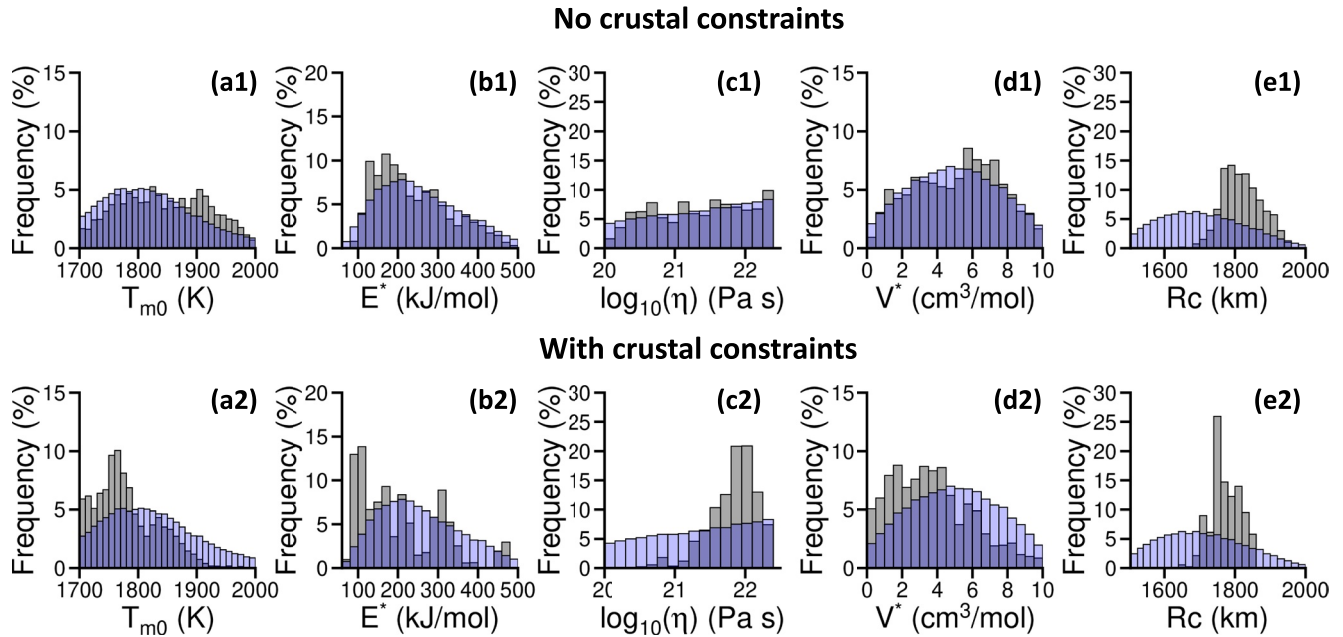
Figure 13. Output marginal distributions of the inverted parameters in the crust, considering a restricted prior range on the location of the upper, mid, and lower crustal layer. The results of the classical and geodynamically constrained inversions are shown in green and pink, respectively. (a) Displays the layer's depth (Dcr). Panels (b and c) are the distributions of the P- and S-waves velocities. The subscripts $_{upper}$, $_{mid}$, and $_{lower}$ refer to parameters belonging to the upper, mid, and lower crusts, respectively. The red dashed lines in panel (a) mark the allowed depth range.

no clear low velocity zone is observed in the upper mantle with the classical models (Figures 11a1 and 11b1). The V_S and V_P pdfs are narrower when constraints on the depth of the crustal layers are added, and the V_P/V_S ratio clearly increases with depth down to ~500 km depth for the classical models (Figure 11c1), which was not observed when no constraints are considered (Figure 8c1). In the crust, the V_S, V_P, and V_P/V_S mean values inferred from both methods are in good agreement, and are relatively similar to the ones estimated without constraints on the depth range of the three crustal layers (Table 4). The values are slightly shifted toward larger values due to trade-off between the depth of the layer and the seismic velocity, as detailed in Appendix F.

One should note that the seismic wave arrival times considered in this paper are computed in spherically symmetric models, and under the hypothesis that the three crustal layers are present at the global scale. However, possible causes of seismic wavefield complexity such as 3-D structure and anisotropy, most likely complexify the inter-

No crustal constraints

With crustal constraints

Figure 14. Marginal posterior distributions of the geodynamic governing parameters using (top) no constraint and (bottom) constraints on the crustal thickness. Panels (a1 and a2) are the distributions of the initial temperature below the lithosphere T_{m_0}, (b1 and b2) the effective activation energy $E*$, (c1 and c2) the reference mantle viscosity η_0, (d1 and d2) the activation volume $V*$, and (e1 and e2) the core radius R_c. The blue and gray histograms correspond to the *a priori* and *a posteriori* distributions, respectively.

pretation as a 1-D radial model. Because the InSight lander and the marsquakes are located close to the crustal dichotomy (see Section 6.1), significant lateral variations of the relief along the crust-mantle interface and the surface relief can potentially affect the seismic wave arrival times. Preliminary tests we performed have shown that uncertainties on the back azimuths can result in arrival time variations of several percent.

5.5. Constraints on the Geodynamic Parameters and Temperature Profile

The distributions of a selection of geodynamic parameters are shown in Figure 14, and their mean values, 1-σ standard deviations and min-max ranges are summarized in Table 5.

Table 5
Summary of the Mean Values, 1-σ Ranges, and Min-Max Ranges of the Initial Temperature Below the Lithosphere T_{m_0}, the Effective Activation Energy $E*$, the Reference Mantle Viscosity η_0, and the Crustal Enrichment Factor Relative to the Primitive Mantle Λ

	No crustal constraints	With crustal constraints
T_{m_0} (K)	Same as prior	1,781 ± 53 (1,700–1,997)
T_{c_0} (K)	Same as prior	2245 ± 81 (2017–2497)
$E*$ (kJ/mol)	Same as prior	205 ± 102 (70–469)
η_0 (Pa s)	Same as prior	$10^{21.9\pm0.4}$ ($10^{20.4}$–$10^{22.5}$)
Λ	8 ± 2 (5–13)	12 ± 2 (5–15)
R_c (km)	1,820 ± 55 (1,595–1,970)	1,773 ± 41 (1,652–1,859)

Note. The min-max ranges are indicated in the parentheses. The values listed correspond to the 10^4 output models that have the smallest misfit, as displayed in Figure 15. "Same as prior" indicates that the *a priori* and *a posteriori* marginal distributions are similar, meaning that the associated parameter is not well constrained by the data set.

When no constraints are considered on the crustal thickness (Figure 14a), a large number of combinations of the initial temperature below the lithosphere T_{m_0}, the effective activation energy $E*$, the reference mantle viscosity η_0, and the activation volume $V*$, can satisfy the data equally well. With the exception of the core radius R_c the *a posteriori* marginal distributions (Figure 14a, in gray) are similar to the *a priori* marginal distributions (Figure 14a, in blue), indicating that our data set is not sensitive to the values of these geodynamic parameters.

As seen in Section 5.4, adding constraints on the crustal thickness leads to a significant reduction of the trade-offs between the geodynamic parameters (Figure 14b). The uncertainty on the effective activation energy $E*$ is still large, with a mean value equal to 205 ± 102 kJ/mol. However, the *a posteriori* and *a posteriori* marginal distributions of T_{m_0} and η_0 are different and significantly narrower compared to the ones obtained when no assumptions are considered on the depth of the crustal layers, with mean values equal to 1,781 ± 53 K and $10^{21.9}$ ± $10^{0.4}$ Pa s, respectively (Table 5). As suggested in Drilleau et al. (2021) and Khan et al. (2021) these results show that further insight into the value of the geodynamic quantities can be gained
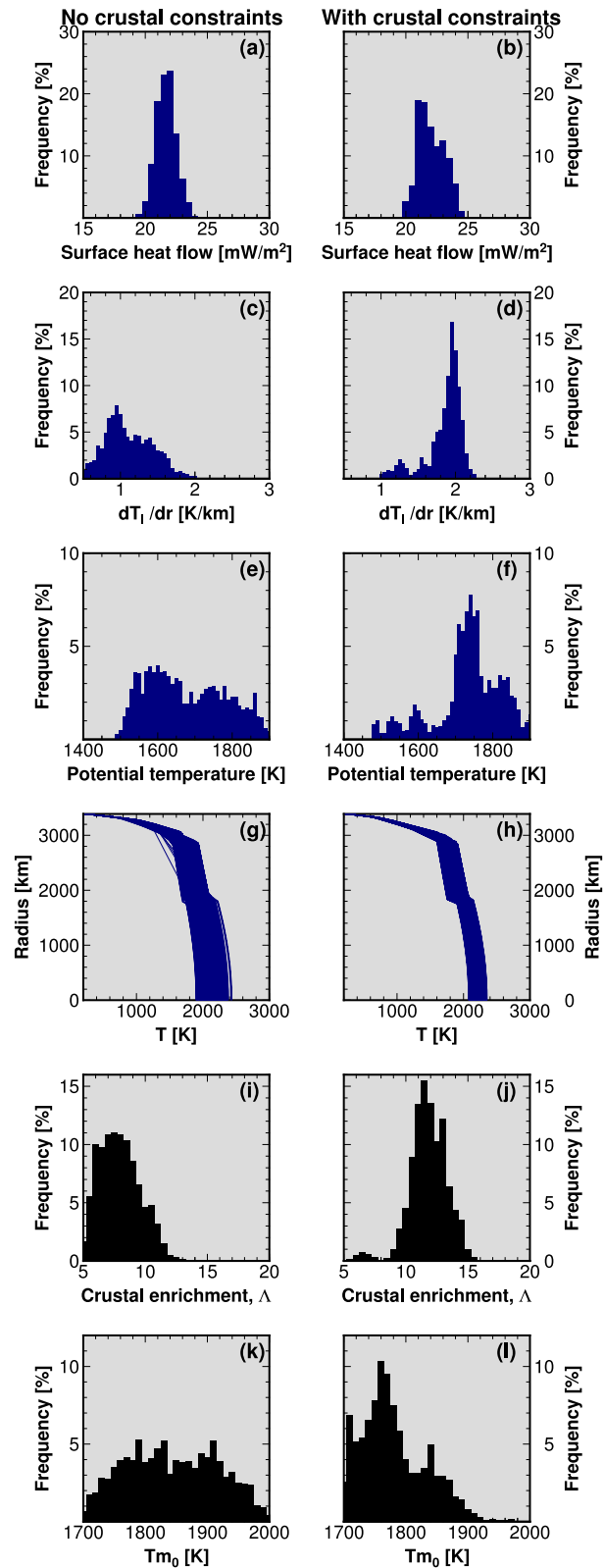
Figure 15.

by considering constraints on the present-day crustal thicknesses. However, even in this case, V^* remains poorly constrained by our data set (see corresponding histograms in Figure 14b).

Figure 15 shows the prior distributions of several present-day quantities obtained with the geodynamically constrained inversions with or without constraints on the crustal thickness. The present-day average surface heat flow is similar for inversions without and with crustal constraints (Figures 15a and 15b) and mostly ranges between 20 and 25 mW/m^2. This similarity results from the fact that the present-day heat flow is primarily determined by the total amount of HPEs in the bulk silicate mantle, which is the same in both inversions. In addition, these heat flow values are comparable to, or smaller than previous estimates (Khan et al., 2021; Knapmeyer-Endrun et al., 2021), because here we have considered a primitive mantle that has a comparable or a smaller amount of HPE, as described in Section 4.1.2. This results in similar and relatively well constrained temperature profiles at shallow depth (i.e., in the crust) in both cases (Figures 15g and 15h).

In contrast to heat flow values, applying crustal constraints along the inversion process yields considerably narrower distributions for several other present-day and initial quantities, which often correspond to distinct regions of the model domain. Indeed, despite the similar gradients in the crust (Figures 15g and 15h), the two inversions show very different and partly non-overlapping distributions of the temperature gradient in the lithosphere (Figures 15c and 15d). The distributions tend to be broader for the inversion without crustal constraints (Figure 15c), and have smaller values compared to those obtained for the inversion with crustal constraints (Figure 15d). This narrower distribution confirms that seismic data with crustal constraints (that also involve gravity and topography data (Knapmeyer-Endrun et al., 2021)) combined with geodynamic considerations can significantly constrain the Martian lithospheric temperature profile. This observation, also noted in Khan et al. (2021), is due to the fact that the seismic data combined with considerations on temperature in the lithosphere and in uppermost mantle can put strong requirements on the seismic velocity gradients in the first 700 km below the Martian surface, which relate to the thermal state of the lithosphere.

Similarly, the present-day potential temperature (T_p) distribution for the inversion without constraints on the crustal thickness (Figure 15e) is broad and multi-modal, with values ranging between 1490 and 1950 K with a 1-σ range $T_p = 1678 \pm 106$ K. On the contrary, the inversions with crustal constraints result in mono-modal and a considerably hotter and narrower distribution with a 1-σ range $T_p = 1736 \pm 92$ K and a min-max range of 1470–1940 K (Figure 15f). Note that the hottest values correspond to thicker lithospheres such that there is no large-scale shallow melting in the mantle at the present-day. Altogether, this results in a narrower range for the present-day thermal structure in the constrained inversions (Figure 15h) compared to that of the inversion without crustal constraints (Figure 15g). Our inversions also allow constraining the crustal enrichment factor, Λ (Section 4.1.2). If no crustal constraints are applied, $\Lambda = 8.3 \pm 1.7$ (Figure 15i), while applying crustal thickness constraints yield to a narrower range with larger values: $\Lambda = 11.7 \pm 1.4$ (min-max range: 5–16, see Table 5 and Figure 15j). This latter range is in line with recent studies based on receiver functions, and gravity-topography data and geodynamic considerations (Knapmeyer-Endrun et al., 2021), and with studies on GRS data (Boynton et al., 2007). However, despite limited overlaps, our inferred range for crustal enrichment is smaller than the range ($\Lambda = 13 - 20$) inferred by seismic data combined with geodynamic considerations (Khan et al., 2021). This is likely due to the differences in the data set and the parameterization used, as explained below.

The initial thermal state is also better constrained in the inversions with crustal thickness requirements (see Figures 15k and 15l). The inversions with constraints on crustal thickness point toward an initially relatively cold mantle, as in previous work using similar constraints (Khan et al., 2021; Knapmeyer-Endrun et al., 2021).

Overall, the inversion results presented above are generally in good agreement with recent studies using seismic data to infer the shallow structure of Mars (Khan et al., 2021; Knapmeyer-Endrun et al., 2021). The differences that remain between our results and the previous inversions can be first attributed to differences in the data set, which contains additional events in our case but also discarded two events considered in Khan et al. (2021), as

Figure 15. Posterior distributions for models with acceptable misfit values (corresponding to the best 10,000 models) from geodynamically constrained inversions without (left) or with (right) constraints on the crustal thickness displayed in Figure 14. (a–h) Present-day quantities: (a and b) average surface heat flow, (c and d) average temperature gradient in the lithosphere (excluding the crust), (e and f) mantle potential temperature, (g and h) areotherms for the best 1,000 models, (i–j) crustal enrichment factor, (k–l) initial uppermost mantle temperature T_{m0}. Blue colors indicate output present-day quantities, while black colors refer to input global or initial quantities from the geodynamic forward problem.

explained in Section 3.3. The differences can also be attributed in part to the parameterization of the forward problem. For example, Khan et al. (2021) allows for enriched HPE contents compared to the fixed bulk HPE content we considered (Section 4.1.2). Higher bulk HPE contents can lead to a hotter thermal evolution and an enhanced crustal production that would be compensated for instance by larger crustal enrichment values, and vice versa (e.g., Knapmeyer-Endrun et al., 2021). In addition, in Khan et al. (2021) the interpretation of the seismic data inversion in terms of mantle structure and thermal history is performed as a second, "post-processing" step, while along the inversion procedure the lithosphere geotherm is considered to be linear throughout the entire lithosphere, and did not consider a change in thermal gradient in the uppermost mantle thermal boundary layer. These simplifications can have a limited, yet appreciable, impact on the seismic structure, in particular toward the base of the lithosphere. In contrast, here we do not assume that the lithospheric geotherm is linear and explicitly consider a change in thermal gradient corresponding to the presence of the upper thermal boundary layer at the base of the lithosphere. Furthermore, the thermal history of Mars is directly embedded in the forward problem and in the inversion loop instead of being treated as a post-processing stage. This implies that our inversion approaches samples a different model space than the one sampled in Khan et al. (2021). Finally, in Khan et al. (2021) the crustal constraints considered are considerably more restrictive because the favored models consist of cases with average crustal thickness smaller than 55 km. Here, we consider instead a broader range with $D_{cr} = 52.5 \pm 10$ km (Section 5.4). This range is compatible with $D_{cr} = 39$–72 km proposed in Knapmeyer-Endrun et al. (2021). Given these differences in data set and parameterization, one can reasonably consider that our inversion results are compatible with recent works. This underlines the fact that inversion results need to be considered with a good awareness of the assumptions associated with the inversion approaches.

6. Discussion

Our results show how the marsquake locations and the 1-D structure of Mars can be investigated using a limited seismic data set and a single station. In this section, the implications of the marsquake locations on the tectonic activity around InSight are first analyzed. Then, we discuss the stratification of the crust.

6.1. Implications of the Marsquake Locations on the Tectonic Activity Around InSight

Most of the Martian volcanic and tectonic activities occurred more than 3 Ga ago and are supposed to have faded out since then, as the heat flow decreased through time (e.g., Carr & Head, 2010). Thus, before the first record of a marsquake by the InSight mission, it was rather expected that the current Martian seismic activity with a tectonic origin would be scattered, generated by contractional features (i.e., wrinkle ridges, lobate scarps; see black lines in Figure 6) related to the global cooling of the planet and local regional stresses resulting from subsidence (e.g., Watters, 1993). Among the large number of events (>1,000) detected by InSight (InSight Marsquake Service, 2021), it is possible that part of the seismicity is located along these contractional features (see white shaded areas in Figure 6 and Giardini et al. (2020)).

Still, the first striking observation of the global topographic map shown in Figure 6 is that, given the fairly large uncertainties in back azimuths, all larger events but five (i.e., S0185a, S0325a, S0474a, S0861a, and S0918a) are located East of the InSight lander, in the close vicinity of Cerberus Fossae and Grjótá Valles. This region was already highlighted in Giardini et al. (2020) that first located the S0173a and S0235b events, which are also in good agreement with the locations obtained in our study. Moreover, the hypocentral depths of the events are fairly shallow (i.e., <40 km; Table 3). This suggests a crustal origin with possible links to the different tectonic morphologies observed at the surface (Perrin et al., 2022).

The Cerberus Fossae and Grjótá Valles are major fracture zones that are cross-cutting one of the youngest volcanic terrains on Mars (Tanaka et al., 1992). Prior to the InSight mission, studies inferred that recent tectonic and volcanic activities (i.e., younger than 10 Ma; Vaucher et al., 2009) occurred in the Cerberus Fossae region, which might be the source of marsquakes of moderate size (J. Taylor et al., 2013). The fact that major events are located close to these extensional structures raises the question of the current active tectonic origin on Mars. One could assume that the global cooling would reactivate weak crustal fracture zones inherited from a past geodynamical history. However, it seems that the recent S0173a and S0235b events display instead extensional strains (Brinkman et al., 2021), in good agreement with Cerberus Fossae's strike and

dip. The evidence for a very recent volcanic activity on Cerberus Fossae (<250 ka; Horvath et al., 2021) and the possibility that some seismic signals could be associated with volcanic tremors (Kedar et al., 2021) would favor the hypothesis of small remnants of volcanic and extensional tectonic activities in the Elysium Planitia region.

Nevertheless a question remains: if the volcano-tectonic activity on Cerberus Fossae (and maybe on Grjótá Valles) is still active, why are they the only young structures to generate magnitude ∼3 marsquakes detected by InSight after 2 years of seismic recording on Mars? The radial geometry of the fossae related to Elysium Mons would suggest a genetic link between the volcano and the fracture networks (e.g., Ernst et al., 2002). If this is the case, one would also expect additional seismic activity coming from Elysium Mons and associated with young graben structures such as Elysium Fossae. Despite its large location uncertainty, the event S0474a might be linked to such activity. Also, it could be included in the smaller magnitude seismicity for which back-azimuths were not possible to determine (i.e., white shaded area between 22° and 30° of epicentral distance; Figure 6 and Giardini et al. (2020)). Otherwise, it would be necessary to involve another mechanism responsible for stress concentrations along Cerberus Fossae and Grjótá Valles, such as the one proposed by Hall et al. (1986), who showed that the global stress field induced by the Tharsis rise could create extensional strains responsible for the formation of Cerberus Fossae.

Finally, four events stand out from the others because of their locations: S0325a and S0918a are located SE of InSight, at the Martian dichotomy, while S0185a and S0861a are located NW of InSight in Utopia Planitia, just north of the dichotomy and Isidis basin (Figure 6). The large uncertainties on their locations allow us to make different hypotheses regarding their origins (note that the back azimuth uncertainty of S0918a is too large to propose a limited number of scenarios). Event S0325a is located close to a major extensional feature: Al Qahira Vallis, which corresponds to a SSW-NNE graben associated with a channel outflow at the dichotomy. The northern and southern vertices of the ellipse cover respectively Apollinaris Mons (estimated age of activity ranging from Lower Hesperian to Lower Amazonian; Robinson et al., 1993) and possible recent fossae (Knapmeyer et al., 2006) linked to the tip of large fracture networks that developed from Tharsis and cross-cutting old highlands terrains (i.e., Memnomia and Sirenum Fossae). Events S0185a and S0861a are located far from major tectonic features. The global fault map shows the presence of few compressional features sub-parallel to the dichotomy (Figure 6). We also note the proximity of the large Nili Fossae to the south, at the edge of the Isidis basin formed by an impact more than 3 Ga ago (Greeley & Guest, 1987), which could present surface instabilities leading to large landslides or rockfalls. However, additional information is required to discuss the details on the origin of these marsquakes, such as the determination of their focal mechanisms.

6.2. Stratification in the Crust

As expected from Martian petrology (McSween, 2015), the crust of Mars appears stratified with an upper crust marked by lower seismic velocities, and a dominant lower crust characterized by large seismic velocities (Table 4). The overall regional structure deduced from seismic inversions appears consistent with the local structure derived from Receiver Function analysis below the InSight station (Knapmeyer-Endrun et al., 2021).

The upper crust may be formed by two different layers. The upper layer shows very low seismic velocities (Table 4), consistent with unconsolidated, highly fractured material. Both the average thickness and seismic velocities are consistent with previous findings from Receiver Function analysis (Knapmeyer-Endrun et al., 2021; Lognonné et al., 2020). However, a model with only two layers in the crust equally fits the data if this upper low-velocity layer is not present, as shown in Appendix G (Figures G1 and G2). Hence, we cannot conclude if this unconsolidated layer is present regionally or only locally. The mid layer, with an estimated thickness of 16.7 ± 17.8 to 32.8 ± 15.0 km depending on the inversion type, shows seismic velocities consistent with those of basalts (Christensen & Mooney, 1995) (Table 4). The lower crust makes a significant fraction of the crust with an average thickness of 50.6 ± 20.5 km for the classical inversion and 52.6 ± 10.8 km for the geodynamically constrained one. Its seismic wave speeds (Table 4) are consistent with that of intrusive mafic to ultramafic rocks and cumulates. The low V_P/V_S ratio excludes compositions such as anorthosites and serpentinites (Christensen, 1995). Seismic velocities in this layer are consistent with a gabbro lithology, although the S-wave velocity falls in the upper range of that characteristic of gabbros and the V_P/V_S ratio is consequently rather low (Christensen & Mooney, 1995).

Thus, as for the oceanic and continental crusts on Earth, the Martian crust seems to exhibit a lower crust of significant thickness composed of denser intrusive mafic rocks (Condie, 2016). This is not a surprise: on Earth, the volume of intrusive rocks is on average five to 10 times larger than the volume of extrusive ones in oceanic and continental settings, respectively (Crisp, 1984). Furthermore, samples of intrusive and cumulate Martian rocks are available among SNC meteorites (Sautter & Payré, 2021). Two gabbroic shergottites have for instance been identified: Northwest Africa (NWA) 7320 (Udry et al., 2017), as well as NWA 6963, that is interpreted as a pyroxene-cumulate gabbro (Filiberto et al., 2014, 2018).

Our results point to a large jump in velocity in between the mid layer (or the upper one if the crust has only two layers) and the lower one, potentially corresponding to the limit between intrusive crystalline rocks and extrusive rocks. The last interface would correspond to the petrological Moho, that is, a difference in petrology between the lower crust and mantle, by opposition to the "seismic Moho" which may refer to a large impedance contrast. This last interface seems associated with a smaller velocity increase than the shallower one, probably because of the mafic to ultramafic and/or cumulate nature of the lower Martian crust. Since seismic velocities tend to increase with the density of crustal material, this could also suggest that the Martian crust is stratified in density with a lower crust denser than the upper one.

From the thickness ratio of the lower to upper crust, and depending on the inversion details (two or three layers in the crust, geodynamic or classical parameterizations), we can estimate an intrusive to extrusive ratio between 4.6 ± 5.0 and 1.5 ± 0.8 (Tables 4 and G1) assuming that the second interface indeed corresponds to the transition between intrusive crystalline rocks and extrusive ones. This ratio appears similar to that of the basaltic oceanic crust and much smaller than that of the continental crust (Crisp, 1984).

7. Conclusion

The uneven and sparse seismic data that results from InSight's single-station/multiple events setup requires inversion approaches specifically designed to best exploit this configuration. In this framework, we used the method developed in Drilleau et al. (2020, 2021) to constrain the quake locations and the 1-D average seismic velocity profiles of Mars, considering a new and augmented data set of direct body waves phases (P and S), surface reflected phases (PP, PPP, SS, and SSS), depth phases (pP, sS, and sP), and core-reflected S-waves (ScS). To the best of our knowledge, this is currently the largest seismic data set so far considered for the inversion of the Martian structure. Two distinct approaches were considered. One approach relying on a classic Bézier curves parameterization of the 1-D seismic velocity profiles. The second approach relied on a parameterization that incorporates the long-term thermochemical evolution of the planet, allowing to increase the prior knowledge on the model parameters.

We identified and localized seventeen low-frequency marsquakes (depth, epicentral distance, and back azimuth), which adds fifteen new marsquakes to the list of the two already localized in Brinkman et al. (2021) and in Clinton et al. (2021). Our results indicate that the hypocenters are relatively shallow, located above 40 km depth. Most of the events are located between 25° and 30° epicentral distance, in the close vicinity to major extensional fracture zones, Cerberus and Grjótá Valles, which could be considered as the main source of marsquakes. These results raise the question of the current active tectonic origin on Mars, in particular if it could be linked to either a volcanic activity from Elysium Mons or/and to the load of the Tharsis rise. The three most distant marsquakes are located southeast of InSight, in close vicinity to the Martian dichotomy, and northwest of InSight in Utopia Planitia. Given the large uncertainties on their back azimuths, additional work remains needed to understand the origin of these marsquakes, in particular their focal mechanisms. Yet, our results represent a first step toward a better understanding of the location of the seismicity on Mars.

Overall, the arrival time data set we extracted out of the seismic record, combined with geodynamic and other associated considerations yields relatively tight constraints on the present-day structure of Mars, on the rheology of its mantle (except for its pressure-dependence that remains too exposed to tradeoffs between temperature and viscosity), and on its thermo-chemical history. Our most constrained inversion results indicate a present-day surface heat flux of 22 ± 1 mW/m², a relatively hot mantle (potential temperature: 1740 ± 90 K) and thick lithosphere (540 ± 120 km), associated with a lithospheric thermal gradient of 1.9 ± 0.3 K/km. These ranges are associated with a relatively sluggish mantle ($\eta_0 = 10^{21.9 \pm 0.4}$ Pa s). These results are compatible with recent seismic studies (Khan et al., 2021; Knapmeyer-Endrun et al., 2021) using a distinct and smaller data set and a different

type of inversions of the shallow structure with less informative prior also confirm that Mars' mantle was initially relatively cold (with an uppermost mantle temperature 1780 ± 50 K), and that its crust contains 10–12 times more HPEs than the primitive mantle.

Our inversion results show that the crust of Mars may be formed by one or two layers, for which the retrieved seismic velocities are consistent with unconsolidated, highly fractured materials. As for oceanic and continental crusts on Earth, the Martian crust appears to exhibit a lower crust of significant thickness, with a composition compatible with that of denser mafic to ultramafic rocks, which is consistent with the analysis of Martian meteorites. Our results show a significant velocity jump between the upper and the lower parts of the crust that we identify as the limit between intrusive and extrusive rocks. We consider the last interface to be the petrological Moho. The velocity jump at this interface is smaller than the one located between the intrusive and extrusive rocks, probably due to the nature of the mafic to ultramafic rocks present in the lower crust. The uncertainty on the Moho depth remains large when inverting differential arrival times of body waves, due to trade-offs between the seismic velocities and the depth of the interfaces. The addition of independent constraints on the crustal thickness from analyzes of seismic phases that are reflected and converted at interfaces (Knapmeyer-Endrun et al., 2021), combined with modeling from gravity and topography measurements, decrease the trade-offs between the governing parameters. Our results raise the question of whether this lower crust, with seismic velocities close to those of the underlying mantle, is present at the global scale on Mars. If it is the case, it could have important consequences on the interpretation of the global crustal thickness maps obtained from modeling of gravity and topography measurements, for which the density is considered to be homogeneous in the entire crust (Wieczorek et al., 2019).

The InSight mission has been extended until the end of 2022. This additional time window could yield the detection and the identification of marsquakes located at different epicentral distances, in particular at larger distances, which could allow for a continuous refinement of the distribution of the model parameters, eventually leading to better constraints on the structure of the deeper parts of mantle.

Appendix A: Back-Azimuth Estimates for All Quakes

This section is providing the figures allowing to estimate all the back azimuths of the quakes listed in Table 1. The figure panels are identical to the ones of Figure 2.
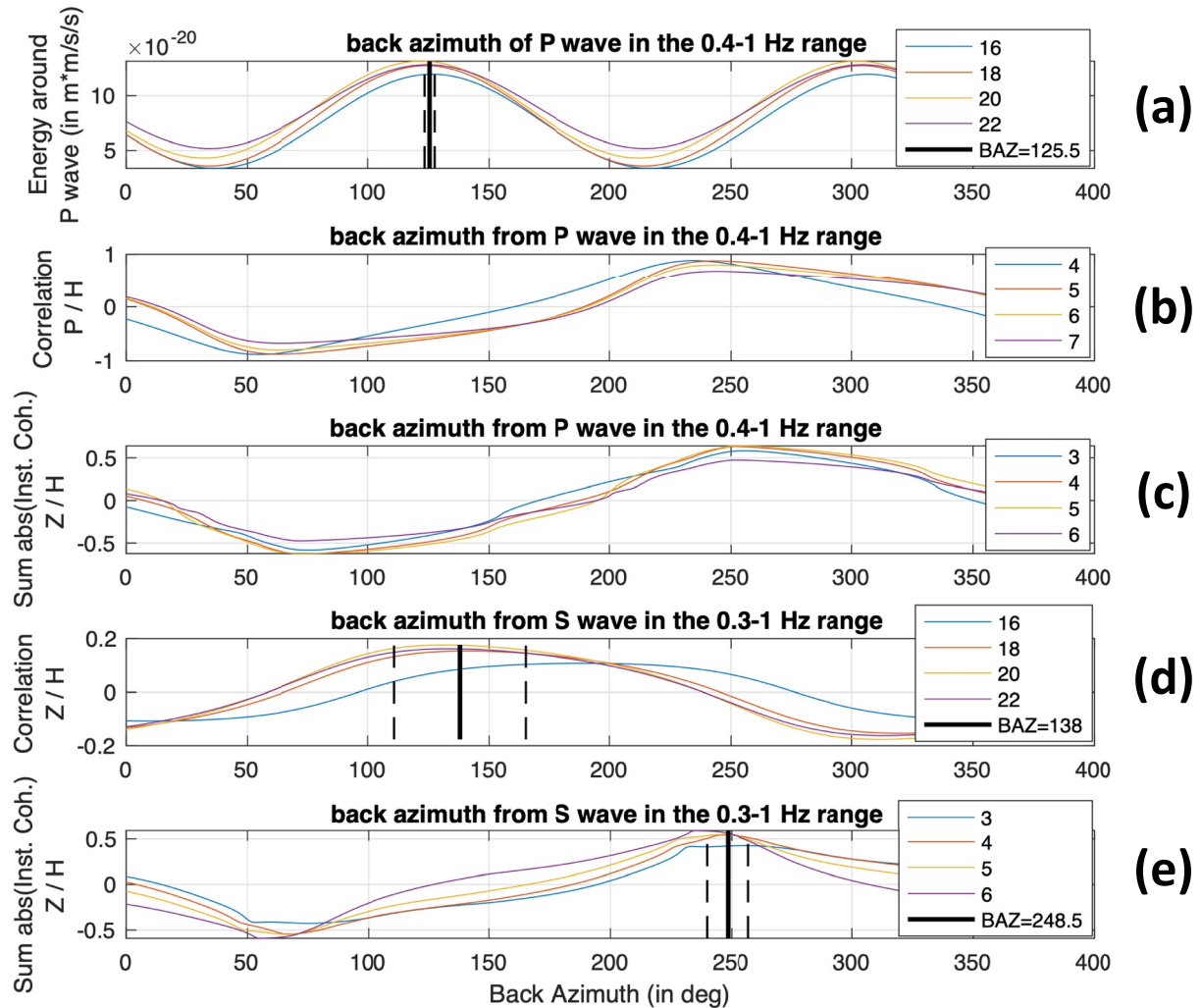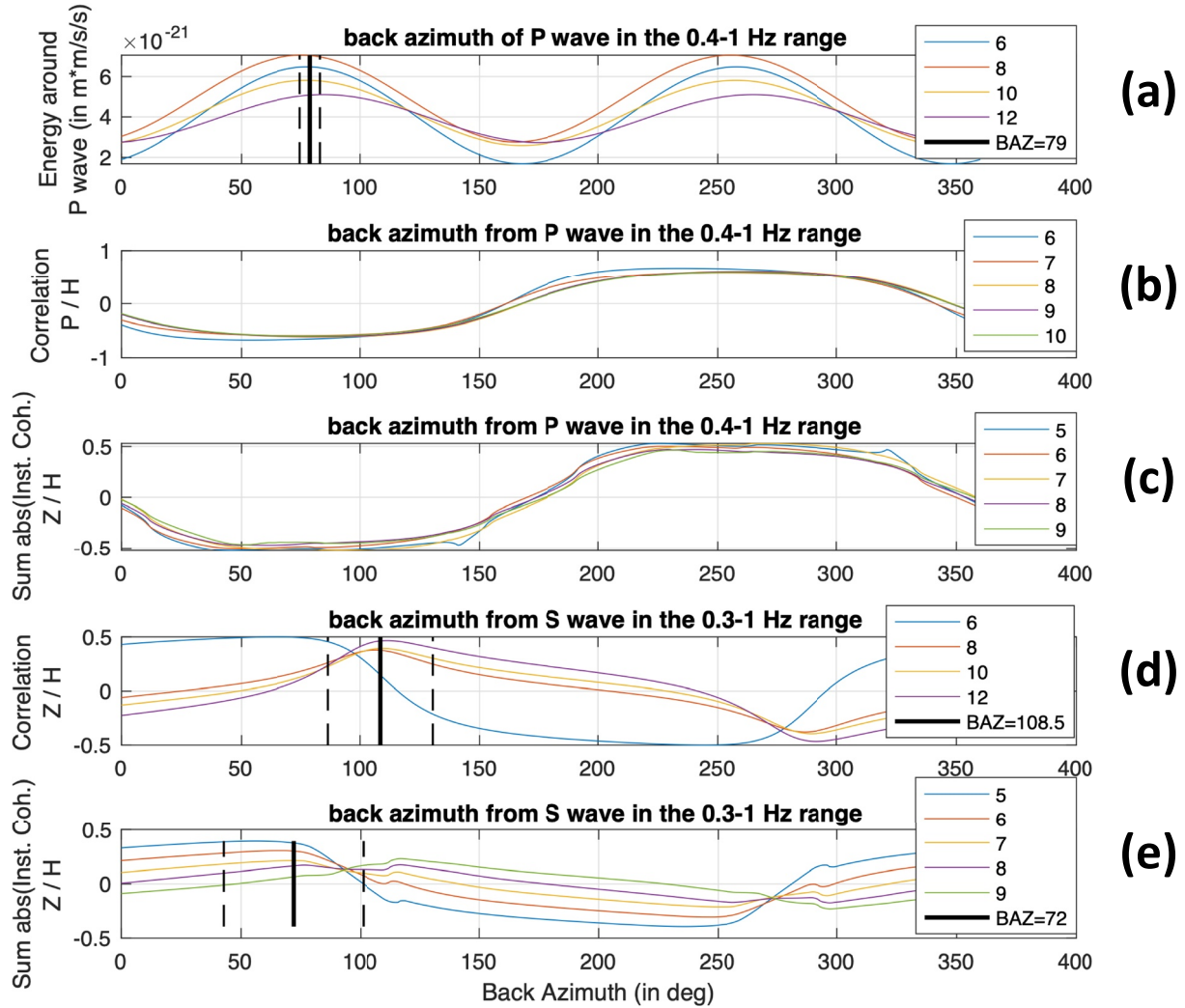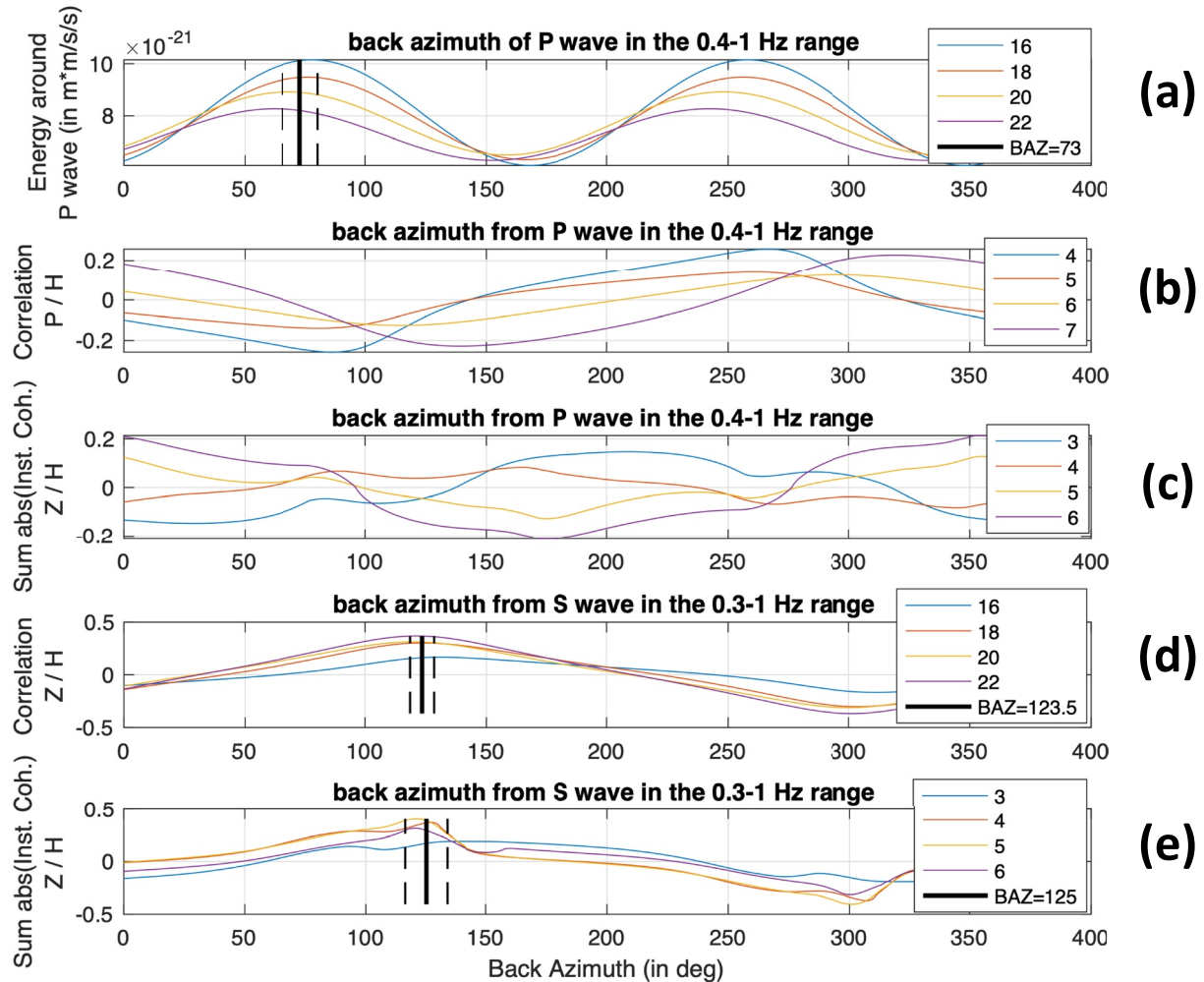
Figure A1
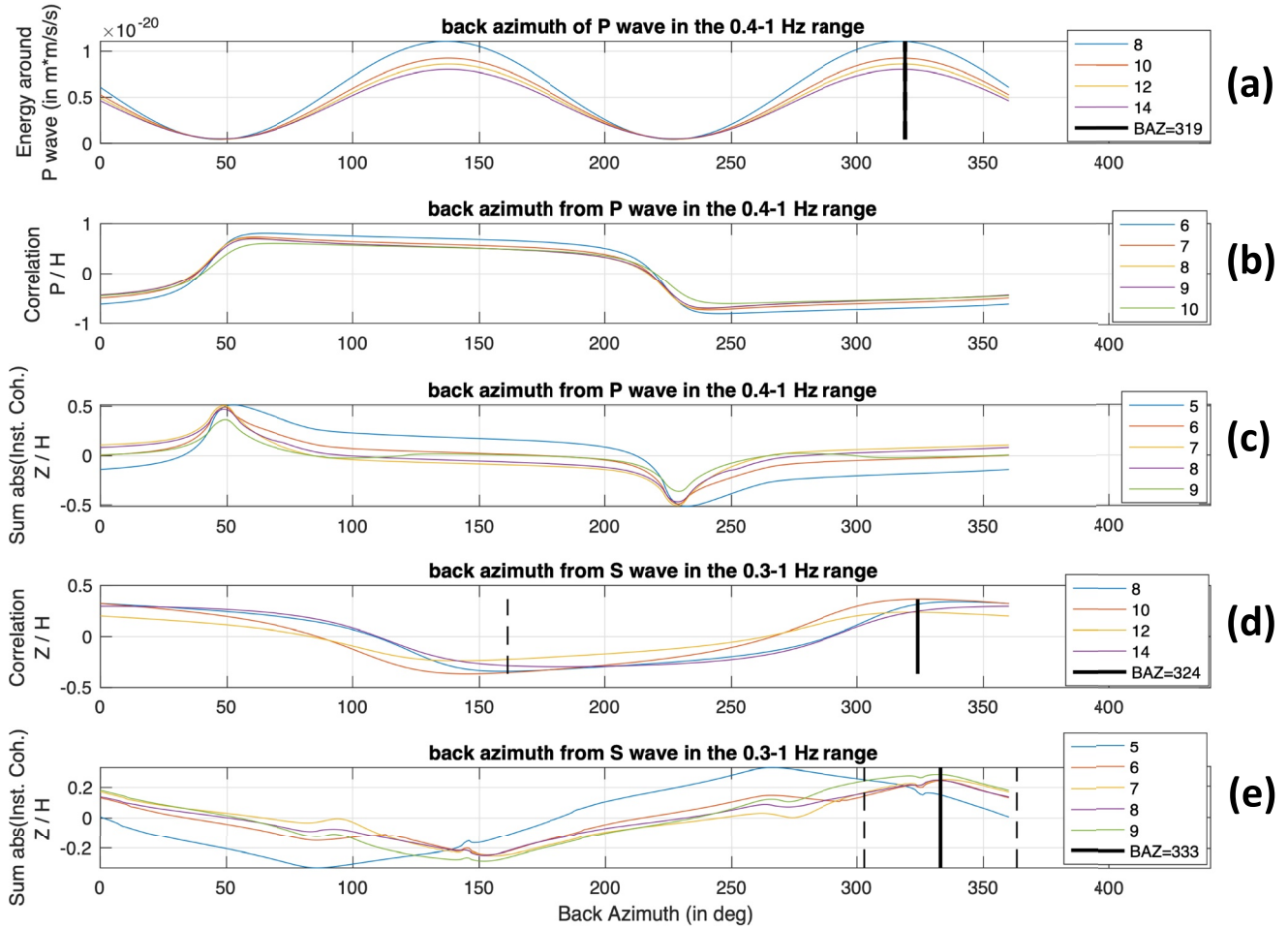
Figure A1. Back azimuth determination for event S0185a. From top to bottom: energy along the horizontal component around the P wave arrival, correlation coefficient between vertical and horizontal components around the P wave, average of instantaneous phase coherence between vertical and horizontal components around the P wave, correlation coefficient between vertical and horizontal components around the S wave, average of instantaneous phase coherence between vertical and horizontal components around the S wave. For each panel, all possible back azimuths are examined and various window length (in s) are tested (different colors). Best estimates of back azimuth are identified by vertical black lines. The standard deviation of the best back azimuths, among all the window sizes tested, are indicated by black dashed vertical lines. The error on the back azimuth estimate is computed by averaging this standard deviation and the average width of the correlation function at 80% of its peak value.
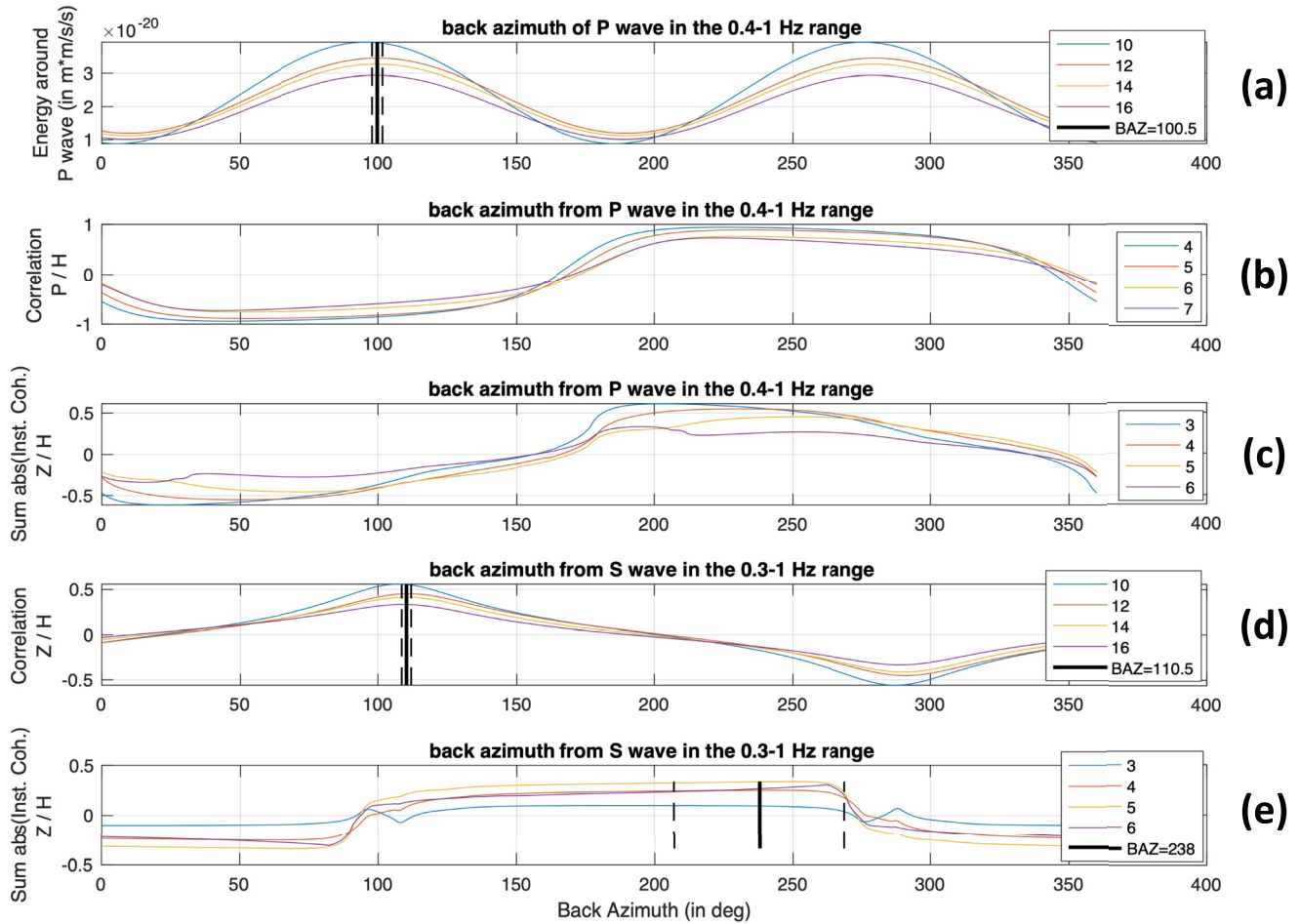
Figure A2
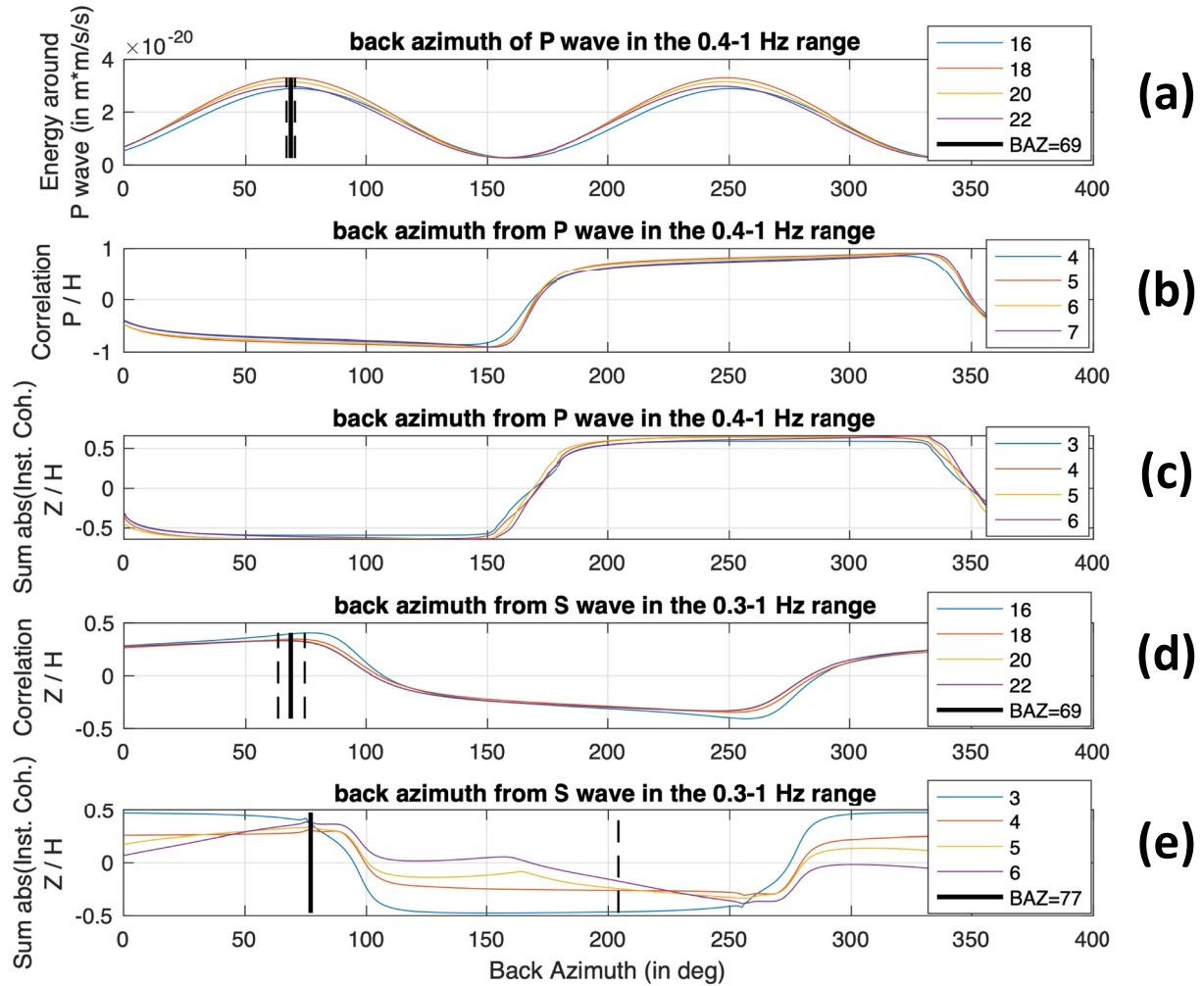
Figure A2. Back azimuth determination for event S0235b. From top to bottom: energy along the horizontal component around the P wave arrival, correlation coefficient between vertical and horizontal components around the P wave, average of instantaneous phase coherence between vertical and horizontal components around the P wave, correlation coefficient between vertical and horizontal components around the S wave, average of instantaneous phase coherence between vertical and horizontal components around the S wave. For each panel, all possible back azimuths are examined and various window length (in s) are tested (different colors). Best estimates of back azimuth are identified by vertical black lines. The error on the back azimuth estimate is computed by averaging this standard deviation and the average width of the correlation function at 80% of its peak value.
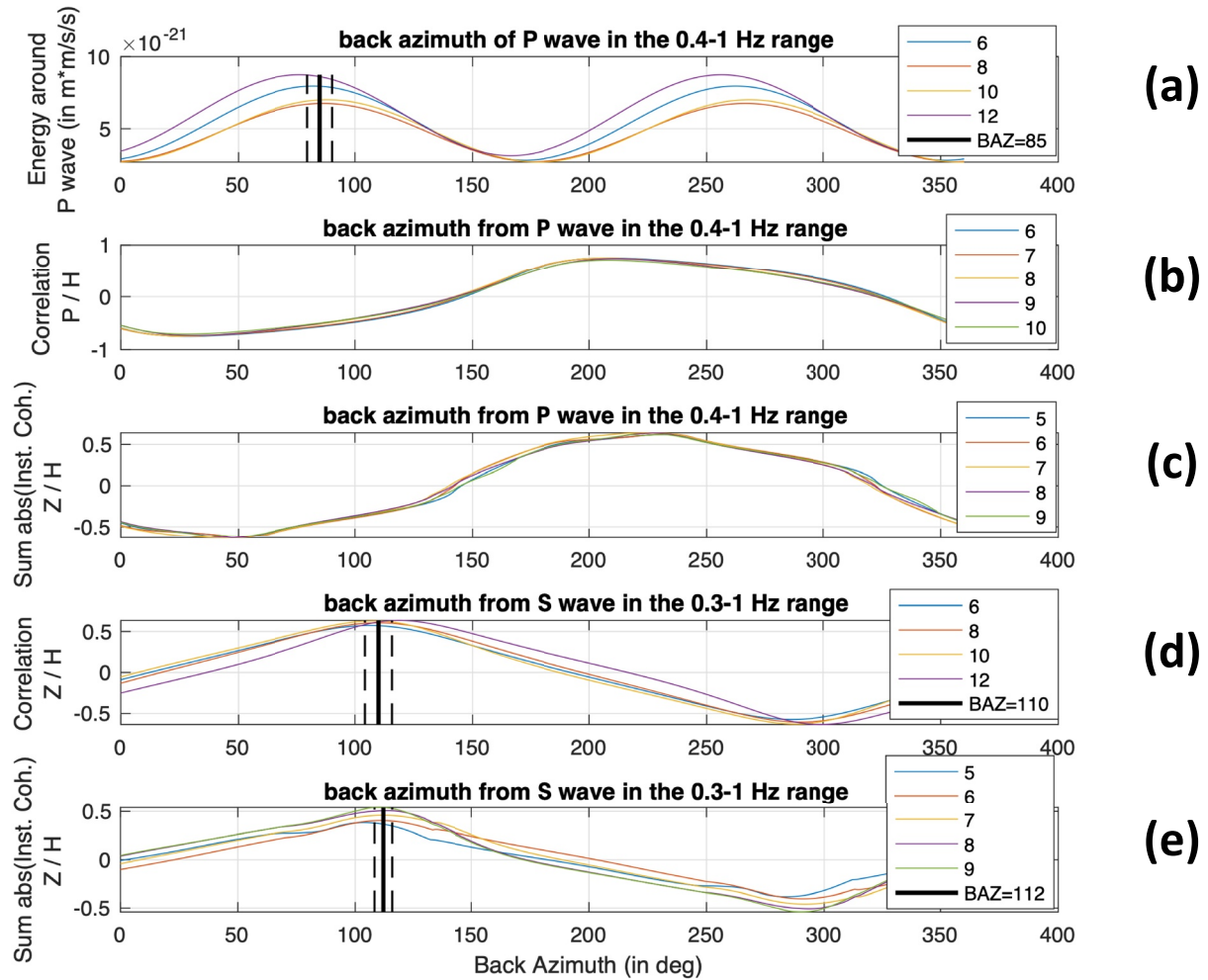
Figure A3

Figure A3. Back azimuth determination for event S0325a. From top to bottom: energy along the horizontal component around the P wave arrival, correlation coefficient between vertical and horizontal components around the P wave, average of instantaneous phase coherence between vertical and horizontal components around the P wave, correlation coefficient between vertical and horizontal components around the S wave, average of instantaneous phase coherence between vertical and horizontal components around the S wave. For each panel, all possible back azimuths are examined and various window length (in s) are tested (different colors). Best estimates of back azimuth are identified by vertical black lines. The error on the back azimuth estimate is computed by averaging this standard deviation and the average width of the correlation function at 80% of its peak value.
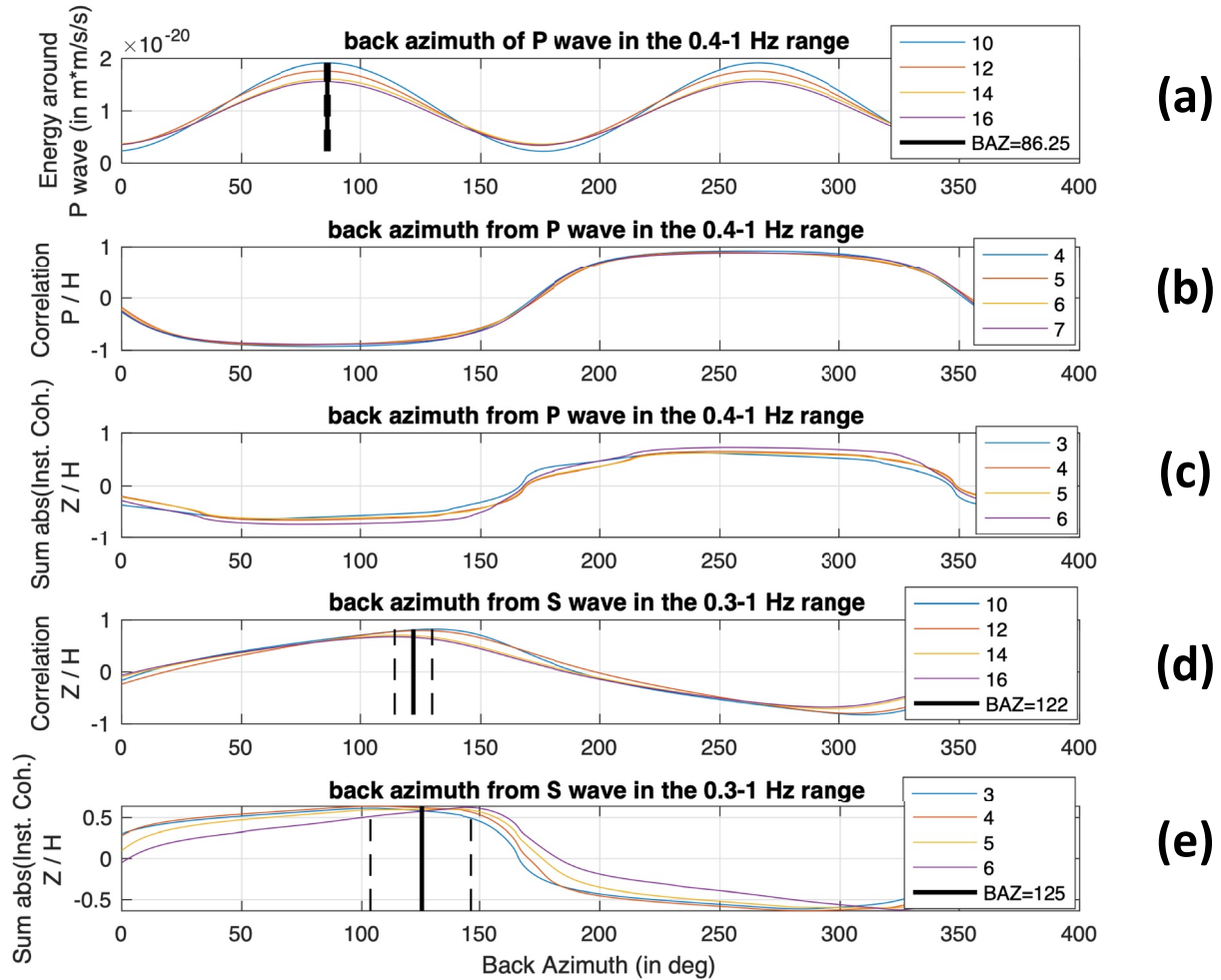
Figure A4

Figure A4. Back azimuth determination for event S0407a. From top to bottom: energy along the horizontal component around the P wave arrival, correlation coefficient between vertical and horizontal components around the P wave, average of instantaneous phase coherence between vertical and horizontal components around the P wave, correlation coefficient between vertical and horizontal components around the S wave, average of instantaneous phase coherence between vertical and horizontal components around the S wave. For each panel, all possible back azimuths are examined and various window length (in s) are tested (different colors). Best estimates of back azimuth are identified by vertical black lines. The error on the back azimuth estimate is computed by averaging this standard deviation and the average width of the correlation function at 80% of its peak value.

Figure A5

Figure A5. Back azimuth determination for event S0484b. From top to bottom: energy along the horizontal component around the P wave arrival, correlation coefficient between vertical and horizontal components around the P wave, average of instantaneous phase coherence between vertical and horizontal components around the P wave, correlation coefficient between vertical and horizontal components around the S wave, average of instantaneous phase coherence between vertical and horizontal components around the S wave. For each panel, all possible back azimuths are examined and various window length (in s) are tested (different colors). Best estimates of back azimuth are identified by vertical black lines. The error on the back azimuth estimate is computed by averaging this standard deviation and the average width of the correlation function at 80% of its peak value.
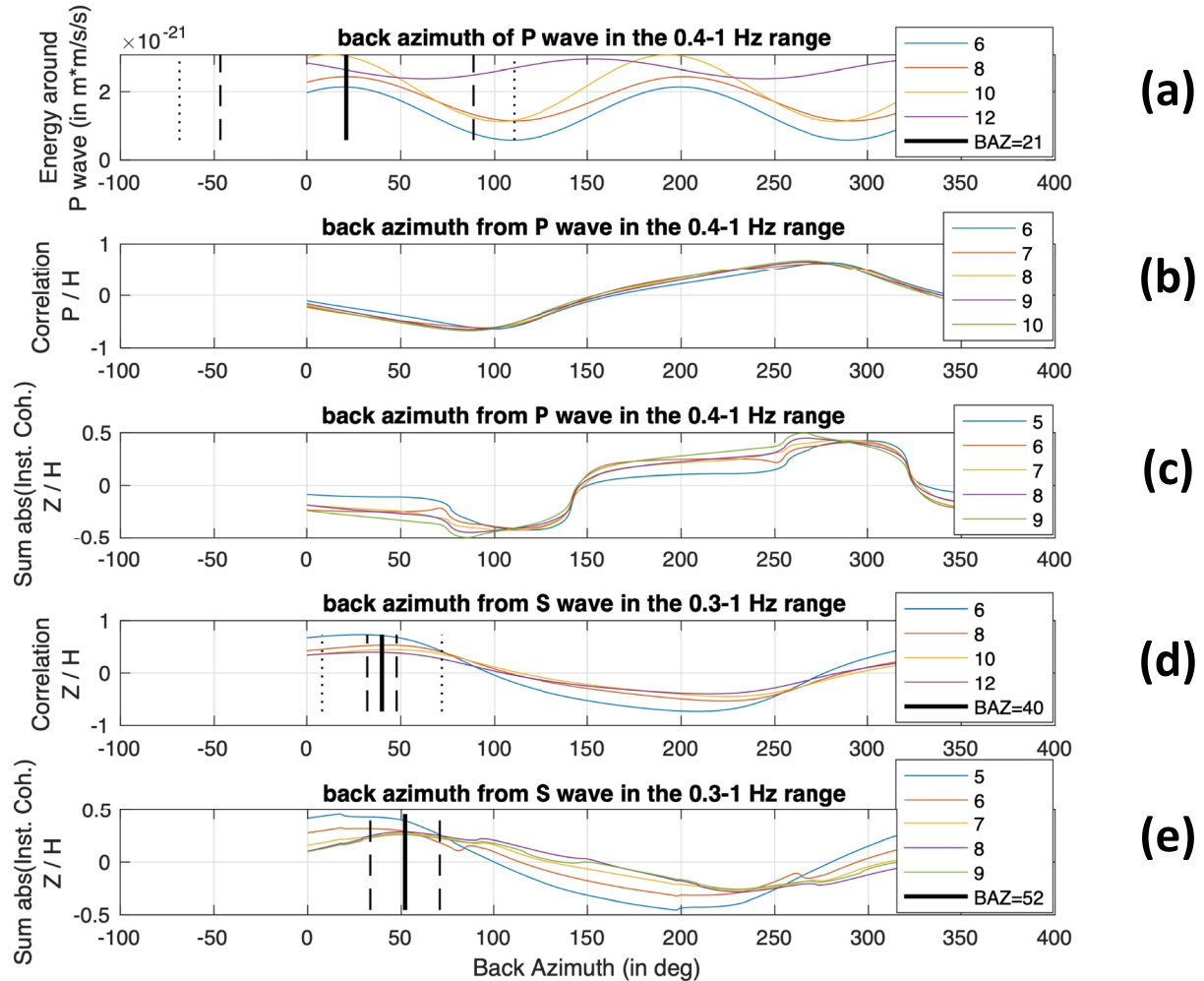
Figure A6

Figure A6. Back azimuth determination for event S0784a. From top to bottom: energy along the horizontal component around the P wave arrival, correlation coefficient between vertical and horizontal components around the P wave, average of instantaneous phase coherence between vertical and horizontal components around the P wave, correlation coefficient between vertical and horizontal components around the S wave, average of instantaneous phase coherence between vertical and horizontal components around the S wave. For each panel, all possible back azimuths are examined and various window length (in s) are tested (different colors). Best estimates of back azimuth are identified by vertical black lines. The error on the back azimuth estimate is computed by averaging this standard deviation and the average width of the correlation function at 80% of its peak value.
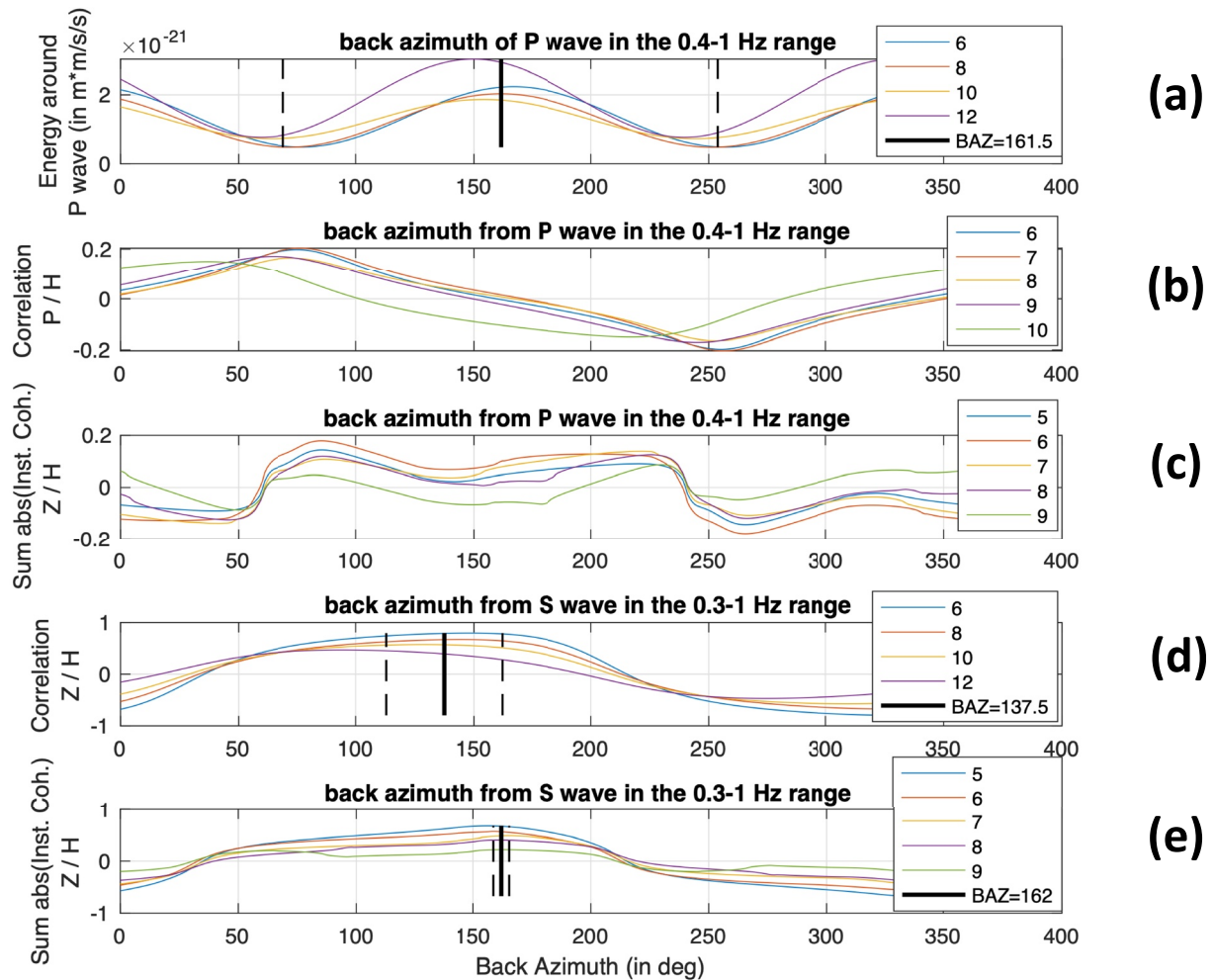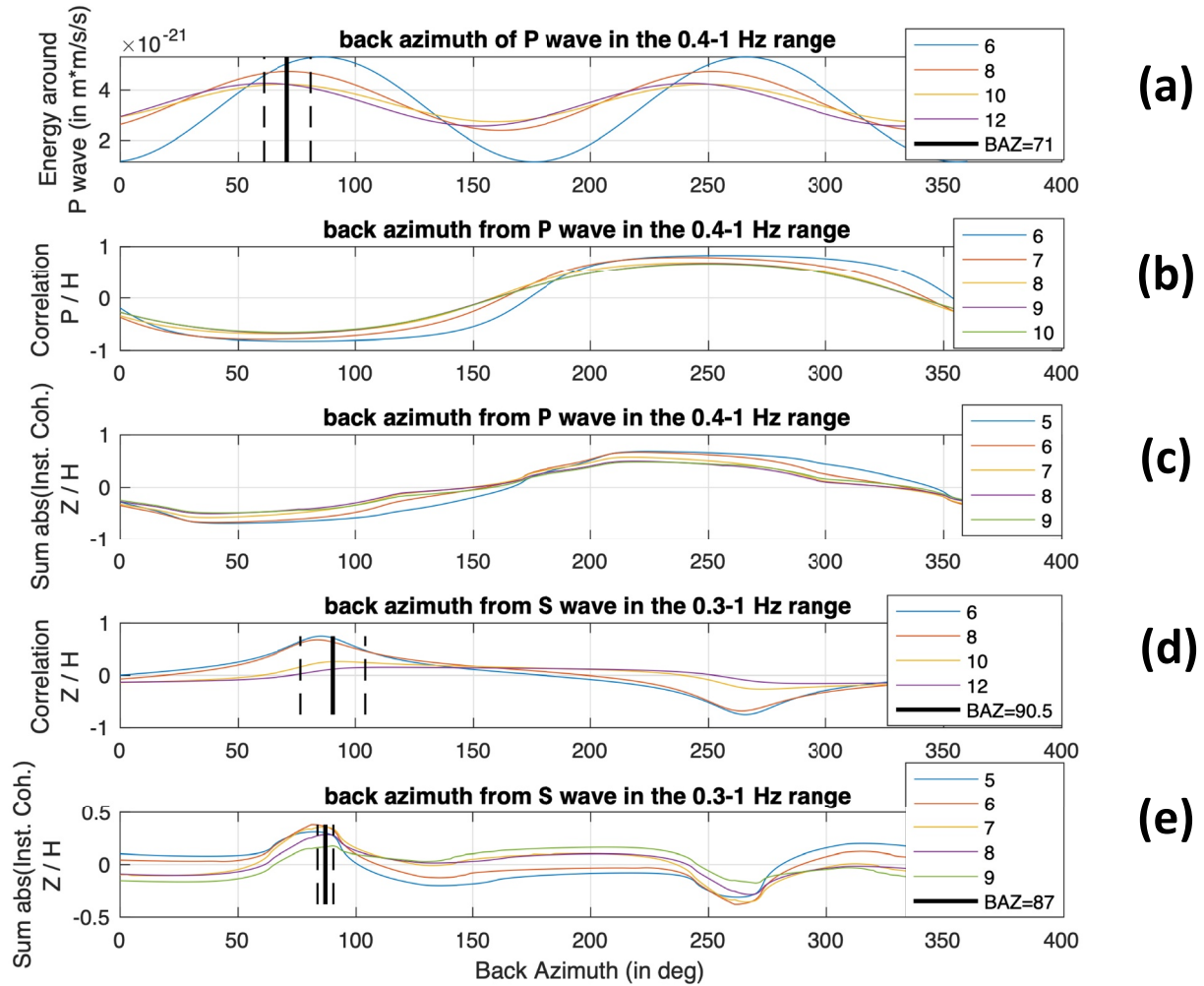
Figure A7

Figure A7. Back azimuth determination for event S0802a. From top to bottom: energy along the horizontal component around the P wave arrival, correlation coefficient between vertical and horizontal components around the P wave, average of instantaneous phase coherence between vertical and horizontal components around the P wave, correlation coefficient between vertical and horizontal components around the S wave, average of instantaneous phase coherence between vertical and horizontal components around the S wave. For each panel, all possible back azimuths are examined and various window length (in s) are tested (different colors). Best estimates of back azimuth are identified by vertical black lines. The error on the back azimuth estimate is computed by averaging this standard deviation and the average width of the correlation function at 80% of its peak value.
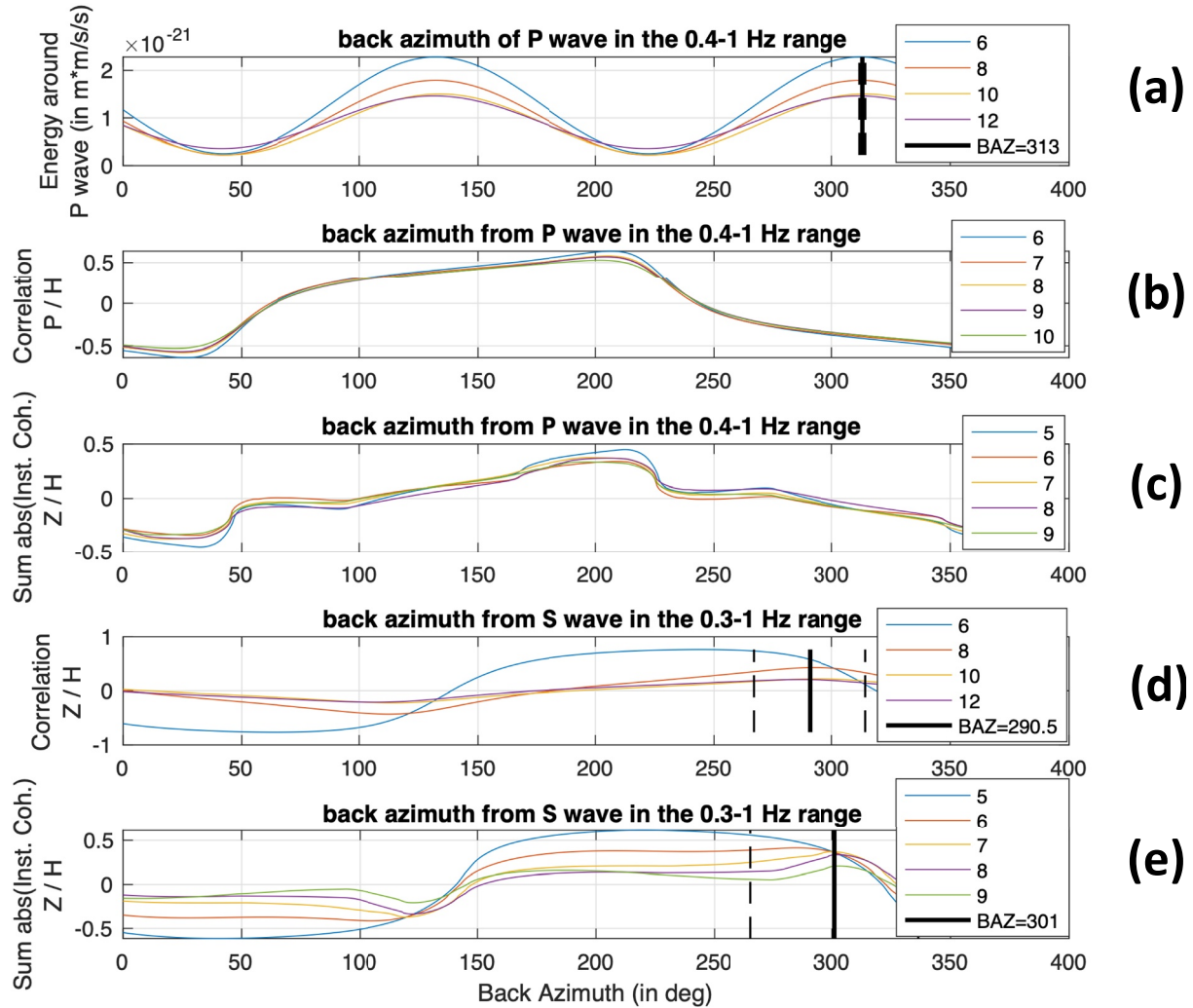
Figure A8

Figure A8. Back azimuth determination for event S0809a. From top to bottom: energy along the horizontal component around the P wave arrival, correlation coefficient between vertical and horizontal components around the P wave, average of instantaneous phase coherence between vertical and horizontal components around the P wave, correlation coefficient between vertical and horizontal components around the S wave, average of instantaneous phase coherence between vertical and horizontal components around the S wave. For each panel, all possible back azimuths are examined and various window length (in s) are tested (different colors). Best estimates of back azimuth are identified by vertical black lines. The error on the back azimuth estimate is computed by averaging this standard deviation and the average width of the correlation function at 80% of its peak value.
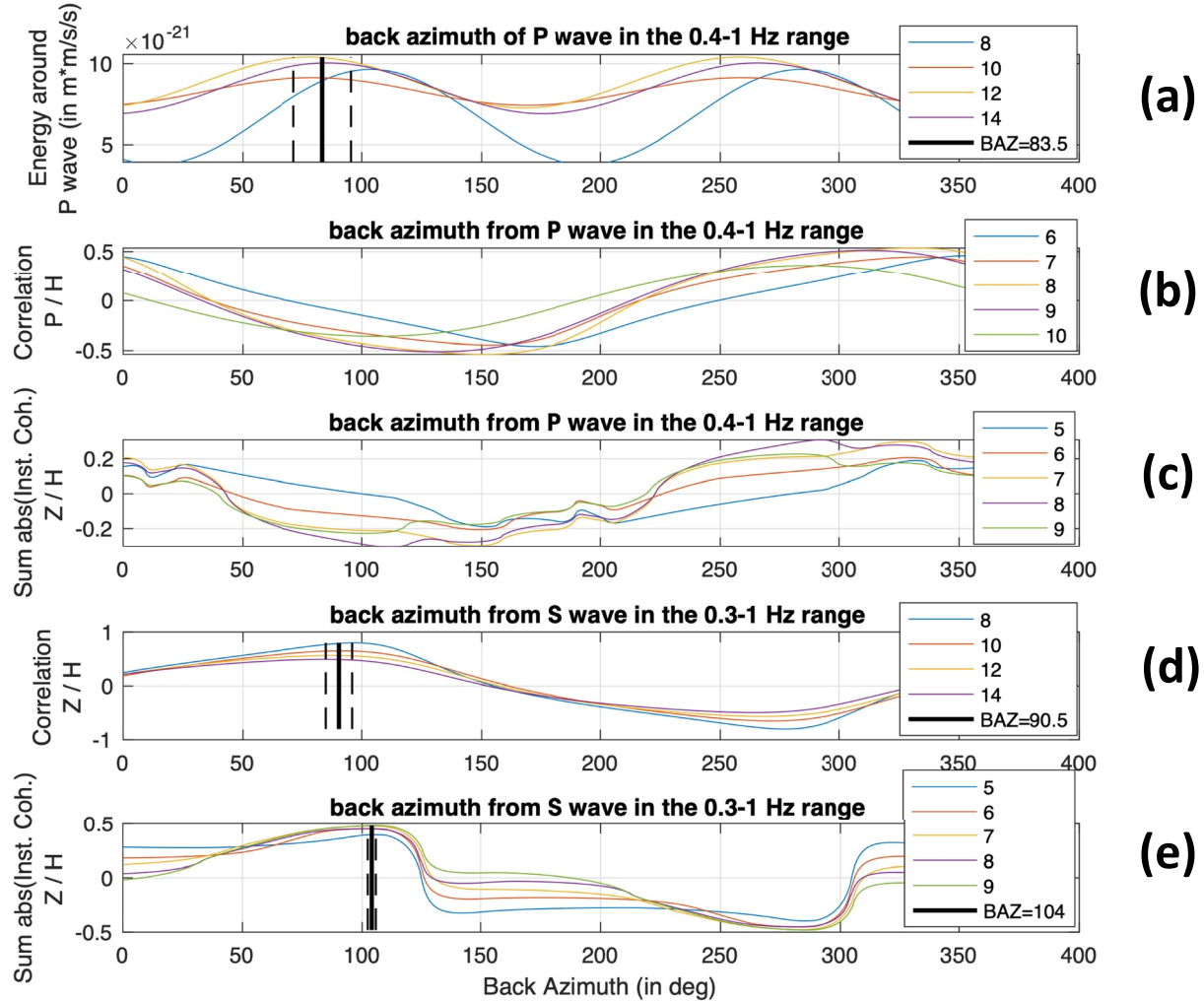
Figure A9

Figure A9. Back azimuth determination for event S0474a. From top to bottom: energy along the horizontal component around the P wave arrival, correlation coefficient between vertical and horizontal components around the P wave, average of instantaneous phase coherence between vertical and horizontal components around the P wave, correlation coefficient between vertical and horizontal components around the S wave, average of instantaneous phase coherence between vertical and horizontal components around the S wave. For each panel, all possible back azimuths are examined and various window length (in s) are tested (different colors). Best estimates of back azimuth are identified by vertical black lines. The error on the back azimuth estimate is computed by averaging this standard deviation and the average width of the correlation function at 80% of its peak value.

Figure A10

Figure A10. Back azimuth determination for event S0918a. From top to bottom: energy along the horizontal component around the P wave arrival, correlation coefficient between vertical and horizontal components around the P wave, average of instantaneous phase coherence between vertical and horizontal components around the P wave, correlation coefficient between vertical and horizontal components around the S wave, average of instantaneous phase coherence between vertical and horizontal components around the S wave. For each panel, all possible back azimuths are examined and various window length (in s) are tested (different colors). Best estimates of back azimuth are identified by vertical black lines. The error on the back azimuth estimate is computed by averaging this standard deviation and the average width of the correlation function at 80% of its peak value.
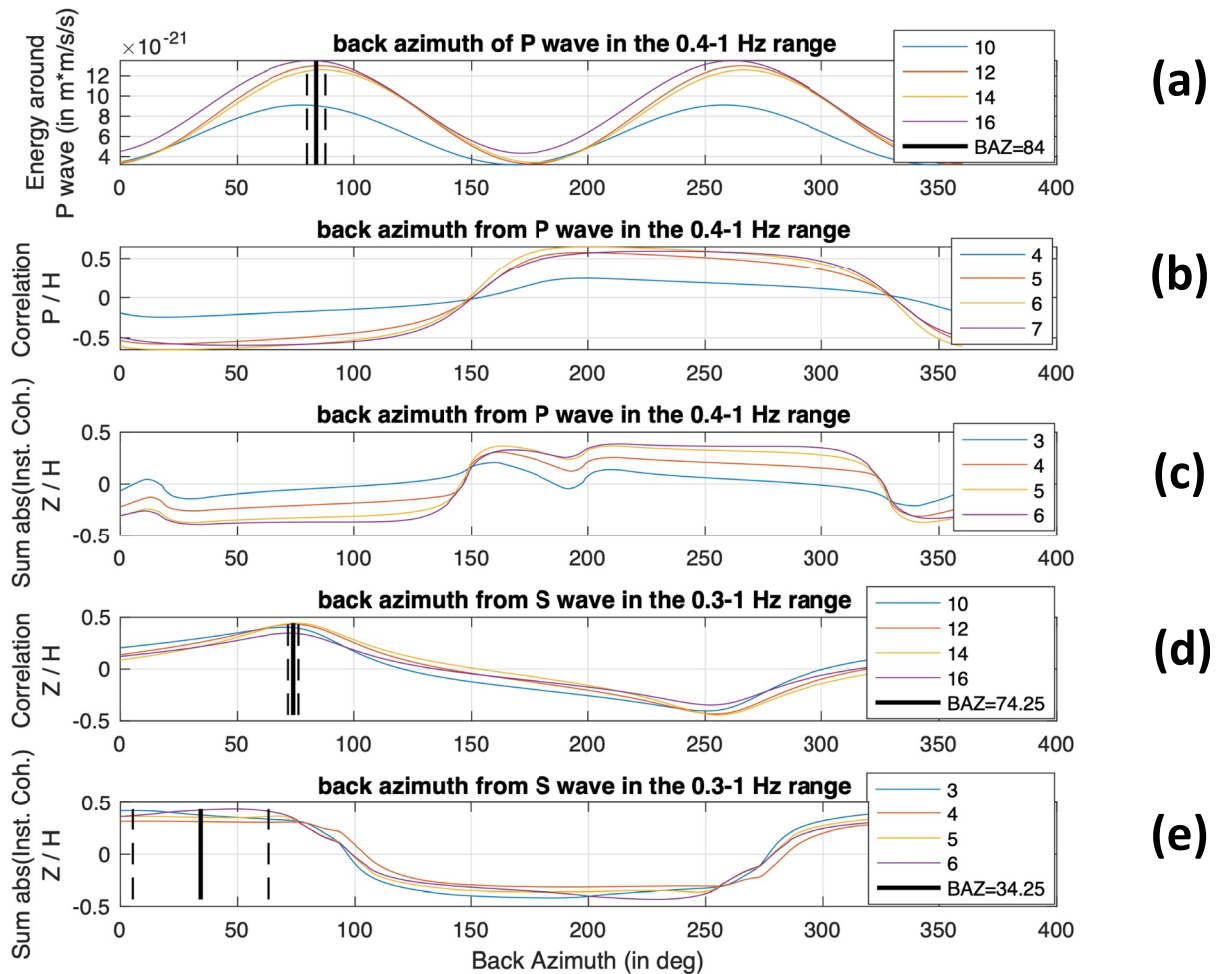
Figure A11

Figure A11. Back azimuth determination for event S0916d. From top to bottom: energy along the horizontal component around the P wave arrival, correlation coefficient between vertical and horizontal components around the P wave, average of instantaneous phase coherence between vertical and horizontal components around the P wave, correlation coefficient between vertical and horizontal components around the S wave, average of instantaneous phase coherence between vertical and horizontal components around the S wave. For each panel, all possible back azimuths are examined and various window length (in s) are tested (different colors). Best estimates of back azimuth are identified by vertical black lines. The error on the back azimuth estimate is computed by averaging this standard deviation and the average width of the correlation function at 80% of its peak value.
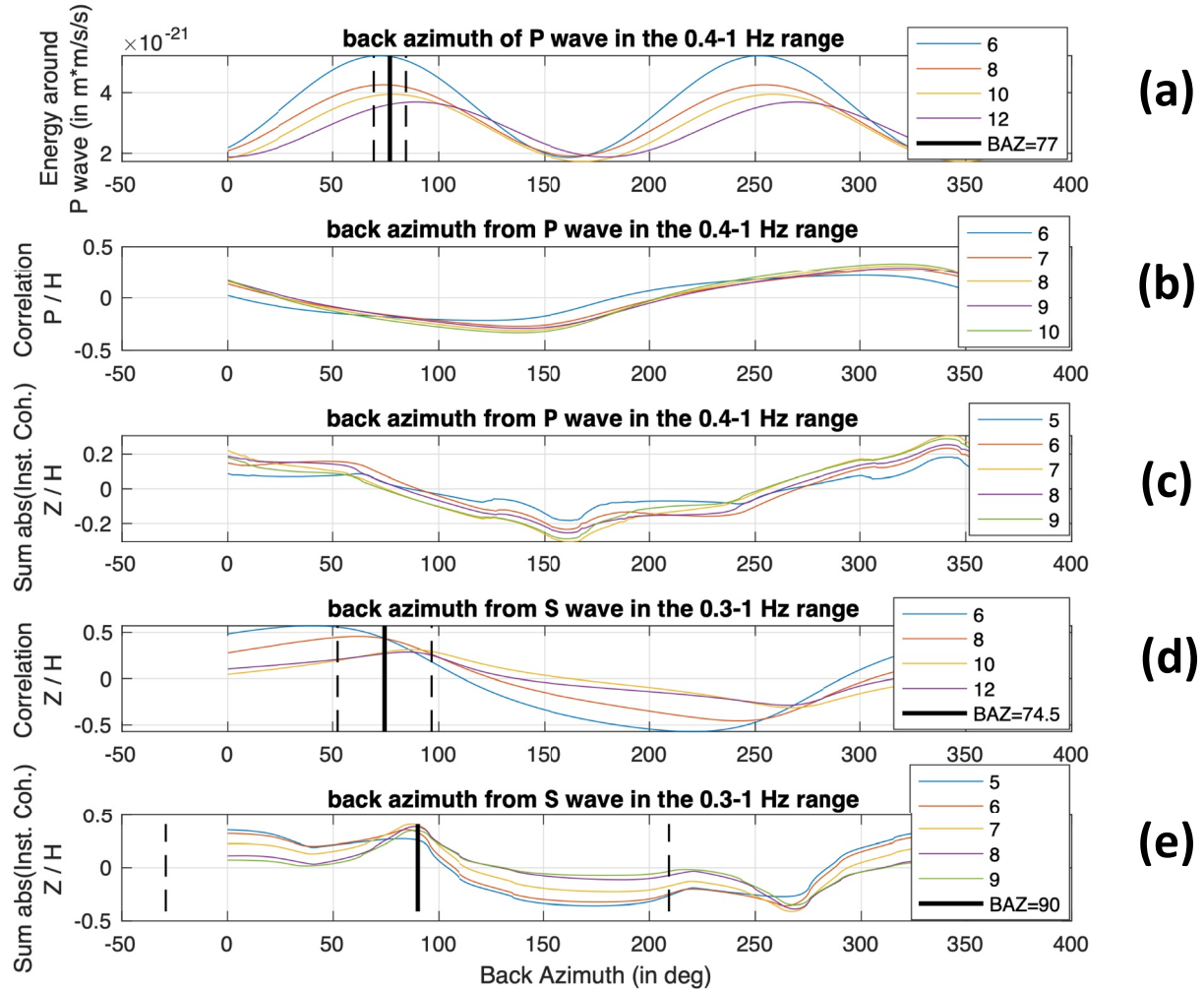
Figure A12

Figure A12. Back azimuth determination for event S0861a. From top to bottom: energy along the horizontal component around the P wave arrival, correlation coefficient between vertical and horizontal components around the P wave, average of instantaneous phase coherence between vertical and horizontal components around the P wave, correlation coefficient between vertical and horizontal components around the S wave, average of instantaneous phase coherence between vertical and horizontal components around the S wave. For each panel, all possible back azimuths are examined and various window length (in s) are tested (different colors). Best estimates of back azimuth are identified by vertical black lines. The error on the back azimuth estimate is computed by averaging this standard deviation and the average width of the correlation function at 80% of its peak value.
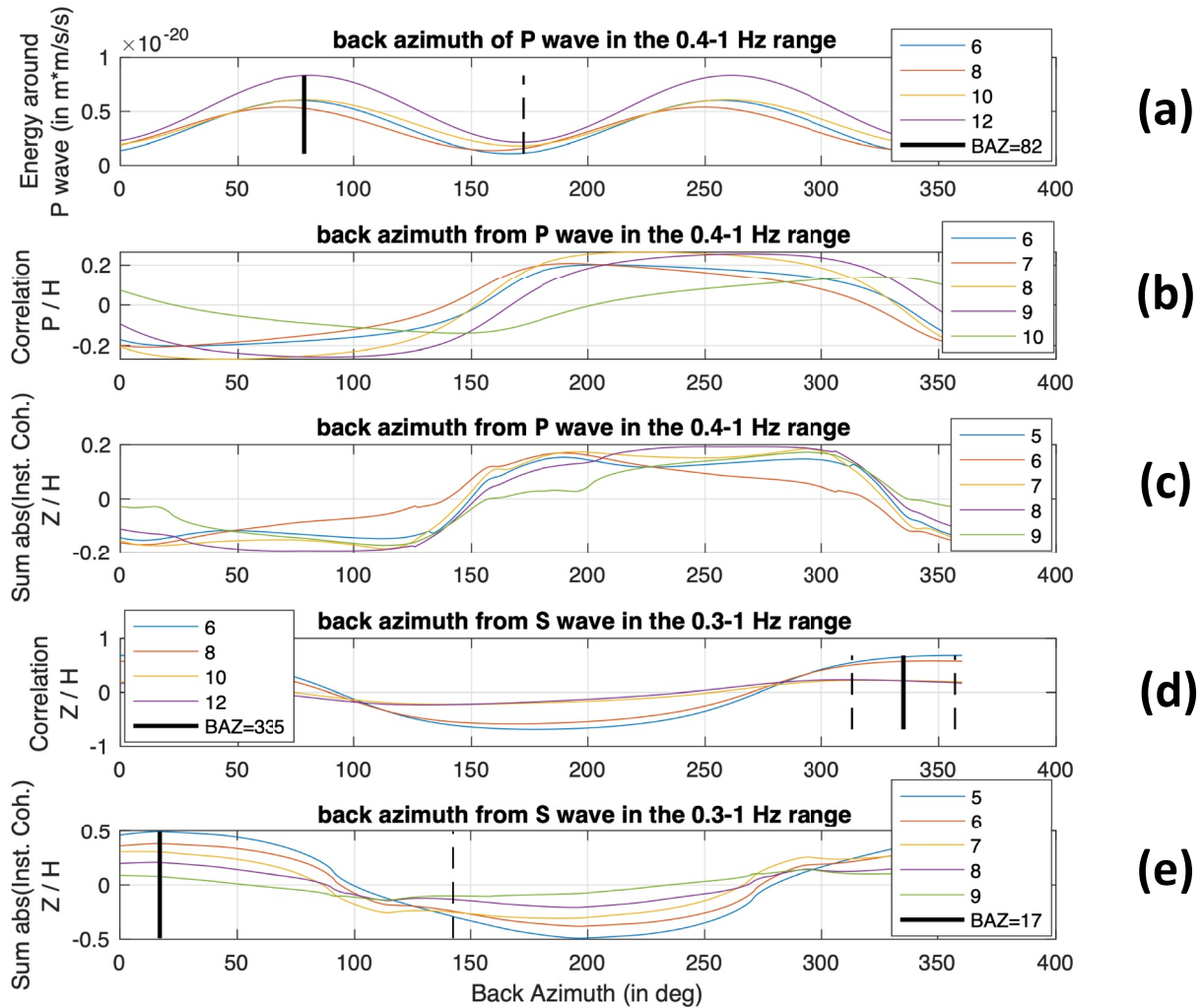
Figure A13

Figure A13. Back azimuth determination for event S0864a. From top to bottom: energy along the horizontal component around the P wave arrival, correlation coefficient between vertical and horizontal components around the P wave, average of instantaneous phase coherence between vertical and horizontal components around the P wave, correlation coefficient between vertical and horizontal components around the S wave, average of instantaneous phase coherence between vertical and horizontal components around the S wave. For each panel, all possible back azimuths are examined and various window length (in s) are tested (different colors). Best estimates of back azimuth are identified by vertical black lines. The error on the back azimuth estimate is computed by averaging this standard deviation and the average width of the correlation function at 80% of its peak value.

Figure A14

Figure A14. Back azimuth determination for event S0820a. From top to bottom: energy along the horizontal component around the P wave arrival, correlation coefficient between vertical and horizontal components around the P wave, average of instantaneous phase coherence between vertical and horizontal components around the P wave, correlation coefficient between vertical and horizontal components around the S wave, average of instantaneous phase coherence between vertical and horizontal components around the S wave. For each panel, all possible back azimuths are examined and various window length (in s) are tested (different colors). Best estimates of back azimuth are identified by vertical black lines. The error on the back azimuth estimate is computed by averaging this standard deviation and the average width of the correlation function at 80% of its peak value.

Figure A15

Figure A15. Back azimuth determination for event S0154a. From top to bottom: energy along the horizontal component around the P wave arrival, correlation coefficient between vertical and horizontal components around the P wave, average of instantaneous phase coherence between vertical and horizontal components around the P wave, correlation coefficient between vertical and horizontal components around the S wave, average of instantaneous phase coherence between vertical and horizontal components around the S wave. For each panel, all possible back azimuths are examined and various window length (in s) are tested (different colors). Best estimates of back azimuth are identified by vertical black lines. The error on the back azimuth estimate is computed by averaging this standard deviation and the average width of the correlation function at 80% of its peak value.

Figure A16

Figure A16. Back azimuth determination for event S0409d. From top to bottom: energy along the horizontal component around the P wave arrival, correlation coefficient between vertical and horizontal components around the P wave, average of instantaneous phase coherence between vertical and horizontal components around the P wave, correlation coefficient between vertical and horizontal components around the S wave, average of instantaneous phase coherence between vertical and horizontal components around the S wave. For each panel, all possible back azimuths are examined and various window length (in s) are tested (different colors). Best estimates of back azimuth are identified by vertical black lines. The error on the back azimuth estimate is computed by averaging this standard deviation and the average width of the correlation function at 80% of its peak value.

Appendix B: Example of Depth Phases Arrival Time Determination for Quakes of Different Qualities

This section is providing examples of depth phases arrival time estimates with correlation method for quakes of quality A and B. We were not able to determine depth phases arrival times for the quality C quakes used in this study (Figures B1 and B2).
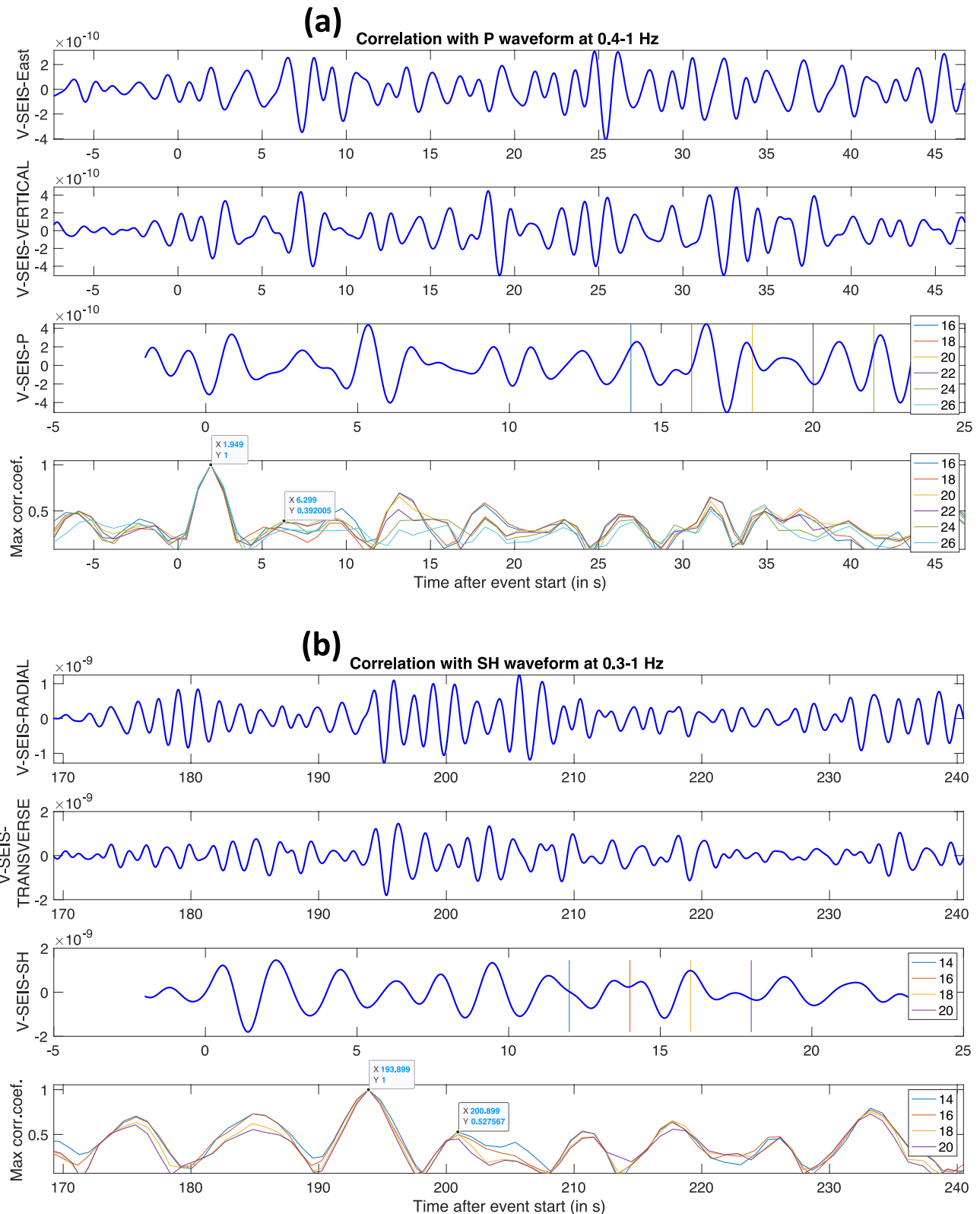
Figure B1. Determination of depth phases arrival times by waveform correlation with the direct phases for pP (a) and sS (b) of event of quality A S0809a. In each sub-figure, the top panel is the radial ground velocity, the second panel is the vertical (for pP) or transverse (for sS) ground velocity, the third panel is the reference waveform extracted from the second panel, and the third panel is the correlation function of the reference waveform with the vertical (for pP) or the transverse (for sS) velocity record. Markers indicate the arrival time of the direct phase and the depth phase. Times are relative to event start time defined by Mars Quake Service.
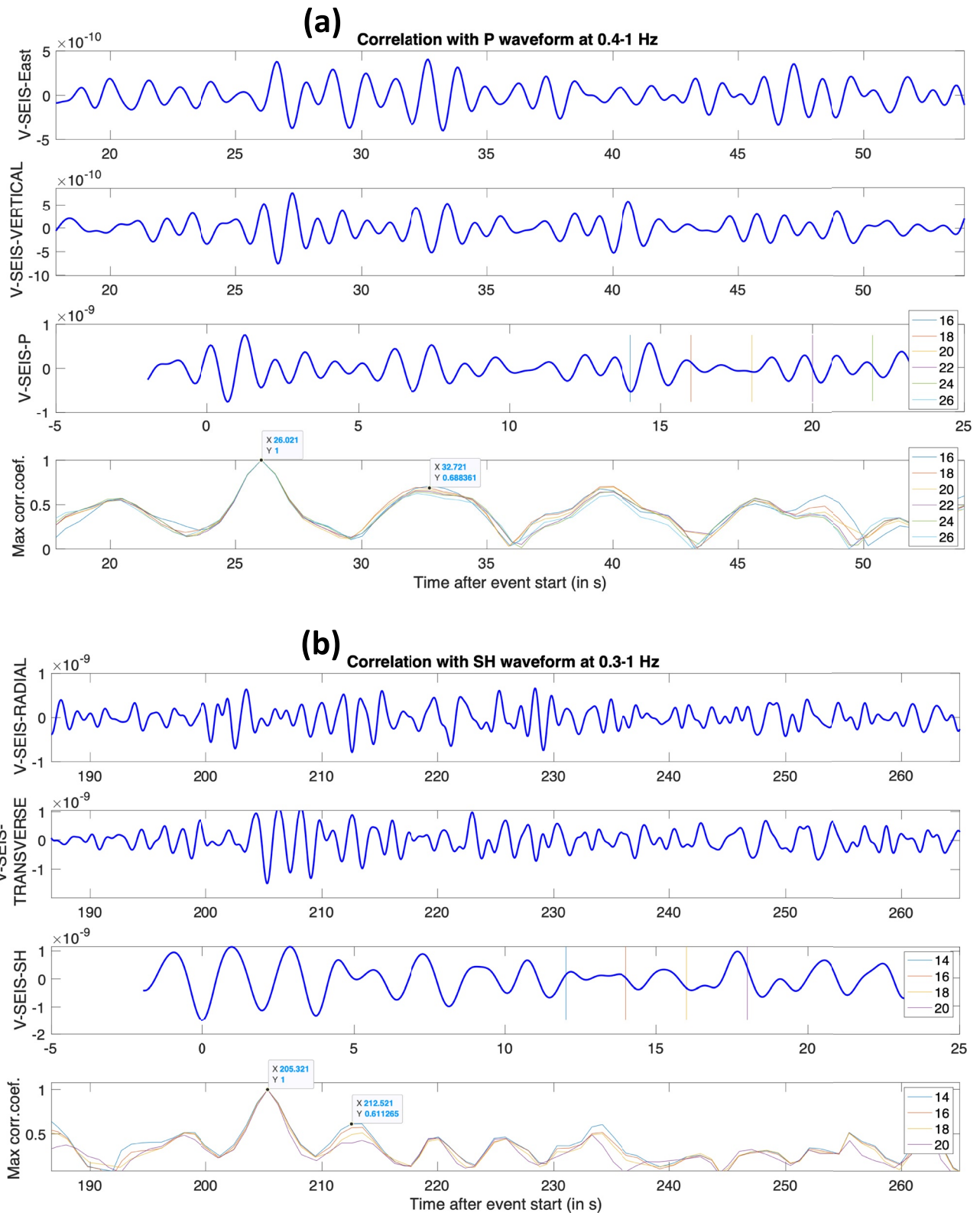
Figure B2. Determination of depth phases arrival times by waveform correlation with the direct phases for pP (a) and sS (b) of event of quality B S0784a. In each sub-figure, the top panel is the radial ground velocity, the second panel is the vertical (for pP) or transverse (for sS) ground velocity, the third panel is the reference waveform extracted from the second panel, and the third panel is the correlation function of the reference waveform with the vertical (for pP) or the transverse (for sS) velocity record. Markers indicate the arrival time of the direct phase and the depth phase. Times are relative to event start time defined by Mars Quake Service.

Appendix C: Influence of the Composition on the Geodynamically Constrained Inversions Results

To test the influence of the composition considered in both major and HPEs on our inversion results, we considered two separate inversion sets where we fixed the composition to that proposed in J. Taylor et al. (2013). We considered an inversion set without crustal constraints and another with crustal constraints. Besides the composition, all the other inversion parameters were identical to those considered elsewhere in this study.

Figure C1 displays the results corresponding to the inversion without crustal constraints. In this case, the inversion is not able to constrain the values of most geodynamic parameters as indicated by the overlap between *prior* and *posterior* values, with the exception of the core radius, constrained here to be close to 1,800 km. These results are very similar to the other inversion set considering the EH45 composition (see Figures 14a1–14e1). This demonstrate that when no crustal constraints are applied, the composition model does not play a major role in our inversion results.

However, when performing the same exercise by considering constraints on the crustal thickness in the inversion process we were not able to find any solution that satisfied all our constraints. This is due to the fact that present-day temperature structure of our inversion output is too hot to satisfy simultaneously a relatively thin crust and a moment of inertia factor within the measured range. This result is consistent with a recent study (Knapmeyer-Endrun et al., 2021). Consequently, contrary to the case described above, when constraints on the crustal thickness are considered, the solution is considerably more sensitive to the composition considered. Because the bulk HPE content for EH45 and the composition considered here are similar (see Section 4.1.2), the observed influence is mainly that of the major element content. However, the HPE can also influence our inversion results because this quantity directly affects crustal production over time and eventually the present-day crustal thickness (Khan et al., 2021; Knapmeyer-Endrun et al., 2021).

Among the main compositional models for both bulk and HPE elements proposed in the literature, Lodders and Fegley (1997) has a significantly different content in HPE compared to that in (Sanloup et al., 1999) and (J. Taylor et al., 2013). However, we did not consider the composition proposed in Lodders and Fegley (1997), because its extreme HPE enrichment likely yields large amounts of melting that would result in overly thick crusts at the present-day (Plesa et al., 2015), which would fail to match constraints on the crustal thickness.
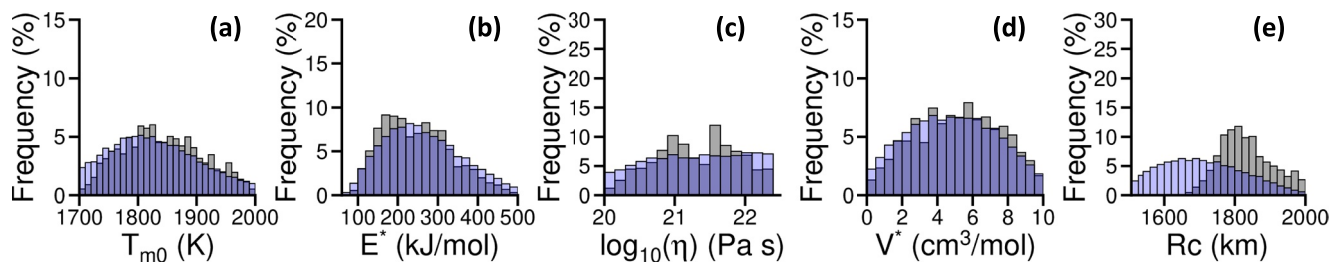

Figure C1. Marginal posterior distributions of the geodynamic governing parameters using no constraint on the crustal thickness. (a) Distribution of the initial temperature below the lithosphere T_{m_0}, (b) effective activation energy E^*, (c) reference mantle viscosity η_0, (d) activation volume V^*, and (e) core radius R_c. The blue and gray histograms correspond to the *a priori* and *a posteriori* distributions, respectively.

Appendix D: Data Sensitivity to the Structure

The maximum depth sensitivity of the body waves to the structure is located near the turning point of the ray paths (e.g., Daubar et al., 2018; Drilleau et al., 2021; Khan et al., 2021). To address the question of resolution, we have computed the depth of the turning points of P- and S-waves and their multiples (PP, PPP, SS, and SSS) for all the models belonging to the *a posteriori* distributions shown in Figure 8. Figure D1 shows how much the information contained in the individual data can resolve the 1-D seismic structure. This computation was performed using the `TauP` toolkit (Crotwell et al., 1999), based on the raypath geometry.

The spread of the turning points' distributions indicates that their location is model-dependent. Figures D1a1, D1d1, D1a2 and D1d2 show that the two farthest marsquakes (S0185a and S0861a) located at ~54° of epicentral distance are able to sample the mantle down to ~700 km. The P- and S-waves generated by the third most distant marsquake (event S0325a located at ~40° of epicentral distance) are sensitive to the structure down to ~300 to 400 km depth. Because the remaining marsquakes are located at very close distances from each other, near 30° epicentral distance, and that no lateral variations are considered in our modeling, they all show turning points ranging between ~100 and 300 km.

Figures D1b1, D1c1, D1b2 and D1c2 show that the depth of the turning points of P- and S-waves multiples are shallower. The multiples reflected once (PP and SS) are located below ~200 km depth, while the multiples reflected twice (PPP and SSS) reach a maximum depth of ~150 km. The distributions of the turning points for all the seismic phases taken together highlight the fact that most of the data are sensitive to the structure of Mars above 200 km depth (Figures D1g1 and D1g2). Without considering the ScS phases, and thanks to the three farthest marsquakes (S0185a, S0325a, and S0861a), the body waves phases provide constraints on the interior structure down to 700 km depth, above the olivine-to-wadsleyite phase transition. Note that the distribution of the turning points obtained using the classical approach are broader, due to the larger flexibility allowed for the models, compared to the more constraining character of the geodynamic approach.
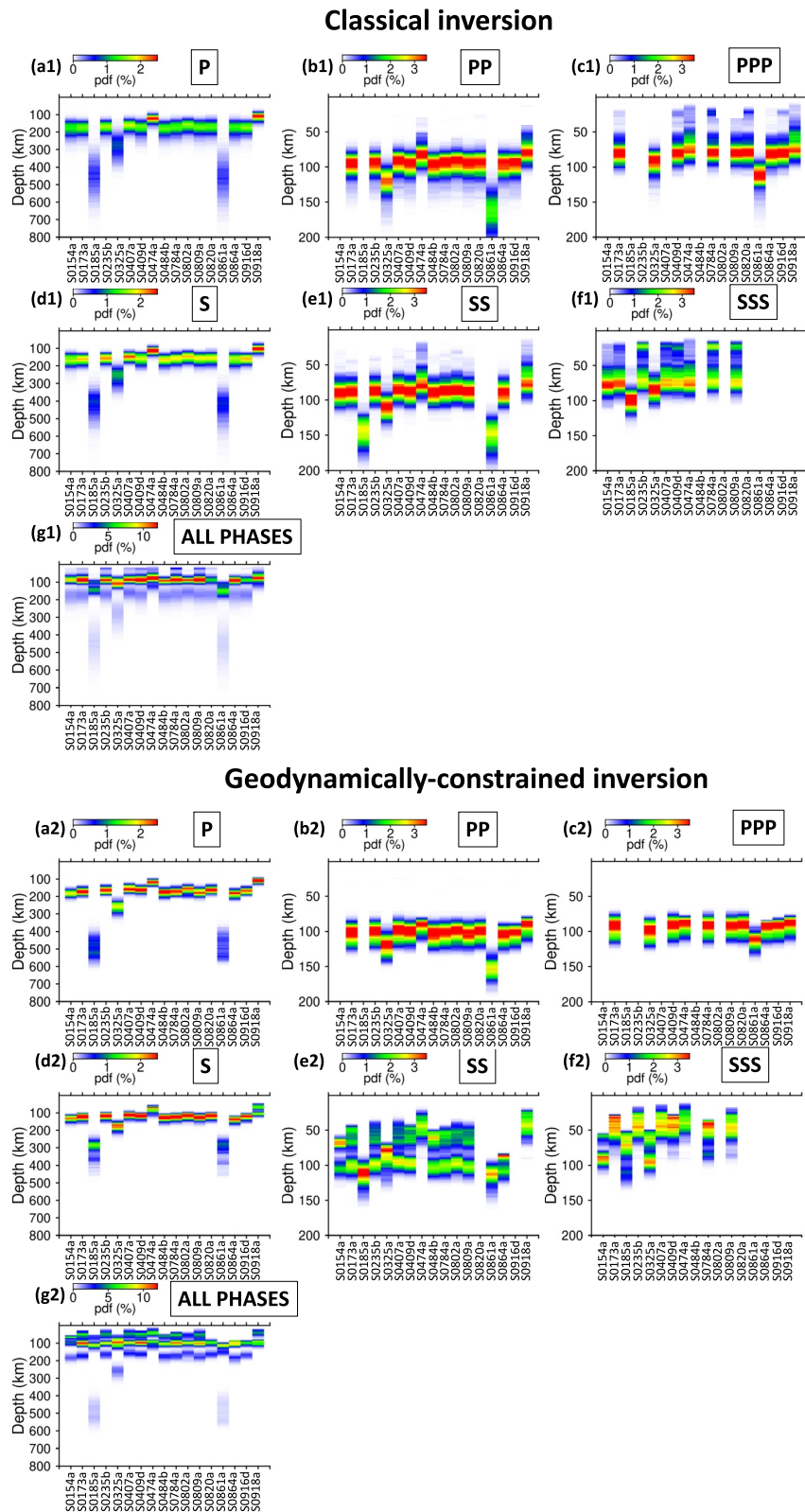
Figure D1. *A posteriori* probability density functions (pdfs) of the turning points' location for P (a1 and a2), PP (b1 and b2), PPP (c1 and c2), S (d1 and d2), SS (e1 and e2), SSS (f1 and f2), considering the 17 marsquakes and using the classical (top) and geodynamic (bottom) approaches. The combined *a posteriori* pdfs of P-, S-waves, and their multiples, are shown in panels (g1 and g2). A spherically symmetric medium is assumed.

Appendix E: Estimation of the Core Radius

The output marginal distributions of the core radius (R_c) are displayed in Figure E1. The retrieved values are in good agreement with the previous study of Stähler et al. (2021), with $R_c = 1,817 \pm 87$ and $1,820 \pm 55$ km for the classical and geodynamically constrained inversions, respectively (Figure E1a). When constraints on the crustal thickness are considered, the core radius is similar for the classical models with $R_c = 1,798 \pm 76$ km (Figure E1b). However, the mean core radius is smaller for the geodynamically constrained models, with $R_c = 1,773 \pm 41$ km.
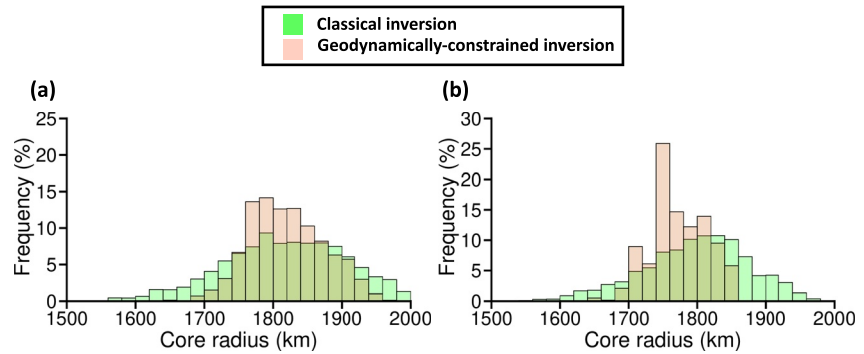
Figure E1. Output marginal distributions of the core radius (R_c) using (a) no constraint and (b) constraints on the crustal thickness. The results of the classical and geodynamically constrained inversions are shown in green and pink, respectively.

Appendix F: Correlations of the Crustal Parameters

Figures F1 and F2 show the correlations between the depth location and the S-wave velocity of the three crustal layers. Dcr_{upper}, Dcr_{mid}, Dcr_{lower}, and $V_{S_{upper}}$, $V_{S_{mid}}$, $V_{S_{lower}}$, refer to the depths and V_S of the upper, mid, and lower crusts, respectively. For a given crustal layer, these figures reveal a correlation between the seismic velocities and the location of the layer. This expected thickness-velocity trade-off results from the fact that the data are fit equally well when the discontinuity is deeper and V_S is higher, and vice versa. A trade-off between the seismic velocities in the three layers is also observed, because we impose an increase of the seismic velocities with depth in the crust.

When constraints on the crustal thickness are applied, the marginal distributions of V_S and V_P models are slightly shifted toward larger values (Figures 13b and 13c). This is mainly explained by the trade-off between the depth of
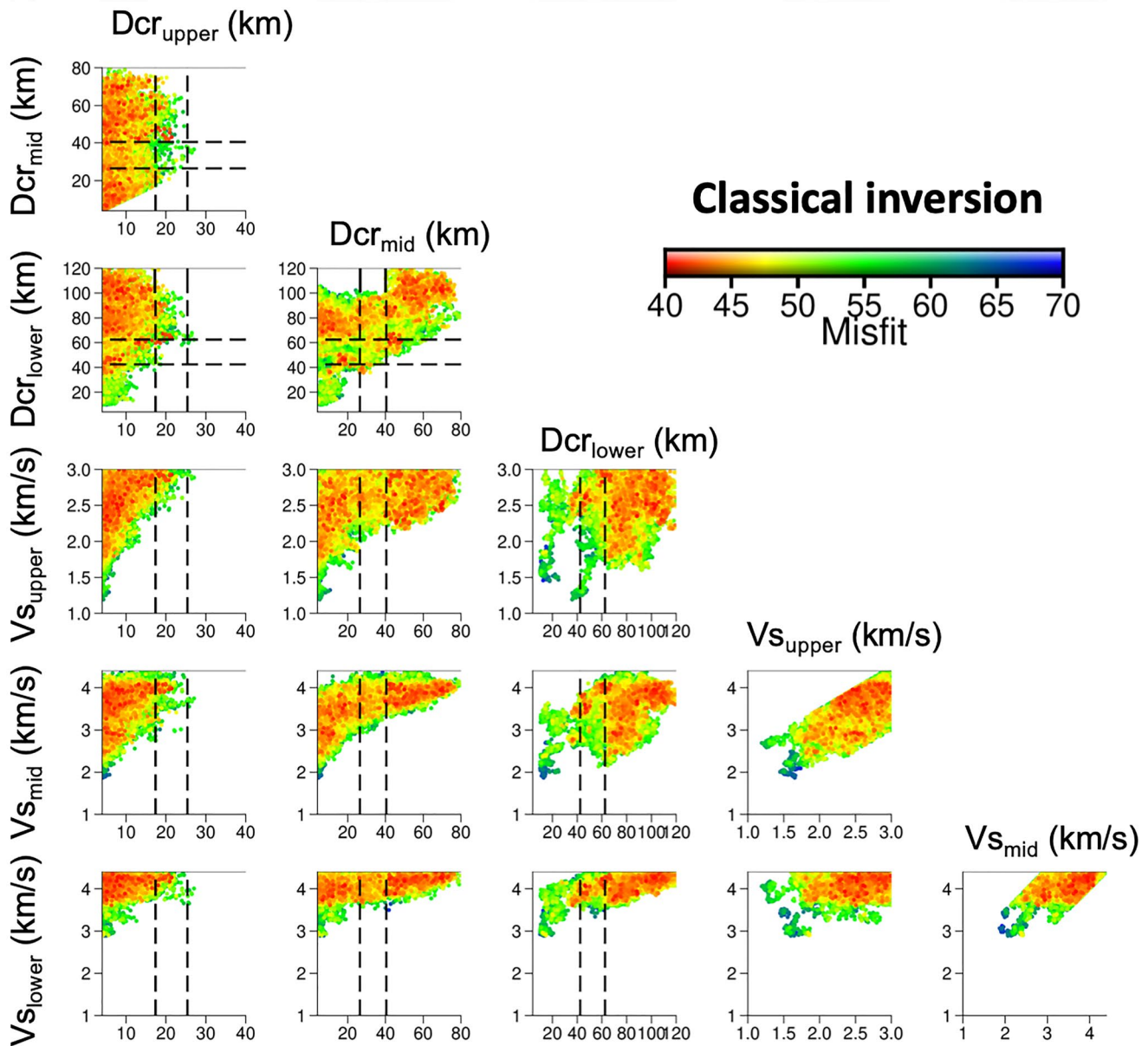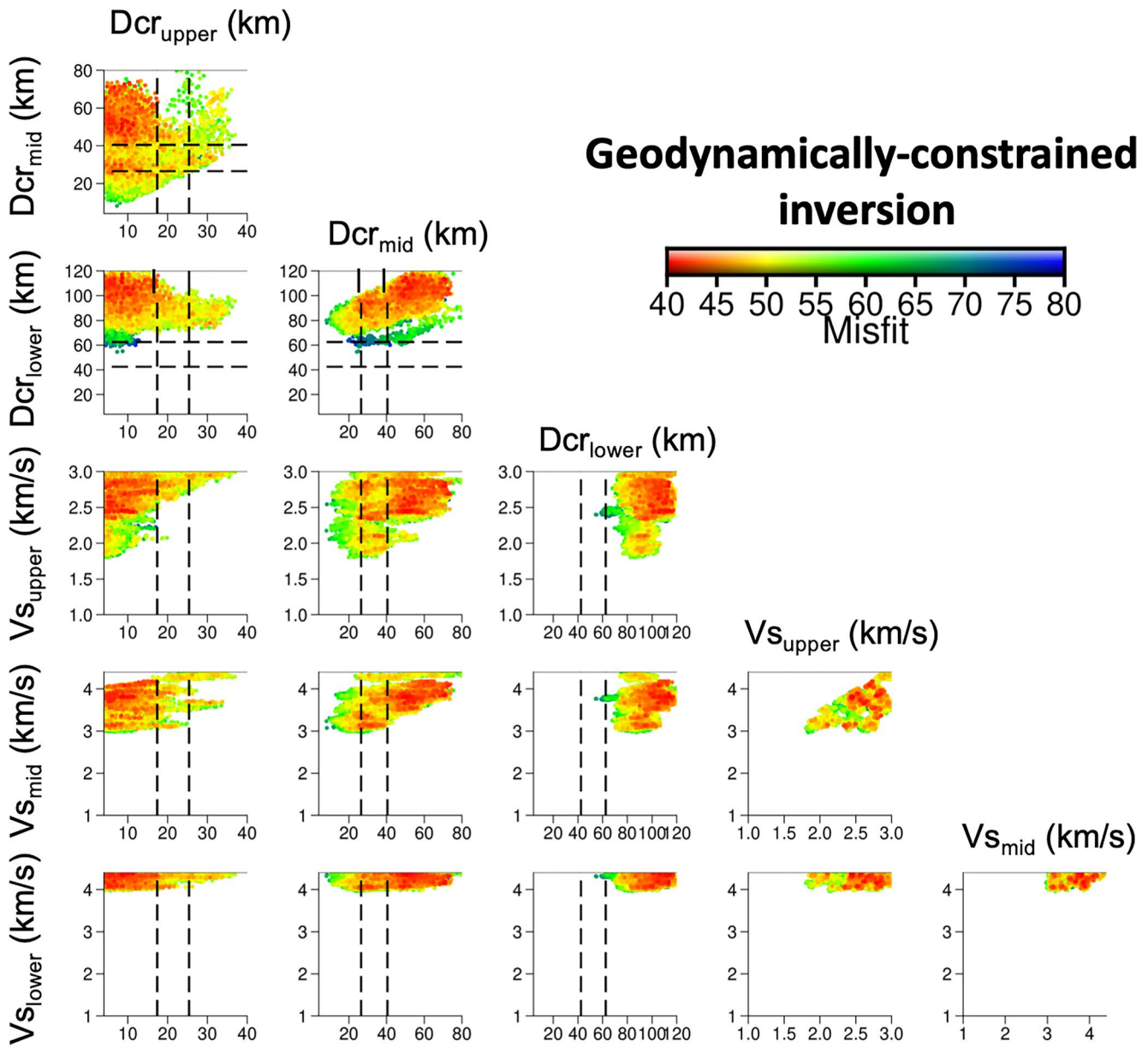

Figure F1. Correlations between the depth and the S-wave velocity of the three crustal layers, for all the models accepted by the classical inversion. Dcr_{upper}, Dcr_{mid}, Dcr_{lower}, and $V_{S_{upper}}$, $V_{S_{mid}}$, $V_{S_{lower}}$, refer to the depths and V_S of the upper, mid, and lower crusts, respectively. Red and blue colors indicate small and large misfit values, respectively. The black dashed lines are the allowed depth range for Dcr_{upper}, Dcr_{mid}, and Dcr_{lower}, used in Section 5.4.

Figure F2. Correlations between the depth and the S-wave velocity of the three crustal layers, for all the models accepted by the geodynamically constrained inversion. Dcr_{upper}, Dcr_{mid}, Dcr_{lower}, and $V_{S_{upper}}$, $V_{S_{mid}}$, $V_{S_{lower}}$, refer to the depths and V_S of the upper, mid, and lower crusts, respectively. Red and blue colors indicate small and large misfit values, respectively. The black dashed lines are the allowed depth range for Dcr_{upper}, Dcr_{mid}, and Dcr_{lower}, used in Section 5.4.

the layer and the seismic velocity. When the depth range of the crustal layers is more restricted (see black dashed lines in Figures F1 and F2), a large number of models with small seismic velocities are rejected by the algorithm.

Appendix G: Inversion Results Considering a Dual-Layered Crust

We investigated to what extent a dual-layered crust could fit the data. Figure G1 shows the pdfs of V_S, V_P, and the V_P/V_S ratio, considering two layers in the crust instead of three. The prior bounds correspond to the ones described in Table 2, except that V_S in the upper crust is authorized to vary between 1.0 and 4.4 km/s instead of 1.0–3.0 km/s. In the mantle, the pdfs are very similar to the ones obtained using three layers in the crust (Figure 8). It is worth noting that models with two layers in the crust provide an equivalent datafit (not shown) to the one obtained using a three layers model, which means that the existence of the uppermost layer of the three layers model is not absolutely required by the data (Table G1).
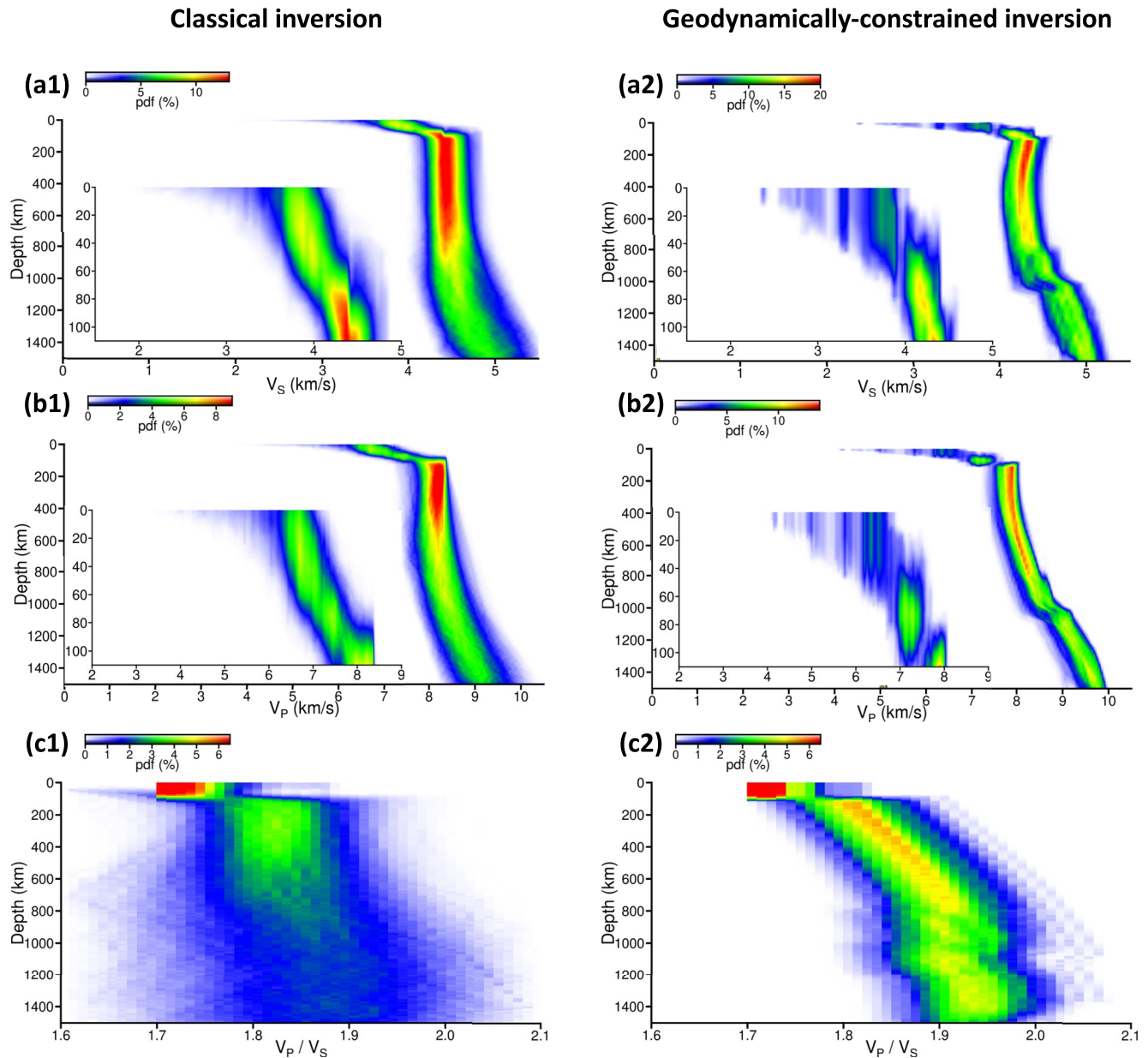
Figure G1. Inversion results using the classical approach (right-hand panel) and the geodynamic approach (left-hand panel), considering two layers in the crust. Panels (a1, a2, b1, b2) are *a posteriori* probability density functions (pdfs) of the 1-D V_S and V_P profiles, respectively. Panels (c1 and c2) are *a posteriori* pdfs of the V_P/V_S ratio. Blue and red colors show small and large probabilities, respectively. The pdf is computed by counting the number of sampled profiles in each of the cases. The discretization is 1 km for depth, 0.05 km/s for V_S and V_P, and 0.01 for the V_P/V_S ratio. For a given depth, the sum of the pdf over all the parameter intervals is equal to 100%. The black lines in panels (a1 and b1) shows the prior bounds of classical models in the mantle. A zoom on the crust between the surface and 110 km depth is shown in panels (a1, a2, b1, b2).

Table G1

Summary of the Mean Layer's Depth (Dcr), the S- and P-Waves Velocities (V_S, V_P) in the Two Crustal Layers, and the V_P/V_S Ratio in the Whole Crust

	Classical inversion	Geodynamically constrained inversion
Dcr_{upper} (km)	35.8 ± 23.4	42.3 ± 16.9
Dcr_{lower} (km)	84.0 ± 22.2	96.5 ± 11.8
$V_{S_{upper}}$ (km/s)	3.6 ± 0.4	3.4 ± 0.4
$V_{S_{lower}}$ (km/s)	4.1 ± 0.2	4.2 ± 0.1
$V_{P_{upper}}$ (km/s)	6.2 ± 0.7	5.9 ± 0.7
$V_{P_{lower}}$ (km/s)	7.1 ± 0.4	7.2 ± 0.2
V_P/V_S	1.74 ± 0.03	1.74 ± 0.03

Note. The subscripts $_{upper}$ and $_{lower}$ refer to parameters belonging to the upper and lower crusts, respectively.

Figure G2
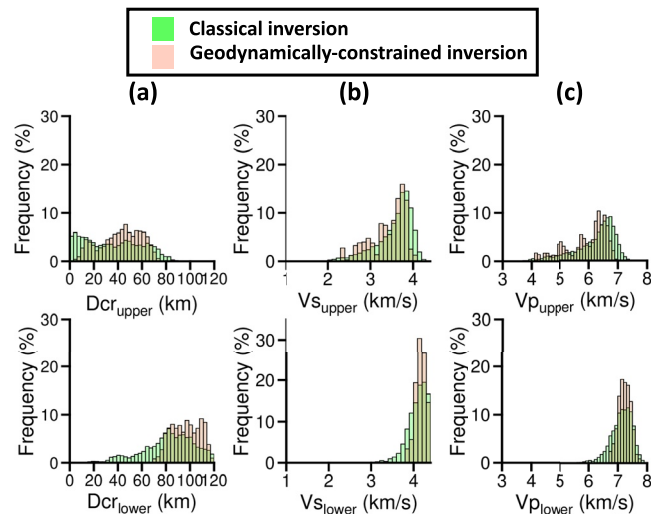
Figure G2. Output marginal distributions of the inverted parameters in the crust. The results of the classical and geodynamically constrained inversions are shown in green and pink, respectively. (a) Displays the layer's depth (Dcr). Panels (b and c) are the P- and S-waves velocities. The subscripts $_{upper}$ and $_{lower}$ refer to parameters belonging to the upper and lower crusts, respectively.

Data Availability Statement

Derived data files used in this study Drilleau (2022) are available using the https://doi.org/10.5281/zenodo.6334517. The numerical codes used to compute the results in this study are described in detail in Drilleau et al. (2021) (McMC inversion); Samuel et al. (2019) (Mars parameterized convection); and Crotwell et al. (1999) (ray paths and travel times).

References

Banerdt, W. B., Smrekar, S. E., Banfield, D., Giardini, D., Golombek, M., Johnson, C. L., et al. (2020). Initial results from the InSight mission on Mars. *Nature Geoscience*, *13*(3), 1–14. https://doi.org/10.1038/s41561-020-0544-y

Banfield, D. J., Rodriguez-Manfredi, J. A., Russell, C. T., Rowe, K. M., Leneman, D., Lai, H. R., et al. (2019). InSight auxiliary payload sensor suite (APSS). *Space Science Reviews*, *215*(1), 4. https://doi.org/10.1007/s11214-018-0570-x

Barton, N. (2006). Rock quality, seismic velocity, attenuation and anisotropy (Vol. *15*). https://doi.org/10.1201/9780203964453

Boynton, W. V., Taylor, G. J., Evans, L. G., Reedy, R. C., Starr, R., Janes, D. M., et al. (2007). Concentration of H, Si, Cl, K, Fe, and Th in the low- and mid-latitude regions of Mars. *Journal of Geophysical Research*, *112*(12), 1–15. https://doi.org/10.1029/2007JE002887

Breuer, D., & Spohn, T. (2006). Viscosity of the Martian mantle and its initial temperature: Constraints from crust formation history and the evolution of the magnetic field. *Planetary and Space Science*, *54*(2), 153–169. https://doi.org/10.1016/j.pss.2005.08.008

Brinkman, N., Stähler, S. C., Giardini, D., Schmelzbach, C., Khan, A., Jacob, A., et al. (2021). First focal mechanisms of marsquakes. *Journal of Geophysical Research: Planets*, *126*(4), e2020JE006546. https://doi.org/10.1029/2020JE006546

Carr, M. H., & Head, J. W. (2010). Geologic history of Mars. *Earth and Planetary Science Letters*, *294*(3–4), 185–203. https://doi.org/10.1016/j.epsl.2009.06.042

Charalambous, C., Stott, A. E., Pike, W. T., McClean, J. B., Warren, T., Spiga, A., et al. (2021). A comodulation analysis of atmospheric energy injection into the ground motion at InSight, Mars. *Journal of Geophysical Research: Planets*, *126*(4), e2020JE006538. https://doi.org/10.1029/2020je006538

Christensen, N. I. (1995). Poisson's ratio and crustal seismology. *Journal of Geophysical Research*, *101*(B2), 3139–3156. https://doi.org/10.1029/95jb03446

Christensen, N. I., & Mooney, W. D. (1995). Seismic velocity structure and composition of the continental crust: A global view. *Journal of Geophysical Research*, *100*(B6), 9761–9788. https://doi.org/10.1029/95jb00259

Clinton, J. F., Ceylan, S., van Driel, M., Giardini, D., Stähler, S. C., Böse, M., et al. (2021). The marsquake catalogue from InSight, sols 0–478. *Physics of the Earth and Planetary Interiors*, *310*, 106595. https://doi.org/10.1016/j.pepi.2020.106595

Compaire, N., Margerin, L., Garcia, R. F., Pinot, B., Calvet, M., Orhand-Mainsant, G., et al. (2021). Autocorrelation of the ground vibrations recorded by the SEIS-InSight seismometer on Mars. *Journal of Geophysical Research: Planets*, *126*(4), e2020JE006498. https://doi.org/10.1029/2020je006498

Condie, K. C. (2016). *Earth as an evolving planetary system*. Elsevier. https://doi.org/10.1016/C2015-0-00179-4

Connolly, J. A. D. (2005). Computation of phase equilibria by linear programming: A tool for geodynamic modeling and its application to subduction zone decarbonation. *Earth and Planetary Science Letters*, *236*(1–2), 524–541. https://doi.org/10.1016/j.epsl.2005.04.033

Crisp, J. A. (1984). Rates of magma emplacement and volcanic output. *Journal of Volcanology and Geothermal Research*, *20*(3–4), 177–211. https://doi.org/10.1016/0377-0273(84)90039-8

Crotwell, H. P., Owens, T. J., & Ritsema, J. (1999). The TauP toolkit: Flexible seismic travel-time and ray-path utilities. *Seismological Research Letters*, *70*(2), 154–160. https://doi.org/10.1785/gssrl.70.2.154

Dahmen, N. L., Clinton, J. F., Ceylan, S., van Driel, M., Giardini, D., Khan, A., et al. (2021). Super high frequency events: A new class of events recorded by the insight seismometers on Mars. *Journal of Geophysical Research: Planets*, *126*(2), e2020JE006599. https://doi.org/10.1029/2020JE006599

Daubar, I., Lognonné, P., Teanby, E. A., Miljkovic, K., Stevanović, J., Vaubaillon, J., et al. (2018). Impact-seismic investigations of the InSight mission. *Space Science Reviews*, *214*(6), 132. https://doi.org/10.1007/s11214-018-0562-x

Daubar, I., Lognonné, P., Teanby, N. A., Collins, G. S., Clinton, J., Stähler, S., et al. (2020). A new crater near insight: Implications for seismic impact detectability on Mars. *Journal of Geophysical Research: Planets*, *125*(8), e2020JE006382. https://doi.org/10.1029/2020JE006382

Drilleau, M. (2022). Marsquake locations and 1-D seismic models for Mars from InSight data (data) (version 1) [Data set]. Zenodo. https://doi.org/10.5281/zenodo.6334517

Drilleau, M., Beucler, E., Lognonné, P., Panning, M., Knapmeyer-Endrun, B., Banerdt, B. W., et al. (2020). MSS/1: Single-station and single-event marsquake inversion. *Earth and Space Science*, *7*(12), e2020EA001118. https://doi.org/10.1029/2020EA001118

Drilleau, M., Beucler, E., Mocquet, A., Verhoeven, O., Moebs, G., Burgos, G., et al. (2013). A Bayesian approach to infer radial models of temperature and anisotropy in the transition zone from surface wave dispersion curves. *Geophysical Journal International*, *195*(2), 1165–1183. https://doi.org/10.1093/gji/ggt284

Drilleau, M., Samuel, H., Rivoldini, A., Panning, M., & Lognonné, P. (2021). Bayesian inversion of the Martian structure using geodynamic constraints. *Geophysical Journal International*, *226*(3), 1615–1644. https://doi.org/10.1093/gji/ggab105

Durán, C., Khan, A., Ceylan, S., Zenhäusern, G., Stähler, S., Clinton, J., & Giardini, D. (2022). Seismology on Mars: An analysis of 1 direct, reflected, and converted seismic body waves with implications for interior structure. *Physics of the Earth and Planetary Interiors*, *325*, 106851. https://doi.org/10.1016/j.pepi.2022.106851

Ernst, R., Grosfils, E., & Mège, D. (2002). Giant dike swarms: Earth, Venus, and Mars. *Annual Review of Earth and Planetary Sciences*, *29*(1), 489–534. https://doi.org/10.1146/annurev.earth.29.1.489

Filiberto, J., Gross, J., Trela, J., & Ferré, E. C. (2014). Gabbroic shergottite northwest Africa 6963: An intrusive sample of Mars. *American Mineralogist*, *99*(4), 601–606. https://doi.org/10.2138/am.2014.4638

Filiberto, J., Gross, J., Udry, A., Trela, J., Wittmann, A., Cannon, K. M., et al. (2018). Shergottite northwest Africa 6963: A pyroxene-cumulate Martian gabbro. *Journal of Geophysical Research: Planets*, *123*(7), 1823–1841. https://doi.org/10.1029/2018JE005635

Garcia, R. F., Kenda, B., Kawamura, T., Spiga, A., Murdoch, N., Lognonné, P. H., et al. (2020). Pressure effects on the SEIS-InSight instrument, improvement of seismic records, and characterization of long period atmospheric waves from ground displacements. *Journal of Geophysical Research: Planets*, *125*(7), e2019JE006278. https://doi.org/10.1029/2019je006278

Giardini, D., Lognonné, P., Banerdt, W. B., Pike, W. T., Christensen, U., Ceylan, S., et al. (2020). The seismicity of Mars. *Nature Geoscience*, *13*(3), 205–212. https://doi.org/10.1038/s41561-020-0539-8

Greeley, R., & Guest, J. (1987). *Geologic map of the eastern equatorial region of Mars* (Tech. Rep.). USGS Numbered Series, IMAP, 1802, Chapter B. https://doi.org/10.3133/i1802B

Hall, J. L., Solomon, S. C., & Head, J. W. (1986). Elysium region, Mars: Tests of lithospheric loading models for the formation of tectonic features. *Journal of Geophysical Research*, *91*(B11), 11377. https://doi.org/10.1029/jb091ib11p11377

Hartmann, W. K., Malin, M., McEwen, A., Carr, M., Soderblom, L., Thomas, P., et al. (1999). Evidence for recent volcanism on Mars from crater counts. *Nature*, *397*(6720), 586–589. https://doi.org/10.1038/17545

Hastings, W. K. (1970). Monte Carlo sampling methods using Markov chains and their applications. *Biometrika*, *57*(1), 97–109. https://doi.org/10.1093/biomet/57.1.97

Hauck, S. A., & Phillips, R. J. (2002). Thermal and crustal evolution of Mars. *Journal of Geophysical Research*, *107*(E7), 5052. https://doi.org/10.1029/2001JE001801

Horvath, D. G., Moitra, P., Hamilton, C. W., Craddock, R. A., & Andrews-Hanna, J. C. (2021). Evidence for geologically recent explosive volcanism in Elysium Planitia, Mars. *Icarus*, *365*(February), 114499. https://doi.org/10.1016/j.icarus.2021.114499

InSight Marsquake Service. (2021). *Mars seismic catalogue, insight mission; v7 2021-07-01*. ETHZ, IPGP, JPL, ICL, University of Bristol. https://doi.org/10.12686/a12

InSight Mars SEIS Data Service. (2019a). *InSight SEIS data bundle*. PDS Geosciences (GEO) node. https://doi.org/10.17189/1517570

InSight Mars SEIS Data Service. (2019b). *SEIS raw data, InSight Mission*. IPGP, JPL, CNES, ETHZ, ICL, MPS, ISAE-Supaero, LPG, MFSC. https://doi.org/10.18715/SEIS.INSIGHT.XB\2016

Kedar, S., Panning, M. P., Smrekar, S. E., Stähler, S. C., King, S. D., Golombek, M. P., et al. (2021). Analyzing low frequency seismic events at Cerberus Fossae as long period volcanic quakes. *Journal of Geophysical Research: Planets*, *126*(4), 1–28. https://doi.org/10.1029/2020JE006518

Khan, A., Ceylan, S., van Driel, M., Giardini, D., Lognonné, P., Samuel, H., et al. (2021). Upper mantle structure of Mars from InSight seismic data. *Science*, *373*(6553), 434–438. https://doi.org/10.1126/science.abf2966

Khan, A., Liebske, C., Rozel, A., Rivoldini, A., Nimmo, F., Connolly, J. A. D., et al. (2018). A geophysical perspective on the bulk composition of Mars. *Journal of Geophysical Research: Planets*, *224*(2–4), 575–611. https://doi.org/10.1002/2017JE005371

Khan, A., van Driel, M., Böse, M., Giardini, D., Ceylan, S., Yan, J., et al. (2016). Single-station and single-event marsquake location and inversion for structure using synthetic Martian waveforms. *Physics of the Earth and Planetary Interiors*, *258*, 28–42. https://doi.org/10.1016/j.pepi.2016.05.017

Kim, D., Lekić, V., Irving, J. C. E., Schmerr, N., Knapmeyer-Endrun, B., Joshi, R., et al. (2021). Improving constraints on planetary interiors with PPS receiver functions. *Journal of Geophysical Research: Planets*, *126*(11), e2021JE006983. https://doi.org/10.1029/2021JE006983

Knapmeyer, M., Oberst, J., Hauber, E., Wählisch, M., Deuchler, C., & Wagner, R. (2006). Working models for spatial distribution and level of Mars' seismicity. *Journal of Geophysical Research*, *111*(11), 1–23. https://doi.org/10.1029/2006JE002708

Knapmeyer-Endrun, B., Panning, M. P., Bissig, F., Joshi, R., Khan, A., Kim, D., et al. (2021). Thickness and structure of the Martian crust from InSight seismic data. *Science*, *373*(6553), 438–443. https://doi.org/10.1126/science.abf8966

Konopliv, A. S., Park, R. S., & Folkner, W. M. (2016). An improved JPL Mars gravity field and orientation from Mars orbiter and lander tracking data. *Icarus*, *274*, 253–260. https://doi.org/10.1016/j.icarus.2016.02.052

Konopliv, A. S., Park, R. S., Rivoldini, A., Baland, R. M., Le Maistre, S., Van Hoolst, T., et al. (2020). Detection of the Chandler Wobble of Mars from orbiting spacecraft. *Geophysical Research Letters*, *47*(21), 1–9. https://doi.org/10.1029/2020GL090568

Lodders, K., & Fegley, B. (1997). An oxygen isotope model for the composition of Mars. *Icarus*, *126*(2), 373–394. https://doi.org/10.1006/icar.1996.5653

Lognonné, P., Banerdt, W., Pike, W. T., Giardini, D., Christensen, U., Garcia, R. F., et al. (2020). Constraints on the shallow elastic and anelastic structure of Mars from insight seismic data. *Nature Geoscience*, *13*(3), 213–220. https://doi.org/10.1038/s41561-020-0536-y

Lognonné, P., Banerdt, W. B., Giardini, D., Pike, W. T., Christensen, U., Laudet, P., et al. (2019). SEIS: Insight's seismic experiment for internal structure of Mars. *Space Science Reviews*, *215*(1), 12. https://doi.org/10.1007/s11214-018-0574-6

Martire, L., Garcia, R. F., Rolland, L., Spiga, A., Lognonné, P. H., Banfield, D., et al. (2020). Martian infrasound: Numerical modeling and analysis of InSight's data. *Journal of Geophysical Research: Planets*, *125*(6), e2020JE006376. https://doi.org/10.1029/2020je006376

McSween, H. Y. (2015). Petrology on Mars. *American Mineralogist*, *100*(11–12), 2380–2395. https://doi.org/10.2138/am-2015-5257

Metropolis, N., Rosenbluth, A. W., Rosenbluth, M. N., Teller, A. H., & Teller, E. (1953). Equation of state calculations by fast computing machines. *The Journal of Chemical Physics*, *21*(6), 1087–1091. https://doi.org/10.1063/1.1699114

Mosegaard, K., & Tarantola, A. (1995). Monte-Carlo sampling of solutions to inverse problems. *Journal of Geophysical Research*, *100*(B7), 12431–12447. https://doi.org/10.1029/94jb03097

Murdoch, N., Mimoun, D., Garcia, R. F., Rapin, W., Kawamura, T., Lognonné, P., et al. (2017). Evaluating the wind-induced mechanical noise on the InSight seismometers. *Space Science Reviews*, *211*(1–4), 429–455. https://doi.org/10.1007/s11214-016-0311-y

Neukum, G., Jaumann, R., Hoffmann, H., Hauber, E., Head, J. W., Basilevsky, A. T., et al. (2004). Recent and episodic volcanic and glacial activity on Mars revealed by the High Resolution Stereo Camera. *Nature*, *432*(7020), 971–979. https://doi.org/10.1038/nature03231

Neumann, G. A., Zuber, M. T., Wieczorek, M. A., McGovern, P. J., Lemoine, F. G., & Smith, D. E. (2004). Crustal structure of Mars from gravity and topography. *Journal of Geophysical Research*, *109*(E8), E08002. https://doi.org/10.1029/2004JE002262

Nimmo, F., & Faul, U. H. (2013). Dissipation at tidal and seismic frequencies in a melt-free, anhydrousMars. *Journal of Geophysical Research: Planets*, *118*(12), 2558–2569. https://doi.org/10.1002/2013je004499

Ohtani, E., Suzuki, A., & Kato, T. (1998). Flotation of olivine and diamond in mantle melt at high pressure: Implications for fractionation in the deep mantle and ultradeep origin of diamond. In *Properties of Earth and planetary materials at high pressure and temperature* (pp. 227–239). American Geophysical Union (AGU).

Panning, M. P., Beucler, E., Drilleau, M., Mocquet, A., Lognonné, P., & Banerdt, W. B. (2015). Verifying single-station seismic approaches using Earth-based data: Preparation for data return from the insight mission to Mars. *Icarus*, *248*, 230–242. https://doi.org/10.1016/j.icarus.2014.10.035

Panning, M. P., Lognonné, P., Bruce Banerdt, W., Garcia, R., Golombek, M., Kedar, S., et al. (2017). Planned products of the Mars structure service for the insight mission to Mars. *Space Science Reviews*, *211*(1), 611–650. https://doi.org/10.1007/s11214-016-0317-5

Perrin, C., Jacob, A., Lucas, A., Myhill, R., Hauber, E., Batov, A., et al. (2022). Geometry and segmentation of Cerberus Fossae, Mars: Implications on marsquake properties in Elysium Planitia. *Journal of Geophysical Research: Planets*, *127*(1), e2021JE007118. https://doi.org/10.1029/2021JE007118

Plesa, A.-C., Padovan, S., Tosi, N., Breuer, D., Grott, M., Wieczorek, M. A., et al. (2018). The thermal state and interior structure of Mars. *Geophysical Research Letters*, *45*(22), 12198–12209. https://doi.org/10.1029/2018GL080728

Plesa, A.-C., Tosi, N., Grott, M., & Breuer, D. (2015). Thermal evolution and Urey ratio of Mars. *Journal of Geophysical Research: Planets*, *120*(5), 995–1010. https://doi.org/10.1002/2014je004748

Robinson, M. S., Mouginis-Mark, P. J., Zimbelman, J. R., Wu, S. S., Ablin, K. K., & Howington-Kraus, A. E. (1993). Chronology, eruption duration, and atmospheric contribution of the Martian volcano Apollinaris Patera. *Icarus*, *104*(2), 301–323. https://doi.org/10.1006/icar.1993.1103

Samuel, H., Lognonné, P. H., Panning, M., & Lainey, V. (2019). The rheology and thermal history of Mars revealed by the orbital evolution of Phobos. *Nature*, *569*(7757), 523–527. https://doi.org/10.1038/s41586-019-1202-7

Sanloup, C., Jambon, A., & Gillet, P. (1999). A simple chondritic model of Mars. *Physics of the Earth and Planetary Interiors*, *112*(1–2), 43–54. https://doi.org/10.1016/s0031-9201(98)00175-7

Sautter, V., & Payré, V. (2021). Alkali magmatism on Mars: An unexpected diversity. *Comptes-Rendus des Géosciences*, *353*(S2), 1–29. https://doi.org/10.5802/crgeos.64

Schimmel, M., Stutzmann, E., & Gallart, J. (2011). Using instantaneous phase coherence for signal extraction from ambient noise data at a local to a global scale. *Geophysical Journal International*, *184*(1), 494–506. https://doi.org/10.1111/j.1365-246x.2010.04861.x

Scholz, J.-R., Widmer-Schnidrig, R., Davis, P., Lognonné, P., Pinot, B., Garcia, R. F., et al. (2020). Detection, analysis, and removal of glitches from InSight′s seismic data from Mars. *Earth and Space Science*, *7*(11), e2020EA001317. https://doi.org/10.1029/2020ea001317

Smith, D. E., Zuber, M. T., Frey, H. V., Garvin, J. B., Head, J., Muhleman, D. O., et al. (2001). Mars Orbiter Laser Altimeter: Experiment summary after the first year of global mapping of Mars. *Journal of Geophysical Research*, *106*(E10), 23689–23722. https://doi.org/10.1029/2000je001364

Smrekar, S. E., Lognoné, P., Spohn, T., Banerdt, B., Breuer, D., Christensen, U., et al. (2019). Pre-mission insights on the interior of Mars. *Space Science Reviews*, *215*(1), 3. https://doi.org/10.1007/s11214-018-0563-9

Stähler, S. C., Khan, A., Banerdt, W. B., Lognonné, P., Giardini, D., Ceylan, S., et al. (2021). Seismic detection of the Martian core. *Science*, *373*(6553), 443–448. https://doi.org/10.1126/science.abi7730

Stixrude, L., & Lithgow-Bertelloni, C. (2011). Thermodynamics of mantle minerals – II. Phase equilibria. *Geophysical Journal International*, *184*(3), 1180–1213. https://doi.org/10.1111/j.1365-246X.2010.04890.x

Stutzmann, E., Schimmel, M., Lognonné, P., Horleston, A., Ceylan, S., van Driel, M., et al. (2021). The polarization of ambient noise on Mars. *Journal of Geophysical Research: Planets*, *126*(1), e2020JE006545. https://doi.org/10.1029/2020je006545

Tanaka, K. L., Chapman, M. G., & Scott, D. H. (1992). Geologic map of the Elysium region of Mars (Vol. *IMAP 2147*). Retrieved from https://pubs.er.usgs.gov/publication/i2147

Tarantola, A. (2005). *Inverse problem theory – And methods for model parameter estimation*. SIAM.

Taylor, G. J. (2013). The bulk composition of Mars. *Chemie der Erde*, *73*(4), 401–420. https://doi.org/10.1016/j.chemer.2013.09.006

Taylor, J., Teanby, N. A., & Wookey, J. (2013). Estimates of seismic activity in the Cerberus Fossae region of Mars. *Journal of Geophysical Research: Planets*, *118*(12), 2570–2581. https://doi.org/10.1002/2013JE004469

Udry, A., Howarth, G. H., Lapen, T. J., & Righter, M. (2017). Petrogenesis of the NWA 7320 enriched Martian gabbroic shergottite: Insight into the Martian crust. *Geochimica et Cosmochimica Acta*, *204*, 1–18. https://doi.org/10.1016/j.gca.2017.01.032

Vaucher, J., Baratoux, D., Mangold, N., Pinet, P., Kurita, K., & Grégoire, M. (2009). The volcanic history of central Elysium Planitia: Implications for Martian magmatism. *Icarus*, *204*(2), 418–442. https://doi.org/10.1016/j.icarus.2009.06.032

Vidale, J. E. (1986). Complex polarization analysis of particle motion. *Bulletin of the Seismological Society of America*, *76*(5), 1393–1405. https://doi.org/10.1785/BSSA0760051393

Wanke, H., & Dreibus, G. (1994). Chemistry and accretion history of Mars. *Philosophical Transactions: Physical Sciences and Engineering*, *349*(1), 285–293. https://doi.org/10.1098/rsta.1994.0132

Watters, T. R. (1993). Compressional tectonism on Mars. *Journal of Geophysical Research*, *98*(E9), 49–60. https://doi.org/10.1029/93je01138

Wieczorek, M. A., Beuthe, M., Rivoldini, A., & Van Hoolst, T. (2019). Hydrostatic interfaces in bodies with nonhydrostatic lithospheres. *Journal of Geophysical Research: Planets*, *124*(5), 1410–1432. https://doi.org/10.1029/2018JE005909

Wieczorek, M. A., & Zuber, M. T. (2004). Thickness of the Martian crust: Improved constraints from geoid-to-topography ratios. *Journal of Geophysical Research E: Planets*, *109*(1), 1–16. https://doi.org/10.1029/2003je002153

Yoshizaki, T., & McDonough, W. F. (2021). Earth and Mars – Distinct inner solar system products. *Geochemistry*, *81*(2), 125746. https://doi.org/10.1016/j.chemer.2021.125746

Zenhäusern, G., Stähler, S. C., Clinton, J. F., Giardini, D., Ceylan, S., & Garcia, R. F. (2022). Low-frequency marsquakes and where to find them: Back azimuth determination using a polarization analysis approach. *Bulletin of the Seismological Society of America*. https://doi.org/10.1785/0120220019